Ingénierie de la frustration magnétique à travers les impuretés

Piyush Jeena

THÈSE PRÉSENTÉE
POUR OBTENIR LE GRADE DE

DOCTEUR DE
L'UNIVERSITÉ DE BORDEAUX

Ecole doctorale Sciences physiques et de l'ingénieur (ED SPI)

Laboratoire Ondes et Matière d'Aquitaine (CNRS)

Présenté par
Piyush JEENA

Engineering magnetic frustration with impurities

Sous la direction de
Ludovic JAUBERT

Soutenue le : **7th December, 2022**

Membres du jury :

M. KNOLLE, Johannes, Professor, TU München, Rapporteur
M. LAFLORENCIE, Nicolas, Directeur de recherche, LPT Toulouse, Rapporteur
M. CAYSSOL, Jerome, Professeur, LOMA, CNRS, Université DE Bordeaux , Examinateur
Mme. LHOTEL, Elsa, Directrice de recherche, Institut Néel, CNRS Grennoble, Examinateur
M. JAUBERT, Ludovic , Chargé de recherche, LOMA, CNRS, Université de Bordeaux, Directeur de these

Acknowledgments

First and foremost, I would like to thank my advisor Ludovic Jaubert, who guided me throughout this project. I am extremely grateful for his invaluable advice, continuous support, and godlike patience during my PhD. His immense knowledge and plentiful experience have encouraged me in all the time of my academics here at the institute. He was always available and responsive to my queries, academic or otherwise. He has helped me a lot to improve my naive experience with physics research. I am extremely thankful to the ANR research grant and CNRS for the financial support during the last three years and funding the travel for conferences to Paris and Amsterdam. I would also like to thank Prof. Johannes Knolle and Nicolas Laflorencie who accepted to be my rapporteurs and for their critical feedback. I would also thank Prof. Jerome Cayssol and Elsa Lhotel to be my examiners.

Secondly, I would like to thank Prof. Anuradha Jagannathan(LPS Orsay, Université Paris-Saclay) who gave me a chance to work on condensed matter theory during the summer of 2018. She was super kind and helpful during my first-stay outside of India. I would also thank Prof. Soumya Bera (IIT Bombay) who supervised my Master's thesis since a lot of skills learnt there has helped me here during my PhD. I would also like to thank Prof. Sayan Chakrabarti (IIT Guwahati) for supervising my Bachelor's thesis since it was my first proper research project.

I am also thankful to Suzanne Bessus, Josiane Parzych and Walid Louati for handling the administrative work. I would also thank THE IT CROWD (Eric, David and Alain) and the CURTA HPC cluster. Also thankful to Benjamin Masset for all the arrangements in the lab.

I am also grateful to my friends here at Bordeaux:: Alpesh(the only guy with a slightly similar research area in the lab and polar opposite food preference, he is an extreme vegetarian), Shashank(who offered me a place in his apartment after my CROUS ended), Debo, Elodie(office-mate and aversive to light), Aditya, Bilal, Vagarsh, Bhavesh, Mariam, Tony, Sotiris, Kapil, Shashank, Alice(Lisbon), Kankana(BTS enthusiast), Tannu(quirky), Guratinder. I would also thank my IIT batchmates (Deependra(Stockholm), Naveen(Zagreb), Navin, Saurabh, Mayank) and people (Nihal, Rajah, Lode, Nicolas etc.) in Munich who helped me during my small stint there. Also thanks to all people who helped me in the past 3

years.

Finally, I would like to thank my parents and sister who supported me in this endeavor for the past 9 years(4 yrs of bachelor's + 2 yr master's + 3 yr PhD) and defended me against ever-asking relatives about my job. Their belief in me(without knowing what I actually do) has kept my sanity in check.

Abstract

In highly frustrated magnetism, it is usually believed that pristine crystals are necessary, and impurities are unwanted perturbations. Our motivation here is to take the opposing view, and use impurities as a tool to design the properties of frustrated magnets. Motivated by experiments on the rare-earth pyrochlore oxide $Er_2Ti_{2-x}Sn_xO_7$, the idea is to tune the Hamiltonian of our system via non-magnetic dilution x; in other words, to use impurities as a knob to explore unknown parts of the phase diagram. This approach brings us at the frontier between geometric frustration and spin glasses.

Chapter 1 explores the literature on frustrated magnetism : Paradigmatic models for frustrated magnets, work done on pure pyrochlore oxides ($Er_2Sn_2O_7$ and $Er_2Ti_2O_7$), spin glasses, classical spin liquids, experimental techniques etc. The numerical formalism (Monte Carlo simulations) to probe frustrated magnetism are outlined in **Chapter 2** along with the algorithmic details.

In **Chapter 3**, we report the phase diagram of $Er_2Ti_{2-x}Sn_xO_7$ for $0 \leq x \leq 2$, using classical Monte-Carlo simulations. To build a detailed theory, we extract from simulations the specific heat, susceptibility, neutron-scattering structure factor, microscopic fluctuations and spin dynamics. Our calculations reproduce the shape of the experimental phase diagram, with a competition between Γ_5 and Palmer-Chalker antiferromagnetic orders. Depending on the type of disorder used in our model, an intermediate spin-glass phase takes place where magnetic order disappears. A pronounced asymmetry in favor of Γ_5 is observed, that we explain when connecting this non-magnetic dilution to the generic nearest-neighbor phase diagram on pyrochlore.

Chapter 4 is a phenomenological extension of the quenched disorder model (used in chapter 3) to classical spin liquids(Heisenberg antiferromagnetic and tensor spin liquid). We try to establish a connection from one to the other via quenched disorder. We analyze the microscopic properties and the dynamical structure factor for our model.

We summarize our findings and future work in **Chapter 5** along with an appendix at the end.

Dans le magnétisme hautement frustré, on pense généralement que des cristaux vierges sont nécessaires et que les impuretés sont des perturbations indésirables. Notre motivation ici est de prendre le point de vue opposé et d'utiliser les impuretés comme un outil pour concevoir les propriétés des aimants frustrés. Motivée par des expériences sur l'oxyde de pyrochlore de terre rare $Er_2Ti_{2-x}Sn_xO_7$, l'idée est d'accorder l'hamiltonien de notre système via une dilution non magnétique x ; en d'autres termes, utiliser les impuretés comme bouton pour explorer les parties inconnues du diagramme de phase. Cette approche nous amène à la frontière entre la frustration géométrique et les lunettes de spin.

Chapitre 1 explore la littérature sur le magnétisme frustré : Modèles paradigmatiques pour les aimants frustrés, travaux effectués sur les oxydes de pyrochlore purs ($Er_2Sn_2O_7$ et $Er_2Ti_2O_7$), verres de spin, liquides de spin classiques, techniques expérimentales, etc.

Le formalisme numérique (simulations de Monte Carlo) pour sonder le magnétisme frustré est décrit dans le **Chapitre 2** avec les détails algorithmiques.

Dans le **Chapitre 3**, nous rapportons le diagramme de phase de $Er_2Ti_{2-x}Sn_xO_7$ pour $0 \leq x \leq 2$, en utilisant le Monte classique -Simulations Carlo. Pour construire une théorie détaillée, nous extrayons des simulations la chaleur spécifique, la susceptibilité, le facteur de structure de diffusion des neutrons, les fluctuations microscopiques et la dynamique de spin. Nos calculs reproduisent la forme du diagramme de phase expérimental, avec une compétition entre les ordres antiferromagnétiques Γ_5 et Palmer-Chalker. Selon le type de désordre utilisé dans notre modèle, une phase intermédiaire de verre de spin a lieu où l'ordre magnétique disparaît. Une asymétrie prononcée en faveur de Γ_5 est observée, que nous expliquons en reliant cette dilution non magnétique au diagramme de phase générique du plus proche voisin sur le pyrochlore.

Chapitre 4 est une extension phénoménologique du modèle de désordre quenched (utilisé au chapitre 3) aux liquides de spin classiques (liquide antiferromagnétique de Heisenberg et tensor spin liquide). Nous essayons d'établir une connexion de l'un à l'autre via le désordre éteint. Nous analysons les propriétés microscopiques et le facteur de structure dynamique pour notre modèle.

Nous résumons nos découvertes et nos travaux futurs dans le **Chapitre 5** avec une annexe à la fin.

Contents

List of Figures viii
List of Tables xiv

1 Introduction **1**
1.1 What is frustration ? 1
1.1.1 Experimental Intuition 2
1.1.2 Canonical frustrated models 3
1.1.3 Order by Disorder(ObD) 4
1.2 The pyrochlore lattice 5
1.2.1 Generic nearest-neighbor model 6
1.2.2 Order parameters 7
1.2.3 Classical Phase Diagram 9
1.3 Er based pyrochlores 14
1.3.1 $Er_2Ti_2O_7$ 15
1.3.2 $Er_2Sn_2O_7$ 15
1.3.3 $Er_2Ti_{2-x}Sn_xO_7$ 15
1.4 Classical spin liquids on the pyrochlore lattice 16
1.4.1 The Heisenberg antiferromagnet 16
1.4.2 The tensor spin liquid 17
1.5 Quenched disorder and spin glasses 17
1.6 Motivation of this thesis 20

2 Numerical Methods **21**
2.1 Introduction 21
2.2 Sampling procedure and the Metropolis Algorithm 22
2.3 Heatbath Method 24
2.4 Over-relaxation 26
2.5 Averaging in quenched disorder systems 26
2.6 Parallel Tempering 28
2.7 Finite size scaling 30
2.8 Technical details of Monte Carlo simulations 31
2.9 Landau-Lifshitz dynamics 33
2.10 Structure Factors 33

3 Non-magnetic dilution in $Er_2Ti_{2-x}Sn_xO_7$ **34**
3.1 Models 35

3.1.1 Model 1: Correlated quenched disorder (CQD) 35
3.1.2 Model 2 : No quenched disorder (NQD) 36
3.1.3 Model 3: Uncorrelated quenched disorder (UQD) 38
3.1.4 Technical aspects of simulations 38
3.2 Results 39
3.2.1 Model 2: No quenched disorder (NQD) 39
3.2.2 Model 1: Correlated quenched disorder (CQD) 41
3.2.3 Model 1: Finite Size Scaling (FSS) 42
3.2.4 Model 1: Spin Glass and Transition Temperature 43
3.2.5 Model 1: Order by Disorder in the Γ_5 states 46
3.2.6 Model 1: Spin-glass dynamics 49
3.2.7 Model 1: Phase diagram of the CQD model 50
3.2.8 Model 3: Uncorrelated quenched disorder (UQD) 51
3.3 To benchmark simulations with experiments 51
3.4 Bridging the gap between rare-earth pyrochlores 56
3.5 In presence of a magnetic field h 58

4 Spin Liquid design 62
4.1 Model 62
4.2 The tensor and Heisenberg-antiferromagnet spin liquids 62
4.3 Results 65
4.3.1 Specific heat 65
4.3.2 Order parameters and susceptibilities 66
4.4 Structure Factor 70

5 Conclusion 78

A 80
A.1 g-tensor calculations 80
A.2 Finite size scaling (Model 1: Correlated quenched disorder) 82

List of Figures

1.1 Characteristic inverse magnetic susceptibility of a geometrically frustrated antiferromagnet χ^{-1} vs temperature T showing that the transition temperature T_c is much smaller than the Curie-Weiss temperature Θ_{cw}. Adapted from [1] 2

1.2 Ising spins on a triangular lattice showing the six possible configurations for the antiferromagnetic ground state. Arrows indicate the spin direction. Blue lines denote the frustrated bonds, along which spins are parallel. 3

1.3 Kagome lattice composed of corner-sharing triangles 4

1.4 Pyrochlore lattice composed of corner-sharing tetrahedra 4

1.5 Schematic diagram of the phase space of a frustrated magnet, where the solid line represents the ground-state manifold. In the left panel, only a narrow and uniform band of states around the ground state manifold is accessible at low temperatures (blue region); there is no order by disorder here. In the right panel, however, a particular region has a bulge of accessible states at low temperatures. This is the place where soft modes allow low-energy excitations and the corresponding ground state is entropically selected via order-by-disorder.[1] 5

1.6 The A and B sites of pyrochlore materials $A_2B_2Y_7$, forming their own interpenetrating pyrochlore structures. In this thesis, A sites are magnetic, B sites are non-magnetic and Y corresponds to oxygens. Figure taken from [2]. 6

1.7 Classical ground-state phase diagram for a pyrochlore magnet with anisotropic exchange interactions in the limit $J_3 < 0$ and $J_4 = 0$. The blue, green, and red/yellow regions correspond to T_1, T_2, and E ground states respectively. The latter is divided into two colors because of thermal order-by-disorder selection, with ψ_2 (red) and ψ_3 (yellow) states. Points correspond to exchange parameters of $Yb_2Ti_2O_7$, $Er_2Ti_2O_7$ and $Er_2Sn_2O_7$. The grey dots in the center is the position of the tensor spin liquid ($J_3 < 0$ and $J_1 = J_2 = J_4 = 0$). The arrow indicates the asymptotic limit of the Heisenberg antiferromagnet at $J_1 = J_2 > 0$ and $J_3 = J_4 = 0$. Figure adapted from [3] 10

1.8 Spin-configuration in the 4-sublattice non-collinear FM phase with T_1 symmetry, viewed slightly off the [110] axis. The magnetization is aligned with the [001] axis, while spins are canted by an angle θ_{T_1}. Figure from [3]. 11

1.9 Example of a spin configuration within the one-dimensional manifold of states transforming with the E irrep of T_d. The yellow circles represent the local easy plane of each sublattice, perpendicular to the local [111] easy-axis. The U(1) manifold can be generated by a clockwise rotation of all spins around their respective local axes. These configurations are commonly called Γ_5 states. 12
1.10 Spin configurations of antiferromagnetic orders: (a) non-coplanar Ψ_2, (b) coplanar Ψ_3 and (c) coplanar Palmer–Chalker (Ψ_4) states. Ψ_2 and Ψ_3 belong to the U(1) manifold of the Γ_5 states. 13
1.11 The structure of the ground state manifold at the boundary between PC and E phases. The black circle denotes the manifold of E ground states. This manifold branches at the Ψ_2 states (black dots) to connect with three additional U(1) manifolds which include the six Palmer-Chalker states with T_2 symmetry (red dots). Figure from [3]. 14
1.12 Experimental phase diagram of $Er_2Ti_{2-x}Sn_xO_7$ as a function of non-magnetic dilution x showing the two ordered states with E symmetry (Ψ_2 or Ψ_3, red) and with T_2 symmetry (Ψ_4, green). A large part of chapter 3 will be dedicated to analyzing and understanding this phase diagram theoretically. Figure from [4]. 16
1.13 Example of (a) crystalline vs (b) amorphous structures. 17
1.14 Schematic representation of the free energy for a spin glass along an arbitrary line in phase space (labeled by x), showing the presence of many metastable states. 18
1.15 Schematic representation of the correlation function $C(t, t')$ for a paramagnet (blue) and a spin glass (orange). The initial memory of the system is retained in a spin glass system whereas it is quickly forgotten in the case of a paramagnet. 19
1.16 Example of magnetic dilution (left) and stuffing (right) with respectively a missing and extra spin in the lattice. 20

2.1 Boltzmann probability distribution vs energy and temperature 22
2.2 Parallel Tempering scheme 29
2.3 MCMC pipeline, Git : pjeena/Markov-chain-Monte-Carlo 32

3.1 The smallest loop in the lattice encompasses 6 spins of Er ions and each Er-Er bond is shared between two loops. Each of these loops has a non-magnetic ion (B=Ti or Sn) at its center. 35
3.2 Classical ground-state phase diagram for a pyrochlore magnet with anisotropic exchange interactions displaying four distinct ordered phases ($J_3 < 0$ $J_4 = 0$). Points correspond to published estimates of parameters for $Yb_2Ti_2O_7$, $Er_2Ti_2O_7$, and $Er_2Sn_2O_7$ [3]. We want to benchmark an uncorrelated model on the dotted line(with a man walking) in the parameter space. Figure adapted from [3]. 37

3.3 Temperature dependence of specific heat C_v for (a) $0 \leq x \leq 1$ and (b) $1 < x \leq 2$ for the NQD model (no quenched disorder). The sharp peaks at $x = \{1.2, 1.4\}$ are consistent with a first order transition, as confirmed by the discontinuous jump in the T_2 order parameter in Fig. 3.4(b). System size is $L = 4$. 39

3.4 Temperature dependence of (a) m_E and (b) m_{T_2} order parameters for the NQD model (no quenched disorder). The results are consistent with a continuous phase transition into Γ_5 order with E symmetry, and a discontinuous phase transition into Palmer-Chalker order with T_2 symmetry. System size is $L = 4$. 40

3.5 Phase diagram for the NQD model without quenched disorder, showing the competition between Ψ_2 and Palmer-Chalker states. x is an interpolating parameter between the exchange parameters of $Er_2Ti_2O_7$ and $Er_2Sn_2O_7$. The zero-temperature boundary is at $x_c = 1.323$. 40

3.6 Temperature dependence of specific heat C_v for (a) $0 \leq x \leq 1$ and (b) $1.2 \leq x \leq 2$ for the CQD model (correlated quenched disorder). System size is $L = 4$. 41

3.7 Temperature dependence of (a) m_E and (b) m_{T_2} order parameters for the CQD model (correlated quenched disorder). The results are consistent with Γ_5 order with E symmetry for $x \leq 1$ and Palmer-Chalker order with T_2 symmetry for $x \geq 1.8$. Finite size scaling is necessary to clarify the situation for intermediate x values. System size is $L = 4$. 42

3.8 Temperature dependence of the energy for the CQD model (correlated quenched disorder). A symmetry in the energy is observed at low temperatures between x=0.8 and x=2, centered at x=1.4. System size is $L = 4$. 42

3.9 Temperature dependence of m_E (a,c,e,g) and m_{T_2} (b,d,f,h) order parameter of the CQD model for $x = \{0.4, 1, 1.5, 1.8\}$ and $L = \{3, 4, 5, 6, \}$. Inset: Finite-size scaling of the corresponding order parameter at very low temperature. The constant in the scaling function gives the value of the order parameter in the thermodynamic limit. 44

3.10 Value of the parameter c vs x obtained from the finite size scaling analysis (see Eq. 3.4), showing the evolution of the two order parameters, m_E and M_{T_2}, at very low temperature in the thermodynamic limit. There is a region without any long-range order between $x = 1.2$ and 1.6. 45

3.11 Binder cumulant U_b for (a)$x = \{1.2, 1.3, 1.5, 1.6\}$, as defined in Eq. (3.8). The crossing of the curves gives the value of the transition temperature and the associated error bars. 46

3.12 Probability distribution $P(m_{E_x}, m_{E_y})$ of the $\mathbf{m}_E$ order parameter at $T < T_c$ ($T = 0.05$ K) for different x values and system size $L = 10$. A uniform E order would give a circle $|\mathbf{m}_e|^2 = cst = m_{E_x}^2 + m_{E_y}^2$, while Ψ_2 and Ψ_3 orders are given by the full and dashed radial lines respectively, as defined in section 1.2.3.(II.a,b). 47

3.13 Clock-like order parameter m_6 as a function of T for L = 10 and several values of x where m_6 being positive (negative) for the Ψ_2/Ψ_3 states. We clearly see a change in temperature for a given x, until Ψ_2 disappears. 48

3.14 (a) Autocorrelation function $A(t)$ of the CQD model at $T = 0.05$ K, as defined in Eq. 3.10), for several dilution x values. The decorrelation is fast for $x = 0, 0.5, 2$ while it reaches a plateau for $x = 1$ and 1.5. (b) q_{EA} vs x which is analogous to the Edwards-Anderson spin glass parameter. 49

3.15 Phase diagram of the CQD model for $Er_2Ti_{2-x}Sn_xO_7$ obtained from classical Monte-Carlo simulations with Γ_5 (purple, pink and red), Palmer-Chalker (green) and spin-glass (white) phases. The Γ_5 phase is split into Ψ_2 and Ψ_3 orders because of order by disorder. In the region with noticeable disorder $x \in [1.0; 1.2]$, the full U(1) manifold of the Γ_5 phase is recovered, albeit with a fintie fraction fraction of frozen magnetic degrees of freedom. 50

3.16 Temperature dependence of (a,c,e,g) m_E and (b,d,f,h) m_{T_2} order parameters for the UQD model (uncorrelated quenched disorder) with $\alpha_0 = 0.2$, for $x = \{1.2, 1.3, 1.4, 1.5\}$ for system size $L = \{3, 4, 5, 6\}$. 52

3.17 Temperature dependence of (a,c,e,g) m_E and (b,d,f,h) m_{T_2} order parameters for the UQD model (uncorrelated quenched disorder) with $\alpha_0 = 0.1$, for $x = \{1.2, 1.3, 1.4, 1.5\}$ for system size $L = \{3, 4, 5, 6\}$. 53

3.18 Phase diagram of the UQD model for $\alpha_0 = 0.1$ 54

3.19 Phase diagrams for the three models studied in this thesis (a,b,c), compared to experiments on $Er_2Ti_{2-x}Sn_xO_7$ from Ref. [4] (d). The x-axis is always the dilution parameter x (or its equivalent as defined in section 3.1). All the ordered phases are antiferromagnetic, either with E (purple or red) or T_2 (green) symmetry. The white region in panel (a) is a spin glass. 55

3.20 Spin configurations of the antiferromagnetic ordered phases found in the phase diagrams of Fig. 3.19: (a) non-coplanar Ψ_2, (b) coplanar Ψ_3 and (c) coplanar Palmer–Chalker (Ψ_4) states. Ψ_2 and Ψ_3 belong to the U(1) manifold of the Γ_5 states. 56

3.21 Structure factor $S(\mathbf{q})$ obtained from classical Monte Carlo simulation for parameters of $Er_2Ti_2O_7$ (top) and $Er_2Sn_2O_7$ (bottom) at three different temperatures : $T < T_c, T \approx T_c$ and $T > T_c$. 57

3.22 Structure factor $S(\mathbf{q})$ obtained from classical Monte Carlo simulation for $x = 0.5$ at three different temperatures : $T < T_c, T \approx T_c$ and $T > T_c$. The first, second and third row corresponds to the CQD, NQD and UQD models respectively. All models order into Γ_5. For each panel, the color scale goes from zero to the maximum of intensity. 58

3.23 Structure factor $S(\mathbf{q})$ obtained from classical Monte Carlo simulation for $x = 1$ at three different temperatures : $T < T_c, T \approx T_c$ and $T > T_c$. The first, second and third row corresponds to the CQD, NQD and UQD models respectively. All models order into Γ_5. For each panel, the color scale goes from zero to the maximum of intensity. 59

3.24 Structure factor $S(\mathbf{q})$ obtained from classical Monte Carlo simulation for $x = 1.5$ at three different temperatures: $T < T_c, T \approx T_c$ and $T > T_c$. The first, second and third row corresponds to the CQD, NQD and UQD models respectively; the former form a spin glass below T_c (no Bragg peaks), while the other two order into Palmer-Chalker. For each panel, the color scale goes from zero to the maximum of intensity. 60

3.25 Phase diagram of the CQD model in the presence of a magnetic field h in the [001] direction. The transition temperatures are obtained from the peak in specific heat. 61

4.1 Specific heat for the tensor spin liquid and Heisenberg antiferromagnet on a log-log scale. 63

4.2 Reduced susceptibilities $\chi_I T$ for each irrep I and for both TSL and HAF. Temperature is in log scale. Degrees of freedom of a given irrep are allowed to fluctuate at low temperature if this irrep belongs to the ground state. 64

4.3 *Left:* Specific-heat temperature dependence for $x \in [0; 1]$ on a log-log scale, obtained from Monte Carlo simulations of the model with quenched disorder, as defined in section 4.1. *Right:* Zoom at low temperature of the same data on a linear scale. 65

4.4 Scaling function of the specific heat as $T \to 0^+$ (see Eq. 4.4) for $\alpha = -0.25$, showing that the specific heat grows linearly with x. 66

4.5 All order parameters, (a) m_{A_2}, (b) m_E, (c) $m_{T_{1,A}}$, (d) $m_{T_{1,B}}$, (e) m_{T_2}, are zero up to finite-size effects, for all values of x. In particular they are always bounded by the ones of the spin liquids at $x = 0$ or $x = 1$. 67

4.6 Reduced susceptibilities $\chi_I T$ for each irrep $I = \{\mathrm{A}_2$ (a), E (b), $\mathrm{T}_{1,A}$ (c), $\mathrm{T}_{1,B}$ (d), T_2 (e)$\}$, as a function of the temperature T in log scale, and for different dilutions x. Simulations for $T \ll 0.01$ could be difficult to thermalise, which explains the spurious data point at $T = 0.001$ in panel (b). 68

4.7 Temperature dependence of spin glass susceptibility for different x values. 69

4.8 Equal-time structure factor in the [HHL] plane (top) and energy cuts of the inelastic structure factor (bottom) for $x = 0$ (TSL, no quenched disorder). The left and right column in the bottom panels correspond to [HHL] and [H0L] planes respectively. The energies are marked in the lower left corner of each subplot. Pinch lines can be seen at energy E = 0.5 meV 72

4.9 Equal-time structure factor in the [HHL] plane (top) and energy cuts of the inelastic structure factor (bottom) for $x = 0.2$. The left and right column in the bottom panels correspond to [HHL] and [H0L] planes respectively. The energies are marked in the lower left corner of each subplot. Pinch lines have smeared out. 73

4.10 Equal-time structure factor in the [HHL] plane (top) and energy cuts of the inelastic structure factor (bottom) for $x = 0.4$. The left and right column in the bottom panels correspond to [HHL] and [H0L] planes respectively. The energies are marked in the lower left corner of each subplot. We are starting to see similarities with HAF spin liquid. 74

4.11 Equal-time structure factor in the [HHL] plane (top) and energy cuts of the inelastic structure factor (bottom) for $x = 0.6$. The left and right column in the bottom panels correspond to [HHL] and [H0L] planes respectively. The energies are marked in the lower left corner of each subplot. The structure factor possesses patterns reminiscent to the one of the HAF spin liquid, with broad pinch points at low energy that evolve into half-moon patterns at higher energy [5, 6, 7, 8]. 75

4.12 Equal-time structure factor in the [HHL] plane (top) and energy cuts of the inelastic structure factor (bottom) for $x = 0.8$. The left and right column in the bottom panels correspond to [HHL] and [H0L] planes respectively. The energies are marked in the lower left corner of each subplot. This structure factor is very similar to the one of the HAF spin liquid. The main difference is the finite thickness of the pinch points, most likely due to the length scale imposed by the presence of TSL tetrahedra in the system that break the HAF gauge field. 76

4.13 Equal-time structure factor in the [HHL] plane (top) and energy cuts of the inelastic structure factor (bottom) for $x = 1$ (HAF, no quenched disorder). The left and right column in the bottom panels correspond to [HHL] and [H0L] planes respectively. The energies are marked in the lower left corner of each subplot. 77

A.1 Temperature dependence of m_E (a,c,e,g) and m_{T_2} (b,d,f,h) order parameter for different x values with the finite size scaling on the inset. The constant in the scaling function gives the value of the order parameter in the thermodynamic limit. m_{T_2} vanishes for these x values. 82

A.2 Temperature dependence of m_E (a,c,e,g) and m_{T_2} (b,d,f,h) order parameter for different x values with the finite size scaling on the inset. The constant in the scaling function gives the value of the order parameter in the thermodynamic limit. m_{T_2} vanishes for these x values. 83

List of Tables

1.1 Order parameters $\mathbf{m}_\lambda$ of the different irreps [3] expressed in terms of linear combinations of spin-components $\mathbf{S}_i = (S_i^x, S_i^y, S_i^z)$, in the global frame of the cubic crystal axes ($\mathcal{H}_{\mathsf{ex}}$ [Eq. (1.5)]) 8

1.2 Interaction parameters of Hamiltonian (1.5) for $Er_2Ti_2O_7$ and $Er_2Sn_2O_7$ obtained by fitting inelastic neutron-scattering data at high field [9, 10]. 14

3.1 Interaction bonds for the CQD model 36

A.1 Estimates of the components of the g-tensor in the local frame $\mathbf{g}_{\mathsf{local}}$ [Eq. (A.2)], taken from experiments. 80

Chapter 1

Introduction

"People need trouble- a little frustration to sharpen the spirit on, toughen it. Artists do; I don't mean you to live in a rat hole or gutter, but you have to learn fortitude, endurance. Only vegetables are happy".- William Faulkner.

The study of order-disorder phenomena is a fundamental task of equilibrium statistical mechanics [11]. Many studies have dealt with the ordered phases at low temperatures as well as the critical phenomena or hysteresis around phase transitions. However, beyond critical phenomena, there has also been particularly intense research in the understanding of frustrated models, either due to quenched disorder which may lead to spin glasses [12], or due to geometric frustration, with the formation of fluid-like states of matter known as spin liquids [1]. In spin liquids, spins fluctuate even down to zero temperature despite significant correlations. These fluctuations show exotic collective phenomena such as emergent gauge fields [13] and fractional particle excitations.

In this introduction, we will first cover the basics of frustrated magnetism, introduce the main theoretical models, and then present in detail the materials that will be studied in this thesis, namely $Er_2Ti_2O_7$ and $Er_2Sn_2O_7$.

1.1 What is frustration ?

The elementary idea of frustration can be understood from the third law of thermodynamics, which states that the entropy of a system should be zero at absolute zero temperature. In other words, a system is a priori expected to order into a unique configuration. However, the main aspect of frustrated systems is that it is impossible to satisfy all interactions simultaneously. In some cases labeled as *spin liquids*, this competition prevents finding that unique ground state [1].

Please note that in this thesis, we will focus on magnetic frustration, but since magnetic systems also serve as ideal experimental testing grounds for various theoretical models, frustration also has implications in protein folding[14, 15], superconductivity[16] ...

1.1.1 Experimental Intuition

How does it look like in experiments? The most common smoking gun of geometric frustration is probably the temperature dependence of magnetic susceptibility χ. Within mean-field theory, χ^{-1} has the following linear form at high temperature :

$$\chi^{-1} = \frac{1}{c}(T - \Theta_{cw}), \tag{1.1}$$

where Θ_{cw} is the Curie-Weiss temperature that measures the average magnitude of exchange interactions. When an unfrustrated system orders at a given transition temperature T_c, we have $T_c \sim |\Theta_{cw}|$ which is characterized by a cusp or divergence in χ. Contrarily, in geometrically frustrated systems nothing happens at the temperature scale set by interactions, precisely because long-range order (LRO) is hindered by frustration (see Fig. 1.1). This is why one can define a frustration ratio[17]

$$f = \frac{|\Theta_{cw}|}{T_c}. \tag{1.2}$$

We have f $\simeq$ 1 for unfrustrated systems, them being ferro- or antiferromagnetic. On the other hand, a relatively large value of f is a typical signature of frustration. f even goes to infinity for spin liquids since there is no transition, but is often limited to a finite large value in experiments because of perturbations such as quenched disorder, and dipolar interactions ...

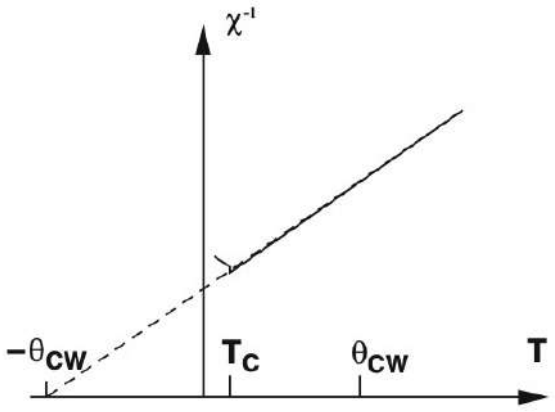

Figure 1.1: Characteristic inverse magnetic susceptibility of a geometrically frustrated antiferromagnet χ^{-1} vs temperature T showing that the transition temperature T_c is much smaller than the Curie-Weiss temperature Θ_{cw}. Adapted from [1]

1.1.2 Canonical frustrated models

Triangular lattice

One of the most famous models was first studied by Wannier[18] back in 1950, where he considered antiferromagnetic (AFM) Ising spins on a triangular lattice. He showed that this spin model has a macroscopic degenerate ground state, i.e. a residual entropy as the system is cooled down to zero temperature. When minimizing the energy of each triangle, one sees easily that two out of the three spins cannot be antiferromagnetically aligned as shown in Fig. 1.2 which results in a frustrated bond (in blue). As a consequence, the six states of Fig. 1.2 have the same, lowest possible, energy. It is possible to pave the entire triangular lattice with these states, and the local degeneracy results in the above-mentioned residual entropy. It is important to notice that this ensemble of ground states does not break any symmetry. Spins are long-ranged correlated but they are not ordered and there is no phase transition at finite temperature in the Ising triangular antiferromagnet.

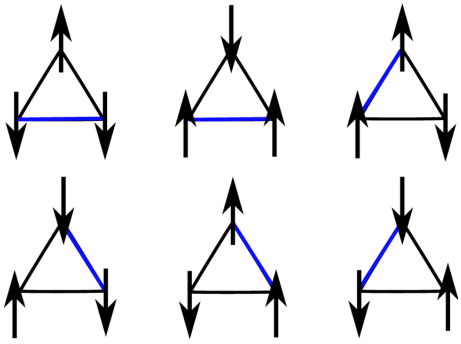

Figure 1.2: Ising spins on a triangular lattice showing the six possible configurations for the antiferromagnetic ground state. Arrows indicate the spin direction. Blue lines denote the frustrated bonds, along which spins are parallel.

Kagome lattice

Since the elementary brick of frustration is the triangle, it is possible to reproduce a similar physics by connecting the triangles by their corners; it results in the kagome lattice shown in Fig. 1.3. With Ising spins, this system is less constrained than the triangular network and presents an even higher residual entropy [19].

Now, if we consider classical Heisenberg spins, the energy is minimized on each triangle when spins are mutually oriented at 120 ° from each other. This ground state remains extensively degenerate, but thermal fluctuations select coplanar states[1, 20]. This selection mechanism is an example of order by disorder[21] which will be discussed in the next section 1.1.3.

Pyrochlore lattice

The triangle is the elementary brick of frustration in two dimensions, but more complex geometries are available in three dimensions, in particular the tetrahedron with four spins

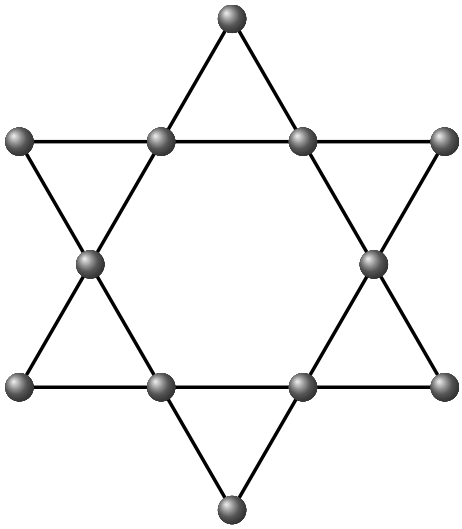

Figure 1.3: Kagome lattice composed of corner-sharing triangles

at equidistance from each other. This thesis will focus on the pyrochlore lattice made of corner-sharing tetrahedra as shown in Fig. 1.4, which has the advantage of being realized in a rich family of rare-earth oxides [22].

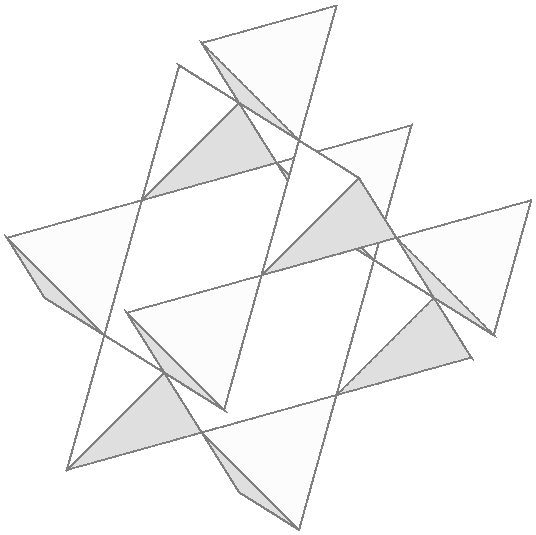

Figure 1.4: Pyrochlore lattice composed of corner-sharing tetrahedra

1.1.3 Order by Disorder(ObD)

The degeneracy of a classical ground state can be fragile since perturbations often lift this degeneracy in favor of an ordered state or a spin glass. But even in the absence of perturbations, thermal and/or quantum fluctuations can lift the degeneracy of the ground state manifold. The selection of an ordered phase by fluctuations is known as order by disorder [21, 23, 20, 24, 25, 26, 9, 27]. It was first studied on the two-dimensional frustrated

Ising model on a domino lattice[21]. At first glance, order by disorder appears to be a paradoxical concept because disorder, caused by fluctuations, tends to suppress order in the system. However, sometimes, fluctuations work in favor of a particular long-range ordered state, as illustrated in Fig. 1.5.

When the degeneracy of a ground-state manifold is accidental, i.e. when it is not protected by the Hamiltonian symmetry, fluctuations around certain ground states differ from others. When this occurs, these particular ground states have a larger entropy (which usually corresponds to more soft modes) or lower zero-point energy for thermal and quantum fluctuations respectively. Focusing on classical systems, the system then has a tendency to be in a region of the ground-state manifold with the highest number of soft modes, which eventually lifts the ground-state degeneracy. Therefore, fluctuations trigger the selection of a particular ground state at low temperatures.

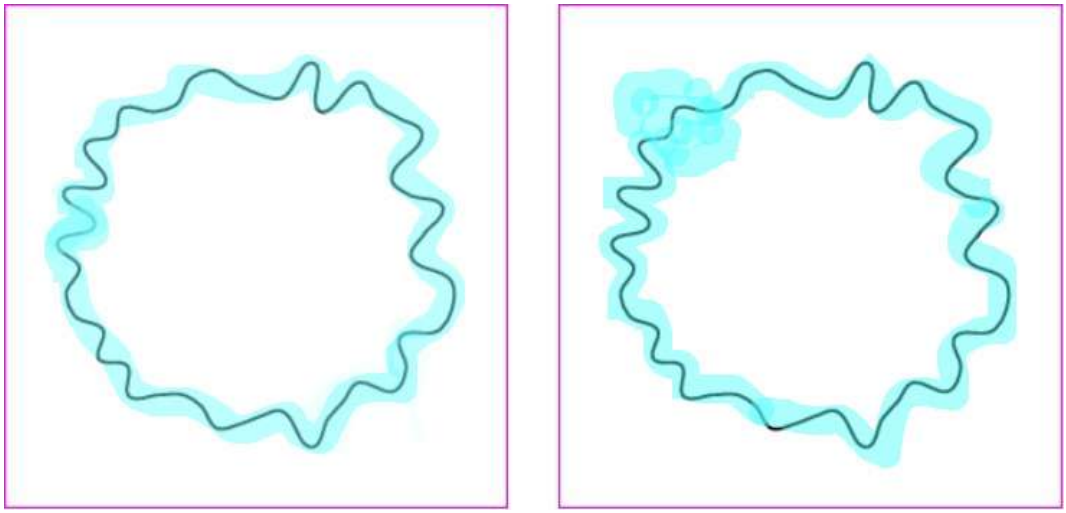

Figure 1.5: Schematic diagram of the phase space of a frustrated magnet, where the solid line represents the ground-state manifold. In the left panel, only a narrow and uniform band of states around the ground state manifold is accessible at low temperatures (blue region); there is no order by disorder here. In the right panel, however, a particular region has a bulge of accessible states at low temperatures. This is the place where soft modes allow low-energy excitations and the corresponding ground state is entropically selected via order-by-disorder.[1]

1.2 The pyrochlore lattice

This thesis will focus on the three-dimensional pyrochlore lattice which has been a major kingpin in the display of geometrical frustration. This is why it is important to understand the geometric and chemical structure of these systems, which is the purpose of this section. The standard pyrochlore lattice is made up of corner-sharing tetrahedra and is commonly observed in rare-earth pyrochlore oxides with a chemical formula $A_2B_2O_7$ [22]. The A site is occupied by a rare-earth ion and the B site is usually non-magnetic. Both A and B ions form their

own pyrochlore structures which are interpenetrating with each other. Examples of diverse phenomena exhibited by $A_2B_2O_7$ materials are [22]: spin glass freezing in $Y_2Mo_2O_7$[28], spin liquid state in $Tb_2Ti_2O_7$[29], spin ice in $Ho_2Ti_2O_7$[30] and $Dy_2Ti_2O_7$[31], order by disorder in $Er_2Ti_2O_7$[9, 26, 32, 33], anomalous Hall effect in $Nd_2Mo_2O_7$[34], superconductivity in $Cd_2Re_2O_7$[35], Kondo effect in $Pr_2Ir_2O_7$[36] etc. The purpose of this section is to provide a broad introduction to the theoretical model of the pyrochlore lattice with classical Heisenberg spins, before moving to the specific materials, $Er_2Ti_2O_7$ and $Er_2Sn_2O_7$.

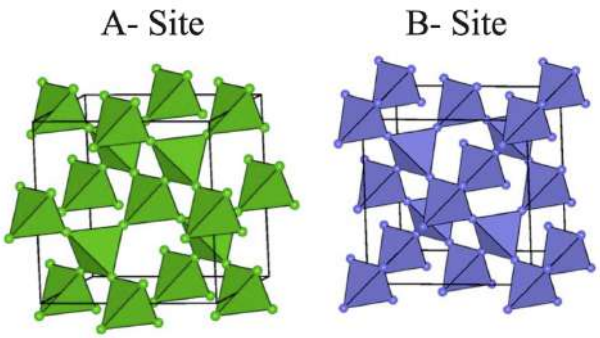

Figure 1.6: The A and B sites of pyrochlore materials $A_2B_2Y_7$, forming their own interpenetrating pyrochlore structures. In this thesis, A sites are magnetic, B sites are non-magnetic and Y corresponds to oxygens. Figure taken from [2].

1.2.1 Generic nearest-neighbor model

Magnetism at the level of a single ion

The magnetic properties of the rare-earth ion A are modulated by the interplay between spin-orbit coupling and the crystal field due to the surrounding oxygens. This leads to immense variations of properties among the rare-earth oxides, which is one of the main reasons for their interest in frustrated magnetism. When the magnetic ion is a Kramers doublet, it can be effectively described by a spin-1/2 degree of freedom [37]:

$$[S^\mu, S^\nu] = i\epsilon_{\mu\nu\xi}S^\xi. \tag{1.3}$$

When S_μ transforms like a magnetic dipole. The real magnetic moment S^μ of the material corresponds to a matrix transformation of S_μ:

$$m_i^\mu = \sum_{\nu=1}^{3} g_i^{\mu\nu} S_i^\nu \tag{1.4}$$

where μ, $\nu \in \{x, y, z\}$. The $g_i^{\mu\nu}$ tensor represents the single-ion anisotropy, from Ising to

Heisenberg passing by XY, and is discussed in Appendix A.

Anisotropy in exchange interactions

The most general model of nearest neighbor interactions compatible with the T_d point group symmetry of the tetrahedron [38, 39, 37] is :

$$\mathcal{H}_{\mathsf{ex}} = \sum_{\langle ij \rangle} J_{ij}^{\mu\nu} S_i^{\mu} S_j^{\nu} = \sum_t \mathcal{H}_{\mathsf{ex}}^{\mathsf{tet}}[t] = \sum_t \sum_{\langle i,j \rangle \in t} \mathbf{S}_i \, \mathbf{J}_{ij}^{[t]} \, \mathbf{S}_j \, , \tag{1.5}$$

where the sum on $\langle i, j \rangle$ runs over the six nearest-neighbor bonds within tetrahedron t. The Hamiltonian can be rewritten as a sum over all tetrahedra because we do not consider interactions beyond first neighbors. $J_{ij}^{[t]}$ is the 3×3 interaction matrix specific to bond ij. It can be shown that $J_{ij}^{[t]}$ is only a function of four independent parameters and that the interaction matrix is the same for all bonds in the lattice (modulo rotation symmetry) [38]. If we label the four spin sublattices within a tetrahedron from 0 to 3, one gets:

$$\mathrm{J}_{01} = \begin{pmatrix} J_2 & J_4 & J_4 \\ -J_4 & J_1 & J_3 \\ -J_4 & J_3 & J_1 \end{pmatrix}, J_{02} = \begin{pmatrix} J_1 & -J_4 & J_3 \\ J_4 & J_2 & J_4 \\ J_3 & -J_4 & J_1 \end{pmatrix}, J_{03} = \begin{pmatrix} J_1 & J_3 & -J_4 \\ J_3 & J_1 & -J_4 \\ J_4 & J_4 & J_2 \end{pmatrix}$$

$$\mathrm{J}_{12} = \begin{pmatrix} J_1 & -J_3 & J_4 \\ -J_3 & J_1 & -J_4 \\ -J_4 & J_4 & J_2 \end{pmatrix}, J_{13} = \begin{pmatrix} J_1 & J_4 & -J_3 \\ -J_4 & J_2 & J_4 \\ -J_3 & -J_4 & J_1 \end{pmatrix}, J_{23} = \begin{pmatrix} J_2 & -J_4 & J_4 \\ J_4 & J_1 & -J_3 \\ -J_4 & -J_3 & J_1 \end{pmatrix},$$

which are all equivalent up to rotation symmetry. Note that the (J_1, J_2, J_3, J_4) parameters are **not** the first, second, third, and fourth nearest-neighbor couplings. They are anisotropic terms of the nearest-neighbor interaction matrix and can be understood as :

- J_1 : XY coupling with respect to the local bond frame.
- J_2 : Ising coupling with respect to the local bond frame.
- J_3 : symmetric off-diagonal exchange (present in dipolar interactions for example).
- J_4 : Dzyaloshinskii-Moriya coupling.

1.2.2 Order parameters

Considering a single tetrahedron, the Hamiltonian becomes a matrix of size 12x12 since we have 4 spins with three components for each spin. This Hamiltonian can then be diagonalized using irreducible representations (irreps) of T_d $\lambda = \{ \mathsf{A}_2, \mathsf{E}, \mathsf{T}_1, \mathsf{T}_2 \}$ [3]:

order parameter	definition in terms of spin components	associated ordered phases
m_{A_2}	$\frac{1}{2\sqrt{3}}(S_0^x+S_0^y+S_0^z+S_1^x-S_1^y-S_1^z-S_2^x+S_2^y-S_2^z-S_3^x-S_3^y+S_3^z)$	"all in-all out"
$\mathbf{m}_{\mathsf{E}}$	$\begin{pmatrix}\frac{1}{2\sqrt{6}}(-2S_0^x+S_0^y+S_0^z-2S_1^x-S_1^y-S_1^z+2S_2^x+S_2^y-S_2^z+2S_3^x-S_3^y+S_3^z)\\ \frac{1}{2\sqrt{2}}(-S_0^y+S_0^z+S_1^y-S_1^z-S_2^y-S_2^z+S_3^y+S_3^z)\end{pmatrix}$	Ψ_2 and Ψ_3
$\mathbf{m}_{\mathsf{T}_{1,\mathsf{A}}}$	$\begin{pmatrix}\frac{1}{2}(S_0^x+S_1^x+S_2^x+S_3^x)\\ \frac{1}{2}(S_0^y+S_1^y+S_2^y+S_3^y)\\ \frac{1}{2}(S_0^z+S_1^z+S_2^z+S_3^z)\end{pmatrix}$	collinear FM
$\mathbf{m}_{\mathsf{T}_{1,\mathsf{B}}}$	$\begin{pmatrix}\frac{-1}{2\sqrt{2}}(S_0^y+S_0^z-S_1^y-S_1^z-S_2^y+S_2^z+S_3^y-S_3^z)\\ \frac{-1}{2\sqrt{2}}(S_0^x+S_0^z-S_1^x+S_1^z-S_2^x-S_2^z+S_3^x-S_3^z)\\ \frac{-1}{2\sqrt{2}}(S_0^x+S_0^y-S_1^x+S_1^y+S_2^x-S_2^y-S_3^x-S_3^y)\end{pmatrix}$	coplanar FM
$\mathbf{m}_{\mathsf{T}_2}$	$\begin{pmatrix}\frac{1}{2\sqrt{2}}(-S_0^y+S_0^z+S_1^y-S_1^z+S_2^y+S_2^z-S_3^y-S_3^z)\\ \frac{1}{2\sqrt{2}}(S_0^x-S_0^z-S_1^x-S_1^z-S_2^x+S_2^z+S_3^x+S_3^z)\\ \frac{1}{2\sqrt{2}}(-S_0^x+S_0^y+S_1^x+S_1^y-S_2^x-S_2^y+S_3^x-S_3^y)\end{pmatrix}$	Palmer-Chalker (Ψ_4)

Table 1.1: Order parameters $\mathbf{m}_\lambda$ of the different irreps [3] expressed in terms of linear combinations of spin-components $\mathbf{S}_i=(S_i^x,S_i^y,S_i^z)$, in the global frame of the cubic crystal axes ($\mathcal{H}_{\mathsf{ex}}$ [Eq. (1.5)])

$$\begin{aligned}\mathcal{H}_{\mathsf{ex}}^{\mathsf{tet}} \;\equiv\; \frac{1}{2}\Big[&a_{\mathsf{A}_2}\,m_{\mathsf{A}_2}^2+a_{\mathsf{E}}\,\mathbf{m}_{\mathsf{E}}^2+a_{\mathsf{T}_2}\,\mathbf{m}_{\mathsf{T}_2}^2+a_{\mathsf{T}_{1,\mathsf{A}}}\,\mathbf{m}_{\mathsf{T}_{1,\mathsf{A}}}^2\\ &+a_{\mathsf{T}_{1,\mathsf{B}}}\,\mathbf{m}_{\mathsf{T}_{1,\mathsf{B}}}^2+a_{\mathsf{T}_{1,\mathsf{AB}}}\,\mathbf{m}_{\mathsf{T}_{1,\mathsf{A}}}\cdot\mathbf{m}_{\mathsf{T}_{1,\mathsf{B}}}\Big],\end{aligned} \tag{1.6}$$

whose eigenvalues

$$\begin{aligned}a_{\mathsf{A}_2} &= -2J_1+J_2-2(J_3+2J_4)\\ a_{\mathsf{E}} &= -2J_1+J_2+J_3+2J_4\\ a_{\mathsf{T}_2} &= -J_2+J_3-2J_4\\ a_{\mathsf{T}_{1,\mathsf{A}}} &= 2J_1+J_2\\ a_{\mathsf{T}_{1,\mathsf{B}}} &= -J_2-J_3+2J_4\\ a_{\mathsf{T}_{1,\mathsf{AB}}} &= -\sqrt{8}J_3\end{aligned} \tag{1.7}$$

are completely determined by the interaction parameters of $\mathcal{H}_{\mathsf{ex}}$ [Eq. (1.5)]; the corresponding eigenvectors $\mathbf{m}_\lambda$ are order parameters given in Table 1.1. However, please note that Eq.

(1.6) is not fully diagonalized because we have a coupling term between the two T_1 irreps. This coupling term can be eliminated by doing a simple coordinate transformation [3] :

$$\begin{aligned} \mathbf{m}_{\mathsf{T}_{1,\mathsf{A}'}} &= \cos\theta_{\mathsf{T}_1}\ \mathbf{m}_{\mathsf{T}_{1,\mathsf{A}}} - \sin\theta_{\mathsf{T}_1}\ \mathbf{m}_{\mathsf{T}_{1,\mathsf{B}}} \\ \mathbf{m}_{\mathsf{T}_{1,\mathsf{B}'}} &= \sin\theta_{\mathsf{T}_1}\ \mathbf{m}_{\mathsf{T}_{1,\mathsf{A}}} + \cos\theta_{\mathsf{T}_1}\ \mathbf{m}_{\mathsf{T}_{1,\mathsf{B}}} \end{aligned} \tag{1.8}$$

where

$$\theta_{\mathsf{T}_1} = \frac{1}{2}\arctan\left(\frac{\sqrt{8}J_3}{2J_1+2J_2+J_3-2J_4}\right). \tag{1.9}$$

The resulting eigenvalues are

$$\begin{aligned} a_{\mathsf{T}_{1,\mathsf{A}'}} &= (2J_1+J_2)\cos^2(\theta_{\mathsf{T}_1}) - (J_2+J_3-2J_4)\sin^2(\theta_{\mathsf{T}_1}) + \sqrt{2}J_3\sin(2\theta_{\mathsf{T}_1}) \\ a_{\mathsf{T}_{1,\mathsf{B}'}} &= (2J_1+J_2)\sin^2(\theta_{\mathsf{T}_1}) - (J_2+J_3-2J_4)\cos^2(\theta_{\mathsf{T}_1}) - \sqrt{2}J_3\sin(2\theta_{\mathsf{T}_1}) \end{aligned} \tag{1.10}$$

Now, we can rewrite the hamiltonian $\mathcal{H}_{\mathsf{ex}}^{\mathsf{tet}}$ as :

$$\mathcal{H}_{\mathsf{ex}}^{[\mathsf{T_d}]} = \frac{1}{2}\left[a_{\mathsf{A}_2}m_{\mathsf{A}_2}^2 + a_{\mathsf{E}}\mathbf{m}_{\mathsf{E}}^2 + a_{\mathsf{T}_2}\mathbf{m}_{\mathsf{T}_2}^2 + a_{\mathsf{T}_{1,\mathsf{A}'}}\mathbf{m}_{\mathsf{T}_{1,\mathsf{A}'}}^2 + a_{\mathsf{T}_{1,\mathsf{B}'}}\mathbf{m}_{\mathsf{T}_{1,\mathsf{B}'}}^2\right]. \tag{1.11}$$

It is important to notice that the constraint on the spin length (S = 1/2) is respected by the order parameters and can be expressed as [3] :

$$\begin{aligned} \mathbf{S}_0^2 + \mathbf{S}_1^2 + \mathbf{S}_2^2 + \mathbf{S}_3^2 &= 1 \\ \mathbf{S}_0^2 + \mathbf{S}_1^2 - \mathbf{S}_2^2 - \mathbf{S}_3^2 &= 0 \\ \mathbf{S}_0^2 - \mathbf{S}_1^2 + \mathbf{S}_2^2 - \mathbf{S}_3^2 &= 0 \\ \mathbf{S}_0^2 - \mathbf{S}_1^2 - \mathbf{S}_2^2 + \mathbf{S}_3^2 &= 0\,. \end{aligned} \tag{1.12}$$

1.2.3 Classical Phase Diagram

Since the Hamiltonian of equation (1.5) can be expressed as a sum of individual tetrahedra, any state that minimizes the energy of each individual tetrahedron is the ground state of the system. In particular, since the spin configurations defined in Table 1.1 are all physical states, i.e. they respect the spin-unit length constraint of Eq.(1.12), it has been shown it was always possible to pave the entire pyrochlore lattice with the same spin configurations on all tetrahedra corresponding to the lowest eigenvalue of Eqs. (1.7) and (1.10) [3]. In other words, there always exist a classical $\mathbf{q} = 0$ ground state for any given exchange interaction (J_1, J_2, J_3, J_4). Please note that even if the spin configuration is the same for all tetrahedra, the spin orientation of the four pyrochlore sublattices might differ.

Many rare-earth pyrochlores are described by $J_3 < 0$ and $J_4 \approx 0$ [40, 9, 37], due to dipolar

interactions and weak Dzyaloshinskii-Moriya coupling. In this limit, the classical ground state phase diagram was obtained in Ref.[3] as shown in Figure 1.7. Now, we will explore the phase diagram and its boundaries ahead.

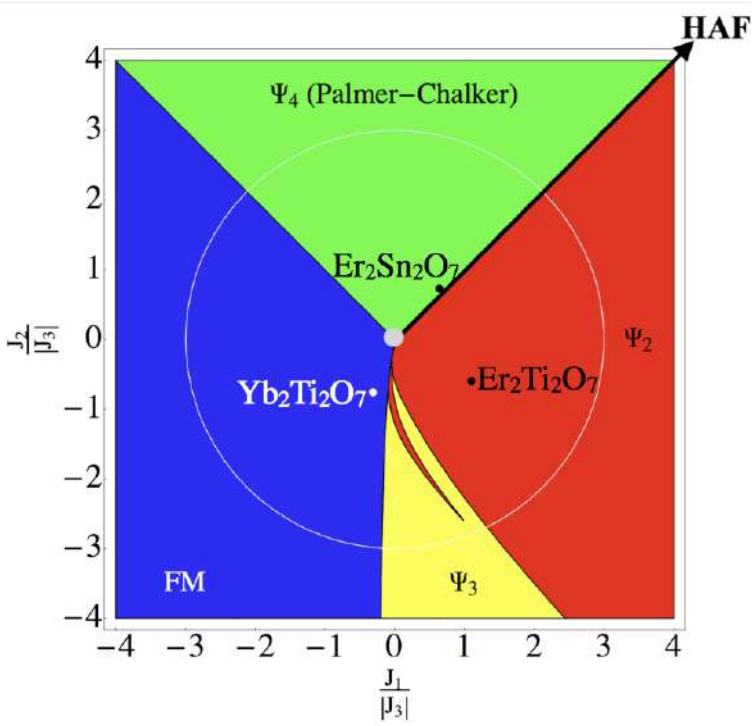

Figure 1.7: Classical ground-state phase diagram for a pyrochlore magnet with anisotropic exchange interactions in the limit $J_3 < 0$ and $J_4 = 0$. The blue, green, and red/yellow regions correspond to T_1, T_2, and E ground states respectively. The latter is divided into two colors because of thermal order-by-disorder selection, with ψ_2 (red) and ψ_3 (yellow) states. Points correspond to exchange parameters of $Yb_2Ti_2O_7$, $Er_2Ti_2O_7$ and $Er_2Sn_2O_7$. The grey dots in the center is the position of the tensor spin liquid ($J_3 < 0$ and $J_1 = J_2 = J_4 = 0$). The arrow indicates the asymptotic limit of the Heisenberg antiferromagnet at $J_1 = J_2 > 0$ and $J_3 = J_4 = 0$. Figure adapted from [3]

(I) Non-collinear ferromagnet (FM) with T_1 symmetry

The classical state in this region has a finite magnetization with $\mathbf{m}^2_{T_{1,A'}} = 1$ and is 6-fold degenerate because of time-reversal symmetry and the three equivalent cubic axes [3]. The magnetization is parallel to one of the three cubic axes, with spins canted away from this axis (see Fig. 1.8). A possible ground state is given below, with magnetization along the [001] axis.

$$\begin{aligned}
\mathbf{S}_0 &= S\left(\sin\theta_{\mathsf{T}_1}/\sqrt{2}, \sin\theta_{\mathsf{T}_1}/\sqrt{2}, \cos\theta_{\mathsf{T}_1}\right) \\
\mathbf{S}_1 &= S\left(-\sin\theta_{\mathsf{T}_1}/\sqrt{2}, \sin\theta_{\mathsf{T}_1}/\sqrt{2}, \cos\theta_{\mathsf{T}_1}\right) \\
\mathbf{S}_2 &= S\left(\sin\theta_{\mathsf{T}_1}/\sqrt{2}, -\sin\theta_{\mathsf{T}_1}/\sqrt{2}, \cos\theta_{\mathsf{T}_1}\right) \\
\mathbf{S}_3 &= S\left(-\sin\theta_{\mathsf{T}_1}/\sqrt{2}, -\sin\theta_{\mathsf{T}_1}/\sqrt{2}, \cos\theta_{\mathsf{T}_1}\right)
\end{aligned} \tag{1.13}$$

where θ_{T_1} is given by Eq. (1.9) and $S = 1/2$. This state has been identified in $Yb_2Ti_2O_7$[41] and $Yb_2Sn_2O_7$[42].

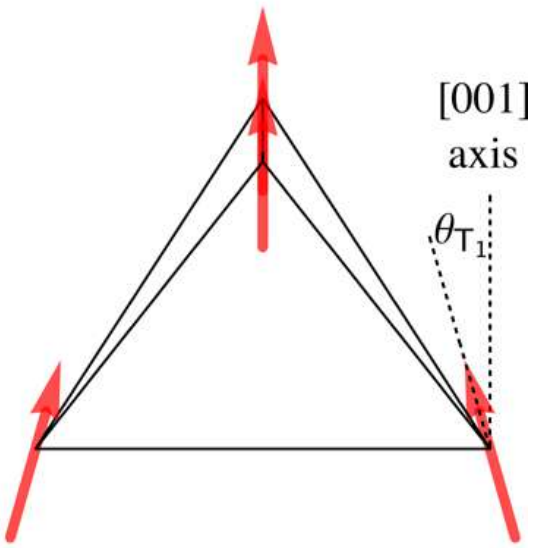

Figure 1.8: Spin-configuration in the 4-sublattice non-collinear FM phase with T_1 symmetry, viewed slightly off the [110] axis. The magnetization is aligned with the [001] axis, while spins are canted by an angle θ_{T_1}. Figure from [3].

(II) Antiferromagnet with E symmetry

The classical state in this region has zero magnetization with $\mathbf{m}_{\mathsf{E}}^2 = 1$ and bears a continuous U(1) degeneracy parametrized by the angle θ_{E} such that [3, 43]

$$\mathbf{m}_{\mathsf{E}} = (\cos\theta_{\mathsf{E}},\ \sin\theta_{\mathsf{E}})\ . \tag{1.14}$$

The spin configuration in this manifold is given by :

$$\begin{aligned}
\mathbf{S}_0 &= S\Big(\sqrt{\frac{2}{3}}\cos(\theta_{\mathsf{E}}),\ \sqrt{\frac{2}{3}}\cos(\theta_{\mathsf{E}}+\frac{2\pi}{3}),\ \sqrt{\frac{2}{3}}\cos(\theta_{\mathsf{E}}-\frac{2\pi}{3})\Big)\\
\mathbf{S}_1 &= S\Big(\sqrt{\frac{2}{3}}\cos(\theta_{\mathsf{E}}),\ -\sqrt{\frac{2}{3}}\cos(\theta_{\mathsf{E}}+\frac{2\pi}{3}),\ -\sqrt{\frac{2}{3}}\cos(\theta_{\mathsf{E}}-\frac{2\pi}{3})\Big)\\
\mathbf{S}_2 &= S\Big(-\sqrt{\frac{2}{3}}\cos(\theta_{\mathsf{E}}),\ \sqrt{\frac{2}{3}}\cos(\theta_{\mathsf{E}}+\frac{2\pi}{3}),\ -\sqrt{\frac{2}{3}}\cos(\theta_{\mathsf{E}}-\frac{2\pi}{3})\Big)\\
\mathbf{S}_3 &= S\Big(-\sqrt{\frac{2}{3}}\cos(\theta_{\mathsf{E}}),\ -\sqrt{\frac{2}{3}}\cos(\theta_{\mathsf{E}}+\frac{2\pi}{3}),\ \sqrt{\frac{2}{3}}\cos(\theta_{\mathsf{E}}-\frac{2\pi}{3})\Big).
\end{aligned} \tag{1.15}$$

with spins restricted to the local easy-plane of each sublattice (see Fig.1.9); it means that spins are orthogonal to their local [111] easy axes.

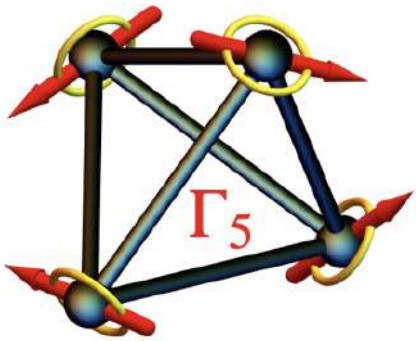

Figure 1.9: Example of a spin configuration within the one-dimensional manifold of states transforming with the E irrep of T_d. The yellow circles represent the local easy plane of each sublattice, perpendicular to the local [111] easy-axis. The U(1) manifold can be generated by a clockwise rotation of all spins around their respective local axes. These configurations are commonly called Γ_5 states.

The antiferromagnetic configurations with E symmetry are sometimes referred to as Γ_5 states. The basis of the E irrep is formed by Ψ_2 and Ψ_3 states [44].

(II.a) Non-coplanar antiferromagnet, Ψ_2, with E symmetry

The Ψ_2 states are six-fold degenerate [43] and given by Eq. (1.15) with $\theta_{\mathsf{E}} = \frac{n\pi}{3}$, $n = 0, 1, 2, 3, 4, 5$. They correspond to the ground state of $Er_2Ti_2O_7$ [43]. See Fig. 1.10(a).

(II.b) Coplanar antiferromagnet, Ψ_3, with E symmetry

The Ψ_3 states are six-fold degenerate[43], with coplanar spins perpendicular to one of the cubic axes. They are given by Eq. (1.15) with $\theta_{\mathsf{E}} = \frac{n\pi}{3} + \frac{\pi}{6}$, $n = 0, 1, 2, 3, 4, 5$. See Fig. 1.10(b).

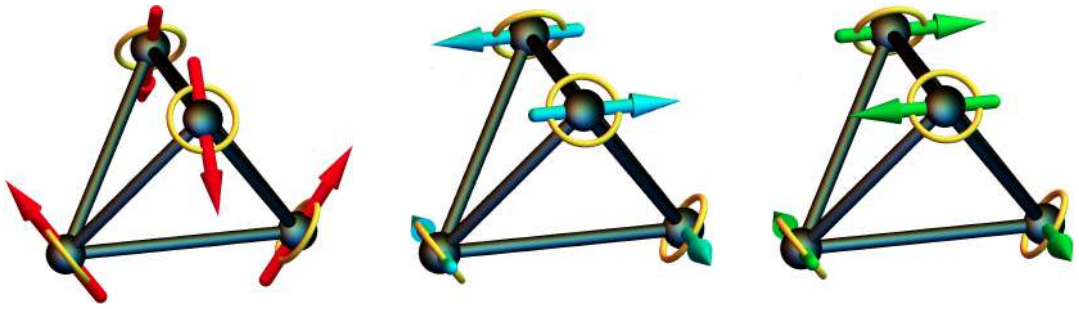

(a) (b) (c)

Figure 1.10: Spin configurations of antiferromagnetic orders: (a) non-coplanar Ψ_2, (b) coplanar Ψ_3 and (c) coplanar Palmer–Chalker (Ψ_4) states. Ψ_2 and Ψ_3 belong to the U(1) manifold of the Γ_5 states.

(III) Palmer-Chalker states with T_2 symmetry

The classical state in this region has zero magnetization with $\mathbf{m}^2_{\mathsf{T}_2} = 1$ and is 6-fold degenerate [45]. One of the six spin configurations is for example:

$$\begin{aligned} \mathbf{S}_0 &= S\left(\frac{1}{\sqrt{2}}, -\frac{1}{\sqrt{2}}, 0\right) \\ \mathbf{S}_1 &= S\left(-\frac{1}{\sqrt{2}}, -\frac{1}{\sqrt{2}}, 0\right) \\ \mathbf{S}_2 &= S\left(\frac{1}{\sqrt{2}}, \frac{1}{\sqrt{2}}, 0\right) \\ \mathbf{S}_3 &= S\left(-\frac{1}{\sqrt{2}}, \frac{1}{\sqrt{2}}, 0\right) \end{aligned} \tag{1.16}$$

This is called a Palmer-Chalker (PC) or Ψ_4 state [45, 44] where the spins are coplanar and arranged in helical fashion in a common [100] plane (see Fig. 1.10(c).). They correspond to the ground state of $Er_2Sn_2O_7$ [46].

(IV) Boundary between Palmer-Chalker phase and E irrep phase

Before moving to the materials, we should briefly discuss the boundary between the Palmer-Chalker phase and E antiferromagnet as it will be of importance later in this thesis. This boundary appears when $a_{\mathsf{E}} = a_{\mathsf{T}_2}$ which implies $\mathrm{J}_1 = \mathrm{J}_2$ for the phase diagram with $J_3 < 0$ and $J_4 = 0$ [3]. It has been shown [3] that the ground states at this boundary can be schematically described by Fig 1.11. The U(1) degeneracy of the E phase (black circle) is enhanced by three additional U(1) degeneracies (red circles), connecting the ψ_2 states (black dots) to the Palmer-Chalker states (red dots). As a consequence, there is an enhancement of

	$Er_2Ti_2O_7$ [9]	$Er_2Sn_2O_7$ [10]
J_1	0.11 meV	0.07 meV
J_2	−0.06 meV	0.08 meV
J_3	−0.10 meV	−0.11 meV
J_4	−0.003 meV	0.04 meV

Table 1.2: Interaction parameters of Hamiltonian (1.5) for $Er_2Ti_2O_7$ and $Er_2Sn_2O_7$ obtained by fitting inelastic neutron-scattering data at high field [9, 10].

soft modes around the ψ_2 states which are then selected via thermal order-by-disorder at finite temperature (see section 1.1.3).

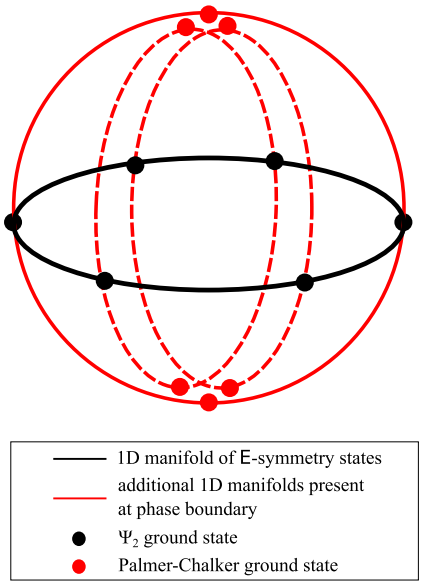

Figure 1.11: The structure of the ground state manifold at the boundary between PC and E phases. The black circle denotes the manifold of E ground states. This manifold branches at the Ψ_2 states (black dots) to connect with three additional U(1) manifolds which include the six Palmer-Chalker states with T_2 symmetry (red dots). Figure from [3].

1.3 Er based pyrochlores

In this section, we shall present the two pyrochlore oxides, $Er_2Ti_2O_7$[9] and $Er_2Sn_2O_7$[10] which form an important part of chapter 3. Their exchange parameters [J_1, J_2, J_3, J_4] have been parametrized in Refs.[9, 10] and are given in Table 1.2

1.3.1 $Er_2Ti_2O_7$

Initial works on $Er_2Ti_2O_7$ confirmed that the material crystallized in the cubic pyrochlore structure. Magnetic susceptibility and specific heat measurements showed that the system orders at $T = 1.25$ K [43, 47, 48], with neutron scattering establishing $Er_2Ti_2O_7$ as a canonical instance of quantum order by disorder [43, 26, 9]. Its orders into the Ψ_2 states defined in Section 1.2.3, which belong to the E irrep with order parameter $\mathbf{m}_E$. The Er^{3+} ion is a Kramers doublet with a substantial easy-plane anisotropy, and $Er_2Ti_2O_7$ is well described by Hamiltonian 1.5 [9]

There have been several studies on $Er_2Ti_2O_7$ in presence of structural disorder. For example, Maryasin and Zhitomirsky[49] studied the effect of non-magnetic dilution and weak bond disorder for the anisotropic XY pyrochlore antiferromagnet. They observed that a small amount of non-magnetic impurities in $Er_2Ti_2O_7$ stabilizes the Ψ_3 states instead of the Ψ_2 ones in the pure material. They also showed that order by structural disorder mechanism competes with the effect of thermal and quantum fluctuations. Andreanov and McClarty[50] studied the effect of substituting nonmagnetic ions onto the magnetic sites in a pyrochlore XY model, for example, $Er_{2-x}Yi_xTi_2O_7$ with a small dilution x of yttrium exhibiting a second order phase transition from the thermally selected Ψ_2 state into a Ψ_3 state selected by the quenched disorder. Andrade, Hoyos, Rachel, and Vojta[51] studied quenched disorder on easy-plane pyrochlore antiferromagnets. They demonstrated that in XY pyrochlore anti-ferromagnets, defects/impurities lead to fluctuating random fields destroying long-range order which leads to a Cluster Glass phase beyond a critical level of randomness. Their results match with experimental studies done on diluted $Er_2Ti_2O_7$.

1.3.2 $Er_2Sn_2O_7$

We now switch our focus to the chemically similar pyrochlore material, $Er_2Sn_2O_7$. Here also the Er^{3+} ion is a Kramers doublet with a substantial easy-plane anisotropy. But as opposed to $Er_2Ti_2O_7$ whose long-range order is particularly robust across samples and experiments, the low-temperature properties of $Er_2Sn_2O_7$ took some time to establish [52, 53, 46]. It is only in 2017 that Refs. [46] and [4] established the presence of long-range order below 130 mK into the Palmer-Chalker states defined in Section 1.2.3. Its order parameter is thus $\mathbf{m}_{T_2}$.

1.3.3 $Er_2Ti_{2-x}Sn_xO_7$

Ref. [4] also showed the evolution of long-range order upon non-magnetic dilution in $Er_2Ti_{2-x}Sn_xO_7$. They found that the critical temperature decreases roughly linearly up to $x \approx 1.7$, with long-range order into the Γ_5 states (with E irrep). Above $x = 1.7$, T_c starts to increase with the emergence of new Bragg peaks consistent with a Palmer-Chalker (Ψ_4) phase.

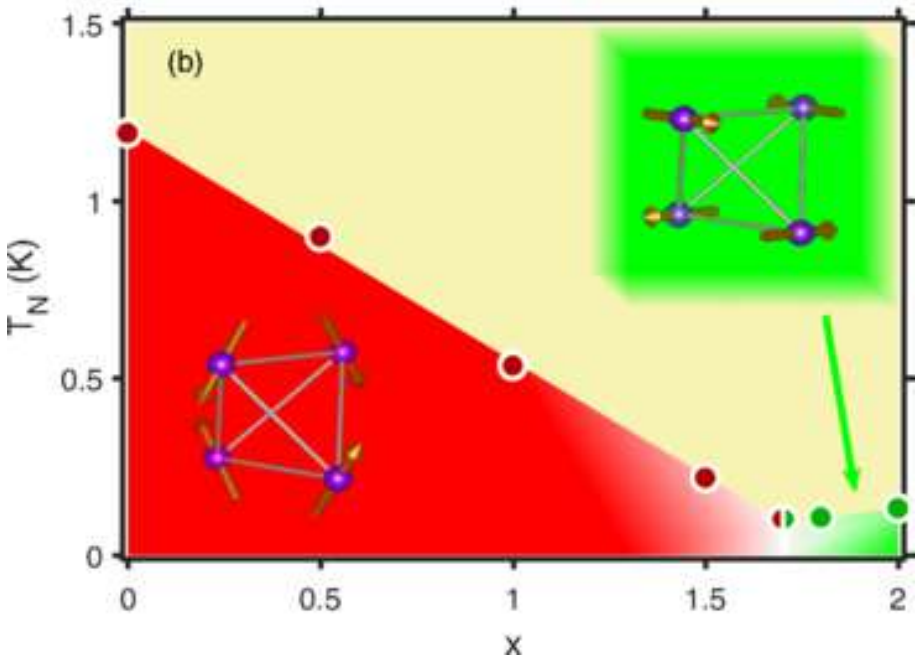

Figure 1.12: Experimental phase diagram of $Er_2Ti_{2-x}Sn_xO_7$ as a function of non-magnetic dilution x showing the two ordered states with E symmetry (Ψ_2 or Ψ_3, red) and with T_2 symmetry (Ψ_4, green). A large part of chapter 3 will be dedicated to analyzing and understanding this phase diagram theoretically. Figure from [4].

1.4 Classical spin liquids on the pyrochlore lattice

Classical spin liquids have, at least theoretically, an infinite frustration parameter f (see Eq. 1.2) [17]. A diversity of such spin liquids has been established on the pyrochlore lattice. Here we shall introduce two specific spin liquids that will be central to chapter 4.

1.4.1 The Heisenberg antiferromagnet

On the classical phase diagram of Hamiltonian (1.5), the Heisenberg antiferromagnet (HAF) corresponds to the asymptotic limit $J_1 = J_2 \gg J_3$, on the boundary between the E and T_2 antiferromagnets (see Fig. 1.7). Taking $J_1 = J_2 = 1$ and $J_3 = J_4 = 0$ in the eigenvalues of Eqs. (1.7) and (1.10), we get :

$$\begin{aligned} a_{\mathsf{A}_2} &= -1 \\ a_{\mathsf{E}} &= -1 \\ a_{\mathsf{T}_2} &= -1 \\ a_{\mathsf{T}_{1,\mathsf{A}}} &= 3 \\ a_{\mathsf{T}_{1,\mathsf{B}}} &= -1 \end{aligned} \tag{1.17}$$

The ground state of the classical HAF naturally includes all antiferromagnetic irreps, A_2, E, T_2, $\mathsf{T}_{1,\mathsf{B}}$. In other words, its ground state manifold can be written as a linear superposition of all of these irreps. It is extensively degenerate and the HAF is a well-known classical spin liquid that remains disordered for all temperatures [54, 55, 56]. The classical HAF model has been realized in a few materials, such as $NaCaNi_2F_7$ [8].

1.4.2 The tensor spin liquid

On the opposite direction of the boundary between the E and T_2 antiferromagnets, at the center of the classical phase diagram in Fig. 1.7 where $J_1 = J_2 = J_4 = 0$ and $J_3 = -1$, we observe a so-called tensor spin liquid [57]. Its name comes from the description of its ground-state manifold that requires an emergent tensor gauge field theory. Its peculiar nature appears in the form of *pinch lines* in its structure factor [57].

Using Eqs. (1.7) and (1.10), the eigenvalues turn out to be :

$$\begin{aligned} a_{\mathsf{A}_2} &= 2\ K \\ a_{\mathsf{E}} &= -1\ K \\ a_{\mathsf{T}_2} &= -1\ K \\ a_{\mathsf{T}_{1,\mathsf{A}'}} &= -1\ K \\ a_{\mathsf{T}_{1,\mathsf{B}'}} &= 2\ K \end{aligned} \tag{1.18}$$

As expected for a point sitting in the center of the phase diagram of Fig. 1.7, the ground state energy is minimized by E, T_2, $\mathsf{T}_{1,\mathsf{A}'}$ irreps.

1.5 Quenched disorder and spin glasses

While most solids studied in condensed matter are crystalline as shown in Figure 1.13(a), the glass that we see in day-to-day life is amorphous (Fig 1.13(b)).

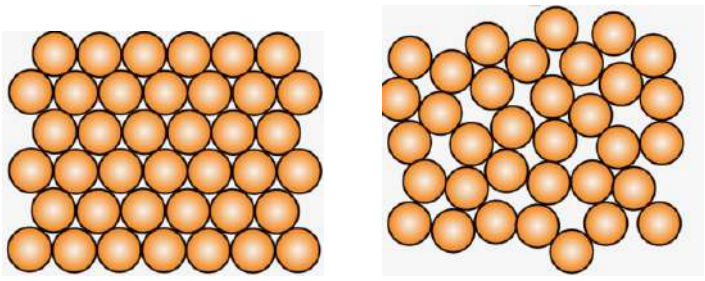

(a) **(b)**

Figure 1.13: Example of (a) crystalline vs (b) amorphous structures.

In amorphous magnetic systems, the Hamiltonian is not invariant by translation anymore.

Spin-spin interactions are randomly distributed, following a given distribution characteristic of the model or material. Since it is not possible to satisfy all interactions in a system with random couplings, amorphous systems are also frustrated; not because of the geometry of the lattice, as considered so far in this chapter, but simply due to the structural disorder of the system. When the Hamiltonian parameters characterizing disorder do not change over time in response to changes in the magnetic degrees of freedom or other parameters, the system is said to be quenched. On the other hand, it is referred to as an annealed disorder if the random variables can be modified. In this thesis, we will focus on quenched disorder.

As a result of this frustration, magnetic moments become frozen in time at low temperatures, even if they remain spatially disordered. This is a spin glass [58, 59, 60, 12] whose physics has been extensively studied in canonical systems such as the Edwards-Anderson model [61], the Sherrington-Kirkpatrick model [62], the spherical model [63], the trap model [64] ... If we plot a free energy landscape of a spin glass system [65], it turns out to be pretty random as illustrated in Fig 1.14. Usually in most physical systems at low temperatures, if we leave the system relaxed for a long enough time, it wants to go to the lowest energy state. On the contrary, spin glass is quite interesting because it has a lot of low-energy states (valleys) but these low-energy states are separated from each other by large energy barriers (mountains). These large energy barriers make it difficult for the system to transition from one state to another. A spin glass appears at low temperatures when the spins get stuck in a particular valley for a very long time.

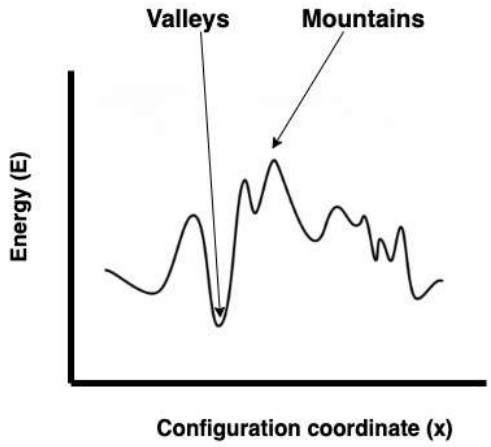

Figure 1.14: Schematic representation of the free energy for a spin glass along an arbitrary line in phase space (labeled by x), showing the presence of many metastable states.

Now, the question one might ask is: How do we identify a spin glass? Spin glasses don't have a spatial order as the spins are randomly aligned so how do we define an order parameter? One solution lies is to look at non-equilibrium dynamics [66]. This can be achieved by performing quenched dynamics and seeing how the spins relax in the system. To be more precise, firstly we define a two-time correlation function[67, 66] $C(t, t')$:

$$C(t,t') = \frac{1}{N}\sum_{i=1}^{N}\overline{\langle S_i(t)S_i(t')\rangle}. \tag{1.19}$$

Here, $S_i(t)$ and $S_i(t')$ are the orientations of spins at times t and t' respectively and N is the number of spins. $\langle O\rangle$ and $\overline{O}$ are respectively the thermal and disorder averages of variable O; the latter is necessary to account for the broken translation symmetry of a spin glass. The value of $C(t,t')$ varies between -1 to 1. Typically, in the case of a paramagnet, the correlation function $C(t,t')$ decays very quickly (see Fig. 1.15). On the contrary, $C(t,t')$ approaches a plateau for a spin glass, which means that the spins are stuck for a very long time.

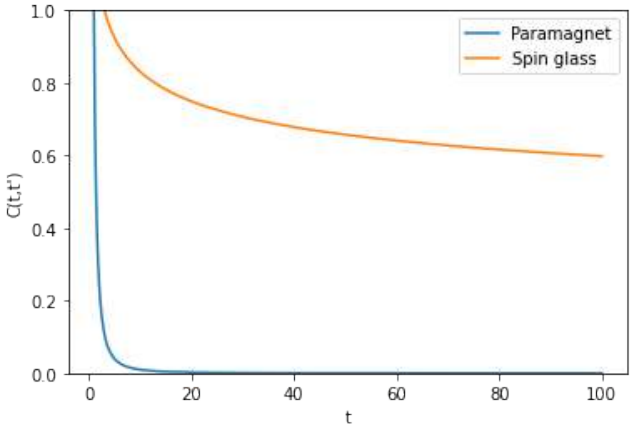

Figure 1.15: Schematic representation of the correlation function $C(t,t')$ for a paramagnet (blue) and a spin glass (orange). The initial memory of the system is retained in a spin glass system whereas it is quickly forgotten in the case of a paramagnet.

We can formalize the above by introducing a new quantity called as Edwards-Anderson spin glass parameter[61] defined as:

$$q_{EA} = \lim_{t-t'\to\infty}\lim_{t'\to\infty} C(t,t') \tag{1.20}$$

If there is a plateau in the correlation function $C(t,t')$, it fixes the value of q_{EA} [66, 68]. The larger the value of q_{EA}, the more glassy the system behaves. The emergence of this plateau in correlation function $C(t,t')$ can be used to characterize the spin glass phase from other phases.

At a microscopic level, one can have various types of defects, such as e.g. magnetic dilution and magnetic stuffing, where a magnetic moment is, respectively, taken out and added to the crystalline structure, as illustrated in Fig. 1.16. These defects can be either accidental or controlled during the synthesis.

In this thesis, we will consider another kind of quenched disorder. All the magnetic ions

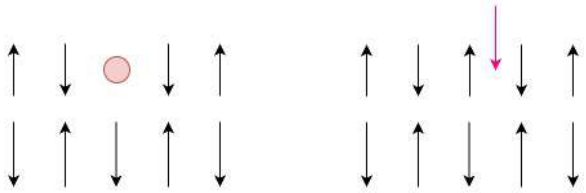

Figure 1.16: Example of magnetic dilution (left) and stuffing (right) with respectively a missing and extra spin in the lattice.

shall remain in place on the pyrochlore lattice, but nonmagnetic ions will be randomly placed. Due to the local variations in the crystalline electric field and superexchange path between magnetic ions, spin-spin interactions will be randomly distributed, reminiscent of an Edwards-Anderson model [61]

1.6 Motivation of this thesis

Most of the literature on geometrically frustrated systems focuses on idealized homogeneous systems. However, realistic systems usually have local random amounts of impurities. Missing ions, dilution, or stuffing are not uncommon in rare-earth pyrochlores and can qualitatively alter a system's properties [69, 70].

In this thesis, we will study the interplay between geometric frustration and quenched disorder. Our goal is to use quenched disorder as a knob to tune the properties of frustrated magnets. First, we will present the methods used in this thesis in chapter 2. In chapter 3 we will focus on an experimentally motivated pyrochlore oxide series $Er_2Ti_{2-x}Sn_xO_7$[4]. We will pay particular attention to generating a phase diagram of $Er_2Ti_{2-x}Sn_xO_7$ and see how the magnetic properties of $Er_2Ti_{2-x}Sn_xO_7$ evolve with x. In chapter 4 we will shift our focus to the two classical spin liquids presented in Section 1.4 and see if we can connect them via quenched disorder. Finally, we conclude with a discussion of the implications of these results and some thoughts about future directions.

Chapter 2

Numerical Methods

2.1 Introduction

The study of statistical properties of complex systems poses many hard problems that are difficult to solve just by analytical approaches. Therefore, numerical simulation techniques such as the Monte Carlo method [71, 72, 73] are indispensable tools to gain a better understanding of complex systems like (spin) glasses, and more generally frustrated magnets.

We are aware of the fact that the magnetic dipoles of the atoms in materials are randomly oriented which results in zero macroscopic magnetic moment. However, in certain cases, such as iron, a magnetic moment is produced as a result of a preferred alignment of the electronic spins. This phenomenon is based on two fundamental but competing principles: energy minimization and entropy maximization [11]. The mediator between these two elements is the temperature which determines the overall dominant term among the two. The Boltzmann distribution function (given below) for a given microstate k governs the relative importance of energy minimization and entropy maximization.

$$P(k) = exp(\frac{-E_k)}{k_b T}) \tag{2.1}$$

which is illustrated in Fig 2.1, here k_b is the Boltzmann constant.

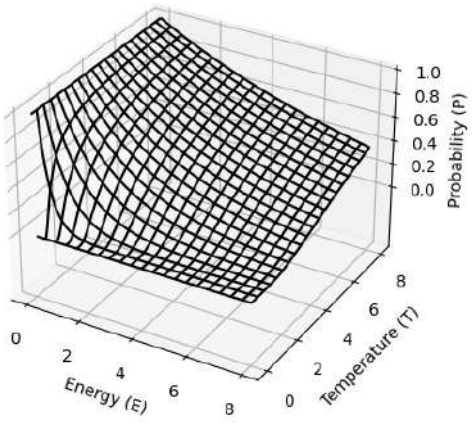

Figure 2.1: Boltzmann probability distribution vs energy and temperature

Given the energy of each possible state k of the system, equation 2.1 gives the probability for the system to be in each possible state (at a given fixed temperature). The macroscopic quantities such as energy, specific heat, etc. can be calculated by doing a weighted summation over all the probabilities. Let's see it through an example:: for any arbitrary fixed state k, let's denote a physical observable O respectively. The expected values of O is given as :

$$< O >= \sum_{k} P(k) O_k \tag{2.2}$$

where O_k is the value of observable O in the microstate k. The above equation seems quite intuitive but lacks practicality. Considering we have a macroscopic number N of classical SO(3) spins, it implies that there is an extensive number of different states. The statistical weight for the majority of configurations is very small and the statistically important configurations would be likely missed. The computations in this way are disconcerting and a waste of computing efforts. A better alternative would be to design a simulation that generates data over the representative states [71]. These representative states will constitute the appropriate proportions of different states. This is a form of a very popular statistical concept called biased sampling where we collect samples favouring some outcomes over others. In simple words:: generated frequency ≡ actual probability. In the next few sections, we explain the approach in detail.

2.2 Sampling procedure and the Metropolis Algorithm

The thermal average for an observable O(x) is defined in the canonical ensemble

$$< O >= \frac{1}{Z} \int e^{-\beta H(x)} O(x) dx \tag{2.3}$$

where x is a position vector in the phase space, $\beta = 1/\mathrm{k}_b\mathrm{T}$ and the partition function Z is given by

$$Z = \int e^{-\beta H(x)} dx \tag{2.4}$$

where the normalized Boltzmann factor is

$$P(x) = \frac{1}{Z} e^{-\beta H(x)} \tag{2.5}$$

This probability gives the statistical weight with which the configuration x occurs in the thermal equilibrium. We want to study the discrete case of the above equations, so equation 2.3 turns out to be of the following form [71]:

$$< O >= \frac{\sum_{i=1}^{n} e^{-\beta H(x_i)} O(x_i)}{\sum_{i=1}^{n} e^{-\beta H(x_i)}} \tag{2.6}$$

Taking n $\rightarrow \infty$(n is the no. of states) would reduce equation 2.6 to equation 2.3. The issue in simple sampling is to overlook the important part of the probability distribution which lies outside the sampling region. So, we need a smarter technique to inculcate the important areas in the phase space. We would like to select points x_i in the phase space with an associated probability, $\mathrm{P}(\mathrm{x}_i)$. Now, we can rewrite equation 2.6 as

$$< O >= \frac{\sum_{i=1}^{n} e^{-\beta H(x_i)} O(x_i)/P(x_i)}{\sum_{i=1}^{n} e^{-\beta H(x_i)}/P(x_i)} \tag{2.7}$$

Now, we can choose $\mathrm{P}(\mathrm{x}_i)$ as $e^{-\beta H(x_i)}$ which would reduce equation 2.7 to a simpler averaging equation.

$$< O >= \frac{\sum_{i=1}^{n} O(x_i)}{n} \tag{2.8}$$

Till now, we have been able to reduce a probability distribution at the equilibrium of the infinite phase space to a representative distribution with a finite set of points from the phase space, x_i. Now the question is: how to generate this representative distribution? This can be achieved by using the concept of Markov chain [74] of successive states $\{\mathrm{x}_i\}$. Each successive state x_{i+1} is constructed from a preceding state x_i via a transition probability $\mathrm{W}(\mathrm{x}_i \rightarrow \mathrm{x}_{i+1})$. In order to implement this idea we need to impose a constraint called detailed balance [75, 76, 71].

$$P_{eq}(x_i) W(x_i \rightarrow x_{i'}) = P_{eq}(x_{i'}) W(x_{i'} \rightarrow x_i). \tag{2.9}$$

This equation ensures that we are in equilibrium implying the probability at arbitrary point

x_i in phase space is time-independent. Since $\mathrm{P}(\mathrm{x}_i) \sim e^{-\beta H(x_i)}$, we can compute the ratio of the transition probabilities since it is only dependent on the difference of the energies of the two states ($\delta H = H(x_{i'}) - H(x_i)$)

$$\frac{W(x_i \to x_{i'})}{W(x_{i'} \to x_i)} = e^{-\delta H \beta} \tag{2.10}$$

The process of engineering the Markov chain in the Metropolis algorithm scheme can be summarized as follows :

- Initialise with a random microstate i with energy E_i.
- Perform a random change(spin flip) in the state i to create a state f.
- Accept or reject the move with the probability $\mathrm{P}_{acceptance} = \min(1, e^{-\Delta E/k_b T})$ where $\Delta E = \mathrm{E}_f$ - E_i

A Monte Carlo simulation is built around these three steps. Starting with a random configuration, the above sequence should be performed multiple times to achieve an equilibrium distribution before starting to measure physical observables. After reaching equilibrium, we can start measuring observables and take an average at the end which gives us the expectation value of the observable. Metropolis [73] algorithm employs importance(biased) sampling which helps in sampling statistically important microstates and increases the efficiency of the simulations.

2.3 Heatbath Method

In the Metropolis [73] algorithm, a random update is based on the change of the energy that follows such configuration change. The acceptance rate thus decreases upon cooling and simulations might become difficult to thermalise at low temperatures. The heatbath[77, 71] approach provides a better way to perform these local spin updates, where the new direction of a spin is drawn from a suitable probability distribution, such that the new configuration energy is automatically distributed according to a Boltzmann weight and is thus always accepted.

Let us assume n local-energy levels, $(\varepsilon_1, \varepsilon_2, \varepsilon_3, \varepsilon_4, ..., \varepsilon_n)$ for a spin. Then the probability of finding the spin in the local energy level j is written as :

$$P_j = \frac{e^{-\varepsilon_j/kT}}{\sum_i e^{-\varepsilon_i/kT}} \tag{2.11}$$

where k_b and T denote respectively the Boltzmann constant and temperature. If a random

number R in the range $0 < \mathrm{R} < 1$ falls into the region

$$\sum_{j=1}^{m-1} P_j < R < \sum_{j=1}^{m} P_j \tag{2.12}$$

we can say that the spin is at level m. When the distribution of the energy levels is continuous, the spin state m is determined by the following equation:

$$R = \int_1^m dj P_j \tag{2.13}$$

The Hamiltonian for our system is given in equation 1.5. Let us denote the local field vector for spin S_i as:

$$H_i^{\mu} = \sum_j J_{ij}^{\mu\nu} S_j^{\nu} \tag{2.14}$$

Then the local Hamiltonian associated with S_i is written as

$$H_{ex,i} = H cos(\theta) \tag{2.15}$$

where $|\mathrm{S}_i| = 1$ and $|\mathrm{H}_i| = \mathrm{H}$. The probability [77] of finding the spin i in an element of solid angle $\mathrm{d}\omega = \sin\,\theta\ \mathrm{d}\theta\ \mathrm{d}\phi$ is written as :

$$P\,(\theta, \phi)\, sin\theta d\theta d\phi = C e^{-H_{ex,i}/kT} sin\theta d\theta d\phi \tag{2.16}$$

where C denotes the normalization constant:

$$1/C = \int_0^{2\pi} d\phi \int_0^{\pi} sin\theta d\theta e^{-H_{ex,i}/kT} \tag{2.17}$$

Thus, θ and ϕ are determined by the following equations:

$$R = \int_0^{2\pi} d\phi^{'} \int_0^{\theta} sin\theta^{'} d\theta^{'} P(\theta^{'}, \phi^{'}) \tag{2.18}$$

$$R' = \phi/2\pi \tag{2.19}$$

where R and R' are random numbers both between 0 and 1. The energy does not depend on the azimuthal angle ϕ that's why it is chosen randomly on the interval $[0,2\pi]$.

Solving equation (2.18), we obtain

$$cos\theta = (1/HK) log[e^{HK}(1-R) + Re^{-HK}] \tag{2.20}$$

where K = J/k_bT. After choosing θ and ϕ, we compute the vector components of the spin and rotate them to the global coordinate system as shown below :

$$\begin{pmatrix} S_i^{x'} \\ S_i^{y'} \\ S_i^{z'} \end{pmatrix} := R(\Theta\Phi\Psi) \begin{pmatrix} S_i^{x} \\ S_i^{y} \\ S_i^{z} \end{pmatrix} \tag{2.21}$$

Finally, we obtain ($S_i^{x'}$, $S_i^{y'}$, $S_i^{z'}$) which is the new thermalized spin. Here, R($\Theta\Phi\Psi$) is the rotation matrix.

Algorithm 1 Heat bath

1: Initialize a configuration of N spins.
2: **Performing a Monte Carlo step :**
3: for i in range(N):
4: Calculate the effective field for a randomly chosen spin.
5: Evaluate θ and ϕ from equation 2.19 and 2.20
6: Compute the new orientation of the spin using θ and ϕ.
7: Collect the value of observables
8: Repeat **Monte Carlo step** for a sufficient number of times and average the accumulated change in observables over the number of spins and the number of Monte Carlo steps

2.4 Over-relaxation

To improve the efficiency of our simulation, we can use over-relaxation[78, 79] techniques alongside other stochastic approaches. We start with calculating the effective interaction vector for a chosen spin from its neighbors and then precess about this vector by an angle θ, θ can either be random or π(extreme rotation), this is usually repeated N($\sim$ no. of spins) times. This algorithm when used together with a stochastic technique, e.g. Metropolis or Heatbath (depending upon the problem), is quite efficient and vectorizes extremely well. Additionally, it also helps to reduce autocorrelations between successive spin configurations.

Algorithm 2 Overrelaxation

1: Choose a spin at random.
2: Calculate the effective field for the selected spin. Let's call it n$_{field}$
3: Rotate the selected spin in step 1 around n$_{field}$ to obtain a new precessed spin.

2.5 Averaging in quenched disorder systems

If a model Hamiltonian depends on random variables other than the regular degrees of freedom, the system is said to have quenched randomness. Usually, these random variables

are kept fixed pertaining to one physical realization of the system(more on this later). Let's consider a doped material A_xB_{1-x}, where a crystal is grown from a melt containing a fraction x of A-atoms and a fraction 1-x of B-atoms. The exchange interactions J_{ij} between spins depend on the type of atoms that are considered: J_{AA}, J_{AB}, or J_{BB}, respectively. Let's denote the occupation variable $c_i = 1$ if site i is occupied by an A-atom and $c_i = 0$ if site i is occupied by a B-atom. We can write the associated Hamiltonian(considering only nearest-neighbor interactions) as follows [71] :

$$H\{S_i, c_i\} = -\sum_{ij} . \{c_i c_j J_{AA} + [c_i(1-c_j) + c_j(1-c_i)]J_{AB} + (1-c_i)(1-c_j)J_{BB}\} S_i S_j \tag{2.22}$$

As we have seen before, the average of the spin configurations are weighted with the Boltzmann factor $e^{-H/kT}$ but we need to associate a different distribution $P(c_i)$ for our occupation variable c_i. The choice of $P(c_i)$ is dependent on the sample preparation in experiments. One can choose c_i to be consistent with the concentration x in the material or with some built-in correlations reflecting 'chemical' short-range order. Therefore, an average of some observable $A(S_i;c_i)$ (e.g. the magnetization) becomes [71]

$$[\langle A(S_i, c_i)\rangle] = \int dc_i P(c_i) \frac{1}{Z(c_i)} \sum_{(S_i)} Tr A(S_i, c_i) e^{-H(S_i,c_i)/kT} \tag{2.23}$$

One needs to carry out a double average for a particular c_i as seen from the above equation : (i) thermal average is done via the importance sampling discussed before (ii) the disorder average $[...]_{av} = \int dc_i P(c_i)...$ which can be achieved by simple sampling.

The solution seems quite straightforward but we need to figure out the frequency of averaging with $P(c_i)$ over the configurations c_i of the quenched disorder variables. In experiments, measurements are carried out for a single probe since the observable quantities are 'self-averaging' [71, 80, 66]. However, the same scheme cannot be applied to simulations since in numerical studies, one mostly considers systems of finite size (L). There is a significant sample-to-sample fluctuation in certain quantities(typically for the order parameter and its susceptibility) which causes a lack of self-averaging. In order to maneuver this, we require a quenched disorder averaging of around $10^2 \sim 10^3$. Monte Carlo simulation of quenched disordered systems is a challenging task; due to the requirement of performing the double averaging procedure over both thermal disorder and quenched disorder, the demand for computer resources is enormous and the judgment of the accuracy is subtle, in particular, due to metastability and slow relaxation at low temperatures.

2.6 Parallel Tempering

The standard method to equilibrate systems with the quenched disorder at low temperatures relies on a slow cooling from high temperature to the temperature of interest. The Parallel tempering[81, 82, 83] algorithm simulates M copies of the original system at different temperatures, with periodic exchanges based on a Metropolis criterion between neighboring temperatures. It is intended for simulating systems with large energy barriers like spin glasses. Replica-exchange [83] moves allow replicas to perform a random walk in temperature space, thereby efficiently overcoming energy barriers. Replicas at high temperatures improve algorithmic mixing, whereas replicas at low temperatures can reach equilibrium on a shorter time scale compared to typical simulations at a fixed low temperature. The performance of the Parallel tempering algorithm is highly dependent on its parameters, including the distribution of replicas in temperature space.

The swapping criterion is based on the detailed balance (equation 2.9). To elaborate, let's take M independent replicas of the system which are simultaneously simulated at different temperature values $T_1, T_2, \ldots, T_M$. The system of M-independent thermal replicas can be treated as an extended ensemble, X = (X_1, X_1,....., X_M) and the partition function:

$$Z = \prod_{m=1}^{M} Z_m \tag{2.24}$$

where Z_m is the partition function of the replica at temperature T_m. The probability of a given configuration X :

$$W(X) = \prod_{m=1}^{M} w(X_m, T_m) \tag{2.25}$$

where

$$w(X_m, T_m) = \frac{1}{Z_m} e^{\frac{-H(X_m)}{k_b T_m}} \tag{2.26}$$

is the probability of configuration X_m in temperature T_m.

The detailed balance equation for a configurational swap between two temperatures T_k and T_l can be written as :

$$W_{kl} P_{kl \to lk} = W_{lk} P_{lk \to kl} \tag{2.27}$$

here, W_{kl} = W(X = $(X_1, ...X_k, X_l, ...X_m)$) and $P_{kl \to lk}$ represents the transition probability between X = $(X_1, ...X_k, X_l, ...X_m)$ and X' = $(X_1, ...X_l, X_k, ...X_m)$.

The swap between two replicas will be accepted by the following probability :

$$P_{accept} = min(1, e^{-\Delta}) \tag{2.28}$$

where $\Delta = (E(X_l) - E(X_k))[\frac{1}{k_b T_k} - \frac{1}{k_b T_l}]$. ΔT must be small enough between the simulated temperatures for the configuration change to occur. If the configurations of thermal replicas k and l are to be exchanged, there must be an overlap between the probability distributions for the temperatures T_k and T_l. Configuration swaps are typically performed between adjacent temperatures because the probability of a configuration exchange reduces as the temperature difference increases. The schematic diagram for PT algorithm is shown in Fig 2.2.

Algorithm 3 Parallel Tempering

1: Initialize an arbitrary temperature set $\{T_1, \ldots, T_i, \ldots, T_M\}$(M is even) in ascending order.
2: Perform 50 MCS for all the temperature points.
3: Swap configurations between T_i and T_{i+1} for $i \in \{1, 3, 5, M-1\}$ with the probability mentioned above.
4: Repeat step 2.
5: Swap configurations between T_i and T_{i+1} for $i \in \{2, 4, 6, M-2\}$ with the probability mentioned above.
6: Repeat steps 2-5 till the required number of MCS.

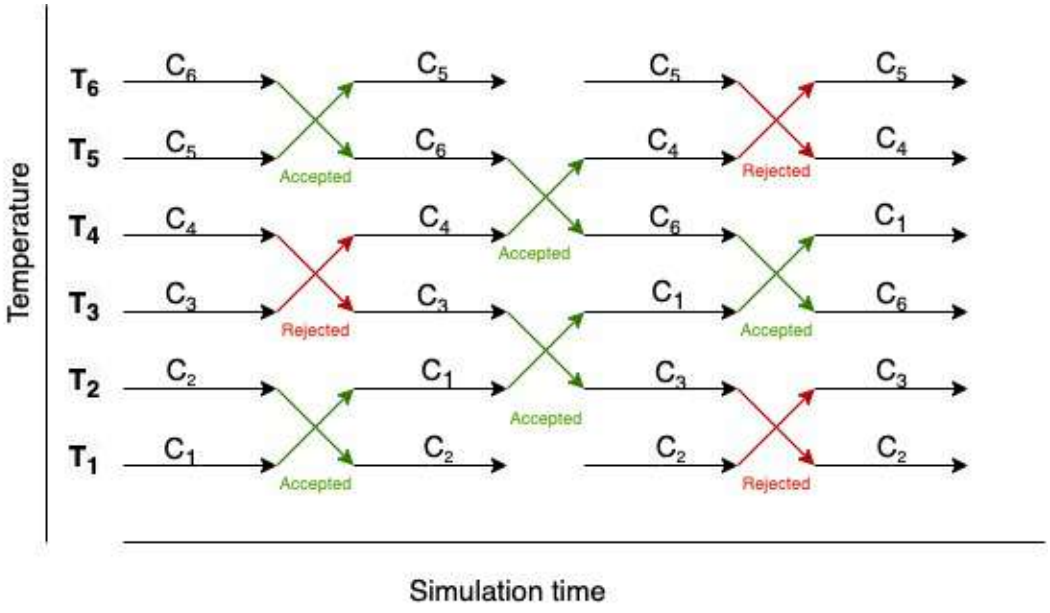

Figure 2.2: Parallel Tempering scheme

In Figure 2.2, we see that several independent replicas are simulated in parallel at different temperatures. At regular time intervals, exchanges of configurations of neighbored replicas are attempted. An exchange between replicas is only accepted when the Metropolis criterion is satisfied. The configuration C_6 at temperature T_6 has moved to a lower temperature T_3 whereas configuration C_1 at temperature T_1 has moved to T_4

2.7 Finite size scaling

One of the limitations that the spin models confront us with is the finite size of our lattice. This results in a problem of recognizing the specific point at which the phase transition occurs. This should be at a theoretical point of divergence but we are limited by the size of the lattice under consideration and thus don't see this divergence. This effect is minimized by using periodic boundary conditions but would only be resolved if we were to consider an infinitely sized lattice as with the associated theoretical values for the phase transition. It is thus necessary to use a construct that will allow us to extrapolate the respective theoretical value given the limited resources of a finite-sized lattice. There are two types of problems, associated with the finite lattice size : (i) errors due to the boundary conditions (ii) mismatch between the critical temperature T_c and the temperature $T_c(L)$ where singularities are observed for the system with characteristic length scale L. We have to study $T_c(L)$ at different system sizes to predict the infinite lattice phase transition point $T_c(L = \infty) = T_c$. Finite-size scaling[71, 84] theory is a powerful scheme to deduce the critical temperature and order parameters at thermodynamic limit.

The correlation length diverges at the critical temperature, $\xi \propto \tau^{-\nu}$, $\tau = |T - T_c|/T_c$ is the reduced temperature. At $\xi = L$, specific heat C and susceptibility χ exhibit a somewhat rounded peak in place of an expected true divergence. We are interested in the critical behavior of the system in the vicinity of the phase transition, which can be extracted from the singular part of the free energy. According to the finite size scaling theory [71] its size dependence is described by the scaling ansatz of the following form :

$$F(L, T, H) = L^{-(2-\alpha)/\nu} F(\tau L^{1/\nu}, H L^{(\gamma+\beta)/\nu}) \tag{2.29}$$

where α, β, γ are the critical exponents. Differentiating F and setting $H = 0$ one gets the scaling form of various thermodynamic functions:

$$M(L, T) \sim L^{-\beta/\nu} M_0(\tau L^{1/\nu}) \tag{2.30}$$

$$\chi(L, T) \sim L^{\gamma/\nu} \chi_0(\tau L^{1/\nu}) \tag{2.31}$$

$$C(L, T) \sim L^{\alpha/\nu} C_0(\tau L^{1/\nu}) \tag{2.32}$$

where M_0, χ_0 and C_0 are fixed scaling functions. At the phase transition ($\tau = 0$), the size dependence reduces to a power law behavior :

$$M_c(L) \sim L^{-\beta/\nu} \tag{2.33}$$

$$\chi_c(L) \sim L^{\gamma/\nu} \tag{2.34}$$

$$C_c(L) \sim L^{\alpha/\nu} \tag{2.35}$$

These functions are the first or second-order moments of the order parameter or energy. Often, we face the problem of determining the transition temperature(from the peak in specific heat) in the first place, and we thus have to implement a different notion in order to ascertain the critical temperature accurately.

The critical temperature can be determined by using the Binder cumulant[71, 84, 85]

$$U_L = 1 - \frac{\langle M^4 \rangle_L}{3\langle M^2 \rangle_L}. \tag{2.36}$$

for an order parameter M and a lattice of size L. In order to estimate critical temperature, one needs to use double precision to achieve considerable accuracy. We use two different system sizes $((L, L'))$ and extract the intersection of $U_L, U_{L'}$, which gives us the critical temperature. The cumulants need to be collected in a temperature window containing the critical temperature. Therefore, an iterative process can be employed in order to narrow down the location of critical temperature.

2.8 Technical details of Monte Carlo simulations

Finally, we present the general flow of our MC simulations. All the simulations were done on the Curta cluster. The cluster has 2x Front-end interactive nodes, 336x compute nodes, 4x bigmem compute nodes, 4x visual nodes, and 4x GPU nodes.

We start with initiating n(suppose 100) Temperature(T) points in n CPU cores. For each T, we generate a random initial spin configuration. Starting deep in the paramagnetic phase, we cool down our spin configuration to the desired T value via simulated annealing, 0.2 10^6 MCS steps were executed for this process. Following that 0.2 10^6 MCS were performed to thermalize the system at temperature T, without storing data. This is followed by 10^6 MCS with Parallel Tempering. The data(energy, specific heat, order parameters, structure factors, etc.) is collected after each MCS and is averaged over a number of MCS. This whole procedure is replicated for a $N_{disorder}$ number of times and the final observables are averaged over $N_{disorder}$ realizations. The full stack program was implemented in Python with subroutines (for heatbath, overrelaxation) in FORTRAN and F2PY was used to connect the subroutines in Python. The Parallel Tempering scheme was implemented via **mpi4py**[86, 87, 88, 89] which is an MPI for Python. A schematic pipeline is shown in Figure 2.3

Final Workflow

Algorithm 4 Complete algorithm to simulate pyrochlore lattice

1: Initialise random spin configurations at different temperatures between a required temperature range.
2: Perform simulated annealing to cool down the spin configurations to the required temperatures using heatbath.
3: Perform equilibration to thermalize the spin configurations
4: Continue with (heath bath + overrelaxation :: 1 MCS) steps with Parallel Tempering. Simulate an adequate amount of MCS to achieve stable results.

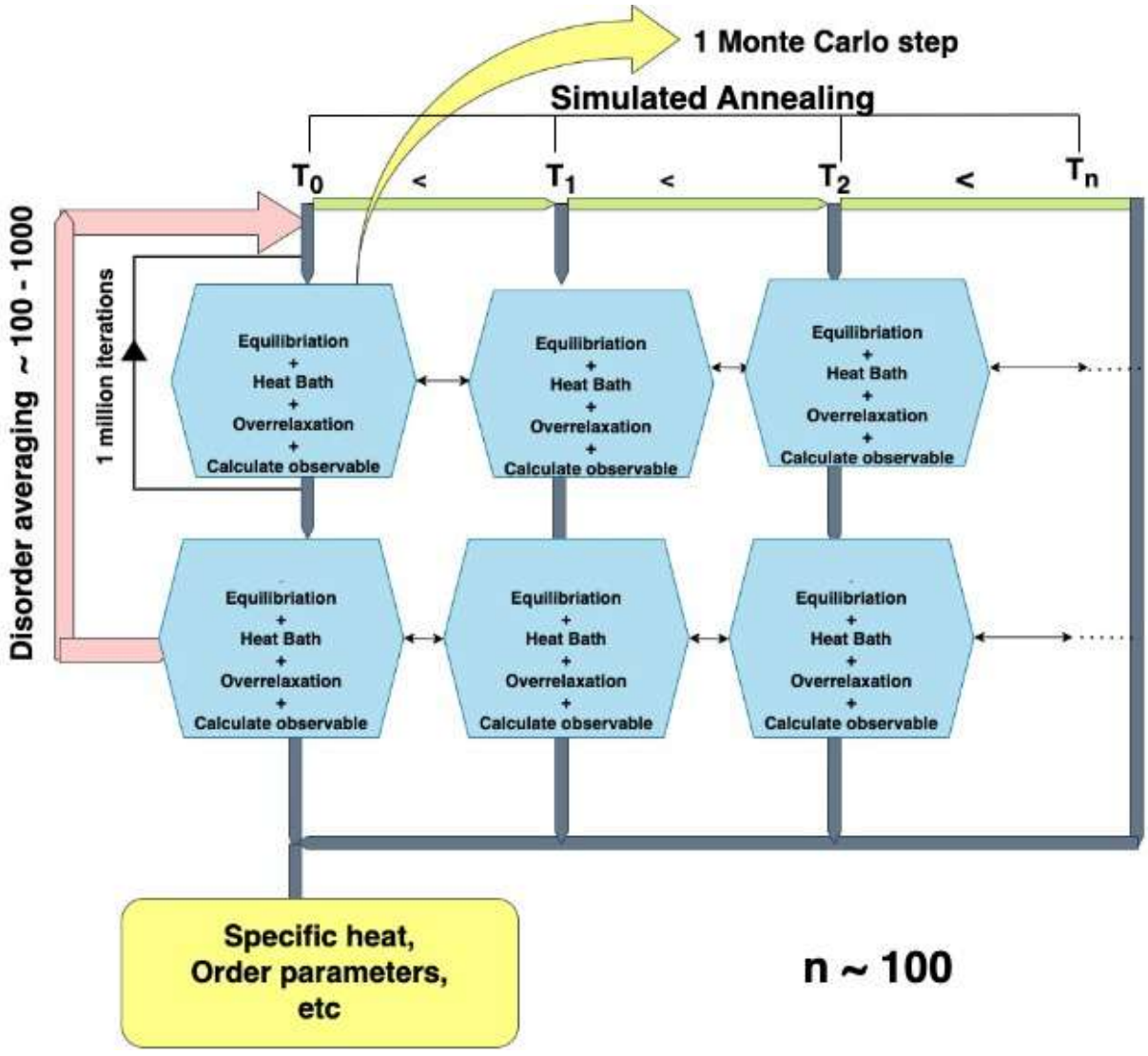

Figure 2.3: MCMC pipeline, Git : pjeena/Markov-chain-Monte-Carlo

2.9 Landau-Lifshitz dynamics

As introduced previously, let us use the local field vector felt by spin $\mathbf{S}_i$: $\mathbf{H}_i = \sum_j \hat{J}_{ij}\mathbf{S}_j$. The equation of motion for this classical spin is given by the Landau-Lifschitz equation of motion [90]:

$$\frac{d\mathbf{S}_i}{dt} = \mathbf{S}_i \times \mathbf{H}_i \tag{2.37}$$

Solving Eq. (2.37) analytically for all spins is impossible in the thermodynamic limit. This is why we shall use a numerical integration, namely the fourth-order Runge-Kutta method [91] where time is divided into equal time steps Δt, making sure that the energy remains constant over time. It means that the Landau-Lifschitz dynamics take place in the microcanonical ensemble (constant energy) and that thermalization of the canonical ensemble thus necessarily comes from the initial seed configurations obtained from Monte Carlo simulations. Using dimensionless units, the numerical solution of equation (2.37) is :

$$\mathbf{S}_i(t+\Delta t) = \mathbf{S}_i(t) + \frac{\mathbf{k}_{1,i}}{6} + \frac{\mathbf{k}_{2,i}}{3} + \frac{\mathbf{k}_{3,i}}{3} + \frac{\mathbf{k}_{4,i}}{6} \tag{2.38}$$

where the vectors $\mathbf{k}_1, \mathbf{k}_2, \mathbf{k}_3, \mathbf{k}_4$ are defined as follow:

$$\mathbf{k}_{1,i} = \mathbf{S}_i \times \mathbf{H}_i \, \Delta t \tag{2.39}$$

$$\mathbf{k}_{2,i} = (\mathbf{S}_i + \frac{\mathbf{k}_{1,i}}{2}) \times (\mathbf{H}_i + \frac{\mathbf{k}_{1,i\ nn}}{2})\Delta t \tag{2.40}$$

$$\mathbf{k}_{3,i} = (\mathbf{S}_i + \frac{\mathbf{k}_{2,i}}{2}) \times (\mathbf{H}_i + \frac{\mathbf{k}_{2,i\ nn}}{2})\Delta t \tag{2.41}$$

$$\mathbf{k}_{4,i} = (\mathbf{S}_i + \mathbf{k}_{3,i}) \times (\mathbf{H}_i + \mathbf{k}_{3,i\ nn})\Delta t \tag{2.42}$$

where $\mathbf{k}_{p,i\ nn} = \sum_j \hat{J}_{ij}\mathbf{k}_{p,j}$ for $p = 1, 2, 3$.

2.10 Structure Factors

The dynamical structure factor, as measured by neutron scattering, is [8, 92] :

$$\begin{aligned}\mathcal{S}(\mathbf{q},\omega) = &\sum_{\mu\nu}(\delta_{\mu\nu} - \frac{q_\mu q_\nu}{q^2}) \\ &\times \frac{1}{2\pi N}\sum_{i,j=1}^{N}\int_{-\infty}^{\infty} dt\, e^{-i\mathbf{q}\cdot(\mathbf{r}_i-\mathbf{r}_j)+i\omega t}\langle s_i^\mu(t)s_j^\nu(0)\rangle.\end{aligned} \tag{2.43}$$

Here, $\mathbf{q}$ denotes the vector in reciprocal space, $\mathbf{r}_i$ and $\mathbf{r}_j$ are the position of spins in the lattice, w is the energy and N number of spins. The thermal average is done by Monte Carlo simulations while the time evolution relies on Landau-Lifschitz dynamics.

Chapter 3

Non-magnetic dilution in $Er_2Ti_{2-x}Sn_xO_7$

The rare earth pyrochlore structure is fairly common in nature and is also of significant interest for magnetic properties. The optimal pyrochlore formula is $A_2B_2X_7$ where A is a rare earth ion, B is usually a non-magnetic ion, and X is an anion such as oxygen. The rare earth metal pyrochlore oxides provide an intriguing platform for studying the interplay of geometric frustration and spin-orbit interaction. In recent times, progress has been observed in the synthesis of new rare-earth pyrochlores. These geometrical frustrated pyrochlore structures have attracted considerable attention over the past decades due to their exotic magnetic properties, e.g. spin ices, spin liquids, and noncollinear XY orders.

The two pyrochlore oxides, $Er_2Ti_2O_7$ [43, 93, 9, 26, 94, 95, 96] and $Er_2Sn_2O_7$ [10, 97, 46, 4], form the central pillars of this chapter. $Er_2Ti_2O_7$ is an antiferromagnetic insulator with an ordering temperature near $T_N \sim 1.2$ K, it undergoes a phase transition to a non-coplanar Ψ_2 antiferromagnetic ordered state. As for $Er_2Sn_2O_7$, it was shown to order below 130 mK in the Palmer-Chalker (Ψ_4) configuration [46, 4].

An experimental study on a pyrochlore series $Er_2Ti_{2-x}Sn_xO_7$[4] formed by the dilution of non-magnetic(B:: Ti/Sn) ions using heat capacity, ac susceptibility, and neutron scattering. This chapter explores a similar standpoint bridging a path between $Er_2Ti_2O_7$ and $Er_2Sn_2O_7$ via a chemical dilution parameter x. Motivated by the above experiments on $Er_2Ti_{2-x}Sn_xO_7$, the idea is to tune the Hamiltonian of our system via non-magnetic dilution x; in other words, to use impurities as a knob to explore unknown parts of the phase diagram.

The organization of this chapter is as follows: first, we briefly introduce the different models which we considered to study $Er_2Ti_{2-x}Sn_xO_7$. Then we present the results of our Monte Carlo simulations of the system. In particular, we present the specific heat, critical temperature, and subsequently the $x - T$(temperature) phase diagram. In the subsequent sections, we compare the structure factor and semi-classical spin dynamics calculations for the different models demonstrating the legitimacy of our theory. We also explore the specific heat dependence on chemical dilution x and the $h - T$ phase diagram in the presence of magnetic field $\mathbf{h}$. Finally, our findings, comparisons, predictions, and future directions are summarised in the last section.

3.1 Models

We assume that the magnetic ions Er^{3+} are in stoichiometric proportions in the system, without any missing spins or stuffed impurities. In other words, the pyrochlore structure of the magnetic moments is conserved, and the structural disorder only comes from Ti^{4+} and Sn^{4+}. The main question is thus how to model the quenched, disordered, positions of these non-magnetic ions into the microscopic Hamiltonian.

3.1.1 Model 1: Correlated quenched disorder (CQD)

In this first model, we will induce chemical disorder by choosing the type of interaction depending on its local surroundings. It is impossible to perform robust ab initio estimates for a structurally disordered structure made of 4f magnetic ions. However, we can build a minimal model to extract the essential physics of the non-magnetic dilution.

The pyrochlore lattice is made of corner-sharing tetrahedra, but can also be seen as an ensemble of bond-sharing hexagons (see Fig 3.1). Each bond between two Er^{3+} ions belongs to exactly two hexagons, and it is at the center of these hexagons that lie the non-magnetic ions.

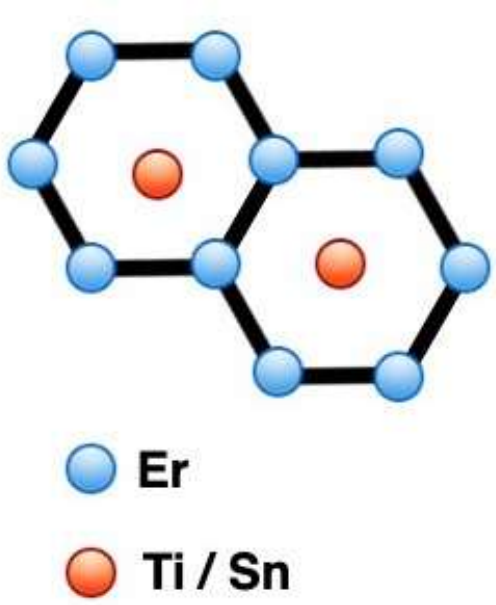

Figure 3.1: The smallest loop in the lattice encompasses 6 spins of Er ions and each Er-Er bond is shared between two loops. Each of these loops has a non-magnetic ion (B=Ti or Sn) at its center.

We shall fix the matrix coupling $\hat{J}_{ij}$ of this bond between spins i and j based on the nature of these two neighboring non-magnetic ions, following the rules of Table 3.1. If the two ions are Ti (resp. Sn), we take the matrix coupling of $Er_2Ti_2O_7$ (resp. $Er_2Sn_2O_7$) as defined in Table 1.2. If the two ions are one Ti and one Sn, then we choose the average value of each

term (J_1, J_2, J_3, J_4).

Table 3.1: Interaction bonds for the CQD model

Local environment	Coupling parameters
Ti-Ti	J_1 = 0.11 meV, J_2 = -0.06 meV, J_3 = -0.10 meV, J_4 = -0.003 meV
Sn-Sn	J_1 = 0.07 meV, J_2 = 0.08 meV, J_3 = -0.11 meV, J_4 = 0.04 meV
Ti-Sn/Sn-Ti	J_1 = 0.09 meV, J_2 = 0.01 meV, J_3 = -0.105 meV, J_4 = 0.0185 meV

This model neglects the influence of further non-magnetic ions B and assumes a relatively simple variation of the matrix coupling when the bond is surrounded by both Ti and Sn. But it has the notable merit (i) of accounting for the correlated nature of the disorder since the six bonds of a hexagon necessarily share the same non-magnetic ion B, and (ii) to include realistic values for coupling parameters, obtained by independent inelastic neutron scattering experiments on $Er_2Ti_2O_7$ [9] and $Er_2Sn_2O_7$ [10]. In order to implement this model in simulations, the algorithm will go as follows

Algorithm

1. There are two interpenetrating pyrochlore lattices, A and B, made respectively of magnetic ions A=Er^{3+} and of non-magnetic ions B=Ti^{4+} or Sn^{4+}.
2. For a given sample and a given dilution x, we randomly fix the nature of the non-magnetic ions on the B pyrochlore lattice with the following probability: $x/2$ for Sn^{4+} and $(1 - x/2)$ for Ti^{4+} ions.
3. Once the quenched disorder is fixed, we go through each of the $3N$ bonds on the A pyrochlore lattice (where N is the number of Er magnetic moments) and check the nature of the two neighboring non-magnetic ions on the B pyrochlore lattice. We fix the matrix coupling $\hat{J}_{ij}$ between spins i and j following the rules of Table 3.1. The Hamiltonian of this sample is now uniquely fixed.
4. We do Monte Carlo simulations for this sample and store the thermally averaged observables.
5. We repeat processes 2, 3 and 4 for quenched-disorder average.

3.1.2 Model 2 : No quenched disorder (NQD)

One of our motivations in this thesis is to see if we can use disorder, more precisely non-magnetic dilution, as a knob to explore the pyrochlore phase diagram beyond pristine compounds. In other words, any $A_2B_2O_7$ material only gives access to a given point of the phase diagram in Fig. 3.2. Here we want to create a bridge between these scattered points, using the dilution x as a tuning variable, to access the physics in regions of the phase

diagram that are otherwise inaccessible. But to check the validity of our approach, we need to know, at least theoretically, what these intermediate regions look like.

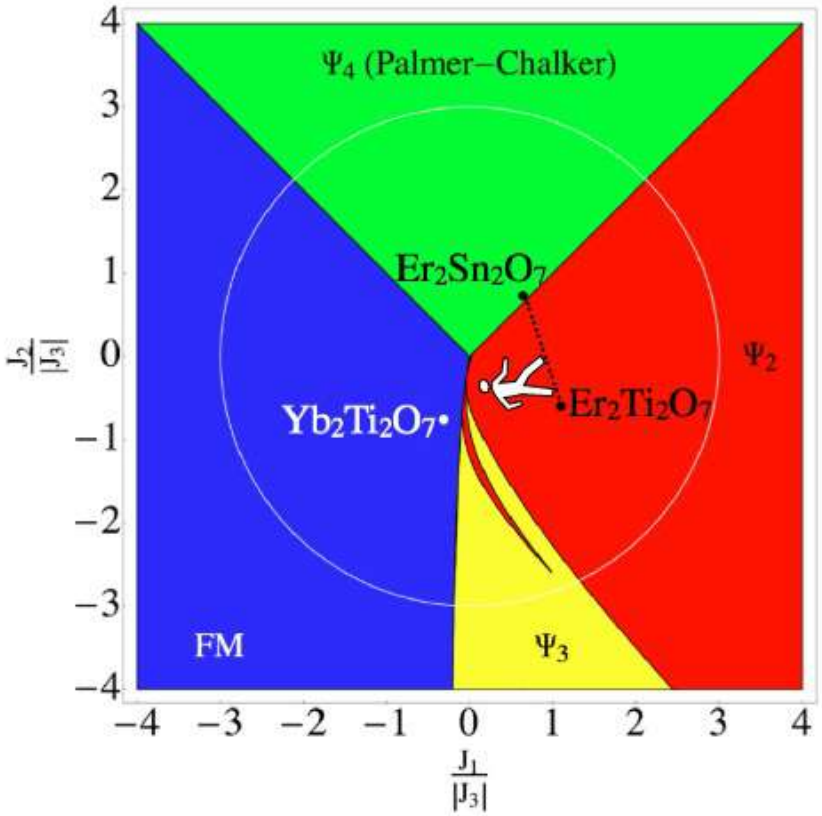

Figure 3.2: Classical ground-state phase diagram for a pyrochlore magnet with anisotropic exchange interactions displaying four distinct ordered phases ($J_3 < 0$ $J_4 = 0$). Points correspond to published estimates of parameters for $Yb_2Ti_2O_7$, $Er_2Ti_2O_7$, and $Er_2Sn_2O_7$ [3]. We want to benchmark an uncorrelated model on the dotted line(with a man walking) in the parameter space. Figure adapted from [3].

This is why we introduce this second model *without* any quenched disorder. Now, x acts as a connecting parameter between the exchange parameters of $Er_2Ti_2O_7$ and $Er_2Sn_2O_7$ (see the dotted line with a walking man in Fig. 3.2). For a given x, all the bonds in the whole pyrochlore lattice have the same exchange parameters, given by:

$$J_x = J_{\text{ETO}} + \frac{J_{\text{ESO}} - J_{\text{ETO}}}{2} x \tag{3.1}$$

where ETO and ESO stand for $Er_2Ti_2O_7$ and $Er_2Sn_2O_7$ respectively. It gives:

$$\begin{aligned} J_{1,x} &= -0.02x + 0.11 \\ J_{2,x} &= 0.07x - 0.06 \\ J_{3,x} &= -0.005x - 0.10 \\ J_{4,x} &= 0.0215x - 0.003 \end{aligned} \tag{3.2}$$

Since this model has no disorder, simulations do not require disorder average and the Monte Carlo algorithm is as explained in chapter 2.

3.1.3 Model 3: Uncorrelated quenched disorder (UQD)

Finally, we shall introduce a third model as an alternative Hamiltonian to include quenched disorder, in order to see which one compares best to experiments. This UQD model can be seen as an Edwards-Anderson version of Hamiltonian (1.5), implemented as follows:

Algorithm

1. For a given dilution x, we start from the disorder-free model NQD with a uniform interaction matrix whose coupling parameters are defined in Eqs. (3.2).
2. Then, for each coupling parameter $\{J_{1,x}, J_{2,x}, J_{3,x}, J_{4,x}\}$ of each Er-Er bond in the pyrochlore lattice, we add a perturbations $\Delta_{i,x}$ with $i = 1, 2, 3, 4$. There are thus $(4 \times 3N) = 12N$ random variables for each sample. This noise variable $\Delta_{i,x}$ is chosen randomly in the range $[-\alpha_0 J_{i,x}\ ;\ +\alpha_0 J_{i,x}]$. In order to study different strengths of disorder, we consider three cases where $\alpha_0 = \{0.1, 0.2, 0.3\}$.
3. We do Monte Carlo simulations for this sample and store the thermally averaged observables.
4. We repeat processes 2 and 3 for quenched-disorder average.

3.1.4 Technical aspects of simulations

The general algorithm was described in chapter 2 and present here only details of the simulations. We first start with a random spin configuration at high temperature and perform simulated annealing to the required finite temperature T. After that, we equilibrate for 2.10^5 MCS and omit the next 2.10^5 MCS for thermalization. We measured specific heat, susceptibility, neutron-scattering structure factor, and order parameters and also performed spin dynamics. The temperature range for our simulations was $10^{-2} \leq \mathrm{T/J} \leq 1.0$. System sizes, specified by the linear dimension L in units of the lattice constant and by the number of spins $\mathrm{N}_s = 16.\mathrm{L}^3$, are $3 \leq \mathrm{L} \leq 10$ and $432 \leq \mathrm{N}_s \leq 16000$. Run lengths for data collection are 10^6 MCS and the results are averaged over a number of disorder realizations varying from 200 for L = 3 to 100 for L = 10.

3.2 Results

We will now present the results for the three different models, and compare them together and with the experimental phase diagram in section 3.3.

3.2.1 Model 2: No quenched disorder (NQD)

We shall start with the NQD model to serve as benchmark of the underlying physics *in absence of* quenched disorder. As explained previously and illustrated in Fig 3.2, x is here a variable in parameter space connecting $Er_2Ti_2O_7$ to $Er_2Sn_2O_7$. All bonds in the lattice have the same coupling parameters given by Eq. (3.2).

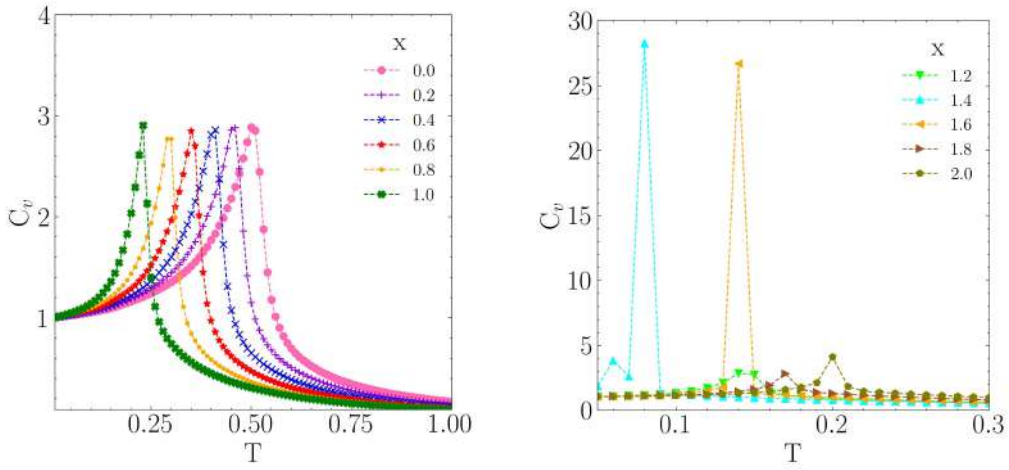

(a) **(b)**

Figure 3.3: Temperature dependence of specific heat C_v for (a) $0 \leq x \leq 1$ and (b) $1 < x \leq 2$ for the NQD model (no quenched disorder). The sharp peaks at $x = \{1.2, 1.4\}$ are consistent with a first order transition, as confirmed by the discontinuous jump in the T_2 order parameter in Fig. 3.4(b). System size is $L = 4$.

According to the specific heat in Fig. 3.3 and the evolution of the order parameters in Fig. 3.4, the system orders into Γ_5 states with E symmetry for $0 \leq x \leq 1.2$ and into Palmer-Chalker states with T_2 symmetry for $1.4 \leq x \leq 2$. The zero-temperature boundary between the two phases can be determined exactly by computing the value x_c where the energy eigenvalues of the E and T_2 irreps become degenerate (see Eqs. (1.7)),

$$a_{\mathsf{E}} = a_{\mathsf{T}_2} \Leftrightarrow -J_1 + J_2 + 2J_4 = 0, \tag{3.3}$$

and then injecting the values of the coupling parameters of Eq. (3.2). We find $x_c = 1.323$, which is consistent with simulations.

As explained in Fig. 1.11, there is always an enhancement of the ground-state degeneracy at the boundary x_c between E and T_2 phases, with additional soft modes around the Ψ_2 states. This is why thermal order-by-disorder lifts the U(1) degeneracy of the ground states with E

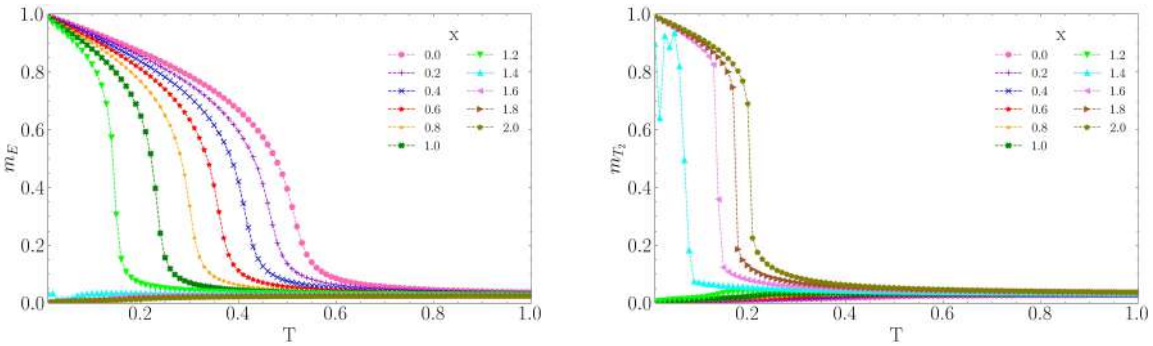

(a) **(b)**

Figure 3.4: Temperature dependence of (a) m_E and (b) m_{T_2} order parameters for the NQD model (no quenched disorder). The results are consistent with a continuous phase transition into Γ_5 order with E symmetry, and a discontinuous phase transition into Palmer-Chalker order with T_2 symmetry. System size is $L = 4$.

symmetry, and entropically selects Ψ_2 states in the left part of the phase diagram in Fig. 3.5. In particular Ψ_2 configurations are ground states at x_c, and this order persists at finite temperature for values just above x_c. This is why the boundary between Ψ_2 and Palmer-Chalker phases bends towards larger values of x in the phase diagram of Fig. 3.5. It also explains why simulation data in Figs. 3.3 and 3.4 are a bit more noisy at $x = 1.4$ than other values, because this is where the competition between the two types of antiferromagnetic orders is the strongest.

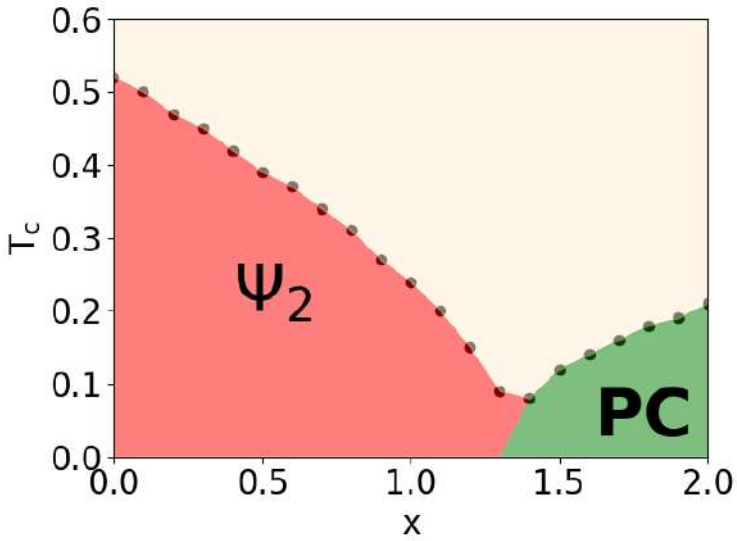

Figure 3.5: Phase diagram for the NQD model without quenched disorder, showing the competition between Ψ_2 and Palmer-Chalker states. x is an interpolating parameter between the exchange parameters of $Er_2Ti_2O_7$ and $Er_2Sn_2O_7$. The zero-temperature boundary is at $x_c = 1.323$.

3.2.2 Model 1: Correlated quenched disorder (CQD)

Now let us consider our first model with quenched disorder, where there are three types of couplings depending on the neighboring non-magnetic ions: the coupling parameters of $Er_2Ti_2O_7$, of $Er_2Sn_2O_7$, or the mean value between the two (see Table 3.1).

Some regions of the phase diagram are reminiscent of the NQD model (no quenched disorder) studied in the previous section. In particular, the specific heat and order parameters confirm the presence of E order for $x \leq 1$ and T_2 order for $x \geq 1.8$ (see Figs. 3.6 and 3.7). But in the intermediate range $1.2 \leq x \leq 1.6$, both order parameters drop noticeably and the specific heat presents no sharp peak, but a broad bump instead.

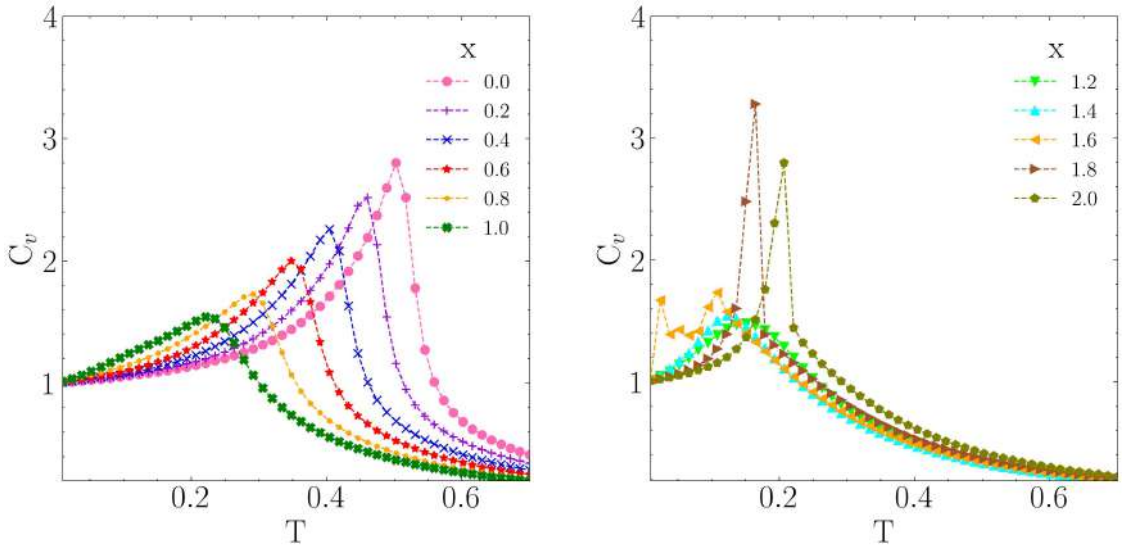

(a) **(b)**

Figure 3.6: Temperature dependence of specific heat C_v for (a) $0 \leq x \leq 1$ and (b) $1.2 \leq x \leq 2$ for the CQD model (correlated quenched disorder). System size is $L = 4$.

Despite substantial quenched disorder, the E order parameter reaches quasi-saturation at zero temperature up to $x \lesssim 0.6$ (see Fig. 3.7(a)). For a given tetrahedron, coupling parameters for $Er_2Ti_2O_7$ are the ones minimizing the energy of the Γ_5 states with E symmetry. It means that all the bonds in the system with different coupling parameters cost energy compared to the pristine $Er_2Ti_2O_7$. Since the number of such bonds increases approximately linearly with x (as long as x is not too big), so should the ground state energy of the entire system. This explains the regular spacing between the energy curves of Fig. 3.8 up to $x \sim 0.6 - 0.8$.

In addition, Fig. 3.8 underlines a symmetry of the energy curves at low temperatures between $x = 0.8$ and $x = 2$, centered around $x = 1.4$. This suggests that our CQD model might reach a maximum of frustration (both geometric and disorder induced) around $x = 1.4$, and encourages us to further explore this intermediate region via finite size scaling.

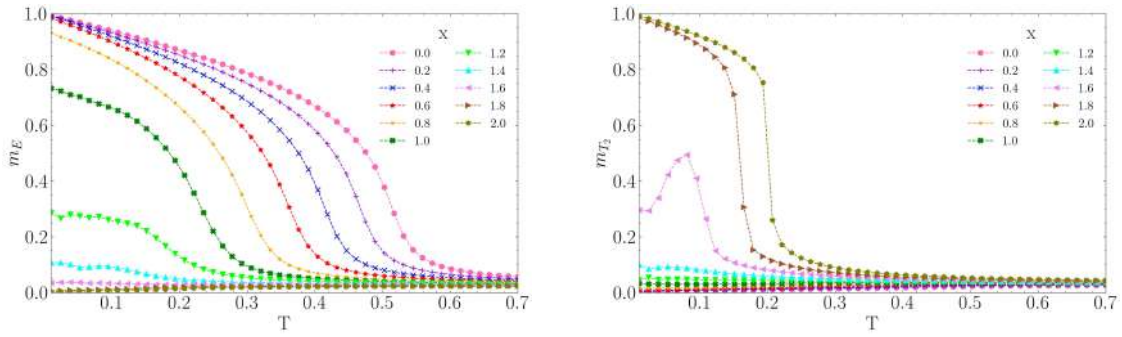

(a) **(b)**

Figure 3.7: Temperature dependence of (a) m_E and (b) m_{T_2} order parameters for the CQD model (correlated quenched disorder). The results are consistent with Γ_5 order with E symmetry for $x \leq 1$ and Palmer-Chalker order with T_2 symmetry for $x \geq 1.8$. Finite size scaling is necessary to clarify the situation for intermediate x values. System size is $L = 4$.

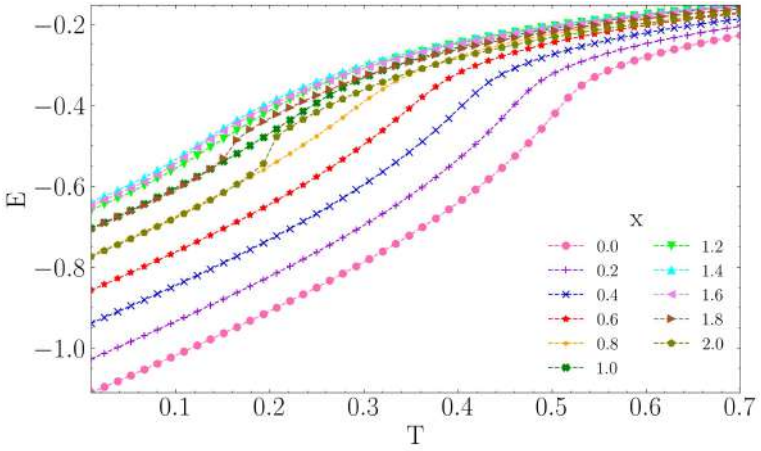

Figure 3.8: Temperature dependence of the energy for the CQD model (correlated quenched disorder). A symmetry in the energy is observed at low temperatures between x=0.8 and x=2, centered at x=1.4. System size is $L = 4$.

3.2.3 Model 1: Finite Size Scaling (FSS)

While quenched disorder might prevent long-range magnetic order, partial order might persist on finite length scale. This is why an order parameter might appear finite on small systems, but eventually vanishes in the thermodynamic limit (N $\to \infty$, V $\to \infty$ such that $\frac{N}{V}$ = constant). To determine what happens in our CQD model, we perform finite-size scaling (FSS) analysis for different dilution x and different system sizes ($L = 3, 4, 5, 6$). We extract the saturated value of m_E and m_{T_2} order parameters at low enough temperatures

and compare its evolution with the scaling function

$$f(L) = a * L^{-b} + c, \tag{3.4}$$

where a, b, and c are constants. We are particularly interested in the value of c since it gives the value of order parameters in the thermodynamic limit.

In Fig. 3.9 we show the m_E (a,c,e,g) and m_{T_2} (b,d,f,h) order parameters for $x = 0.4$, 1.0, 1.5 and 1.8. The scaling functions (equation 3.4) are plotted in the inset. FSS at $x = 0.4$ and 1.8 show that the respective E and T_2 orders are quasi-saturated, confirming that a "small" amount of non-magnetic dilution is not enough to drastically modify the physics of $Er_2Ti_2O_7$ and $Er_2Sn_2O_7$. However, the m_E order parameter noticeably drops at $x = 1$. This is easy to understand since roughly 1/4 of the bonds bear the coupling parameters of $Er_2Sn_2O_7$, thus favoring T_2 order. It is actually somewhat surprising to see the Γ_5 order with E symmetry persists for such large values of disorder. We shall come back to that point in section 3.3.

But it is at $x = 1.5$ that the physics qualitatively changes. Here, both order parameters vanish in the thermodynamic limit (within numerical noise). To make sure we did not miss the appearance of another form of long-range order, we confirmed the absence of any forms of dipolar and quadrupolar orders and the absence of Bragg peaks in the structure factor at zero and finite wavevectors $\mathbf{q}$ (see section 3.4). When plotting the evolution of these order parameters in the thermodynamic limit as a function of x in Fig. 3.10, we see that the absence of long-range order persists between $x = 1.2$ and 1.6. Finite-size scaling for other values of x are given in Appendix A.

FSS analysis has thus shown that the competition between $Er_2Ti_2O_7$ and $Er_2Sn_2O_7$ coupling parameters does not induce the co-existence of the two corresponding antiferromagnetic phases, but rather destroys any form of long-range order over a reasonable part of the phase diagram. We are now left with two possible scenarios for this intermediate regime: is it a spin liquid or a spin glass? Or in other words, which frustration is the strongest in this regime: geometric or quenched disorder?

3.2.4 Model 1: Spin Glass and Transition Temperature

Since the structure of the lattice is strongly disordered in this intermediate regime, the presence of a spin glass is a priori more likely. To prove that, we shall now consider the simulations of so-called replicas. For every realization of the lattice disorder, we run two thermally independent copies from Monte-Carlo simulations and compute the overlap field between these two replicas [98, 99, 100]

$$q_i = s_i^{(1)}.s_i^{(2)}. \tag{3.5}$$

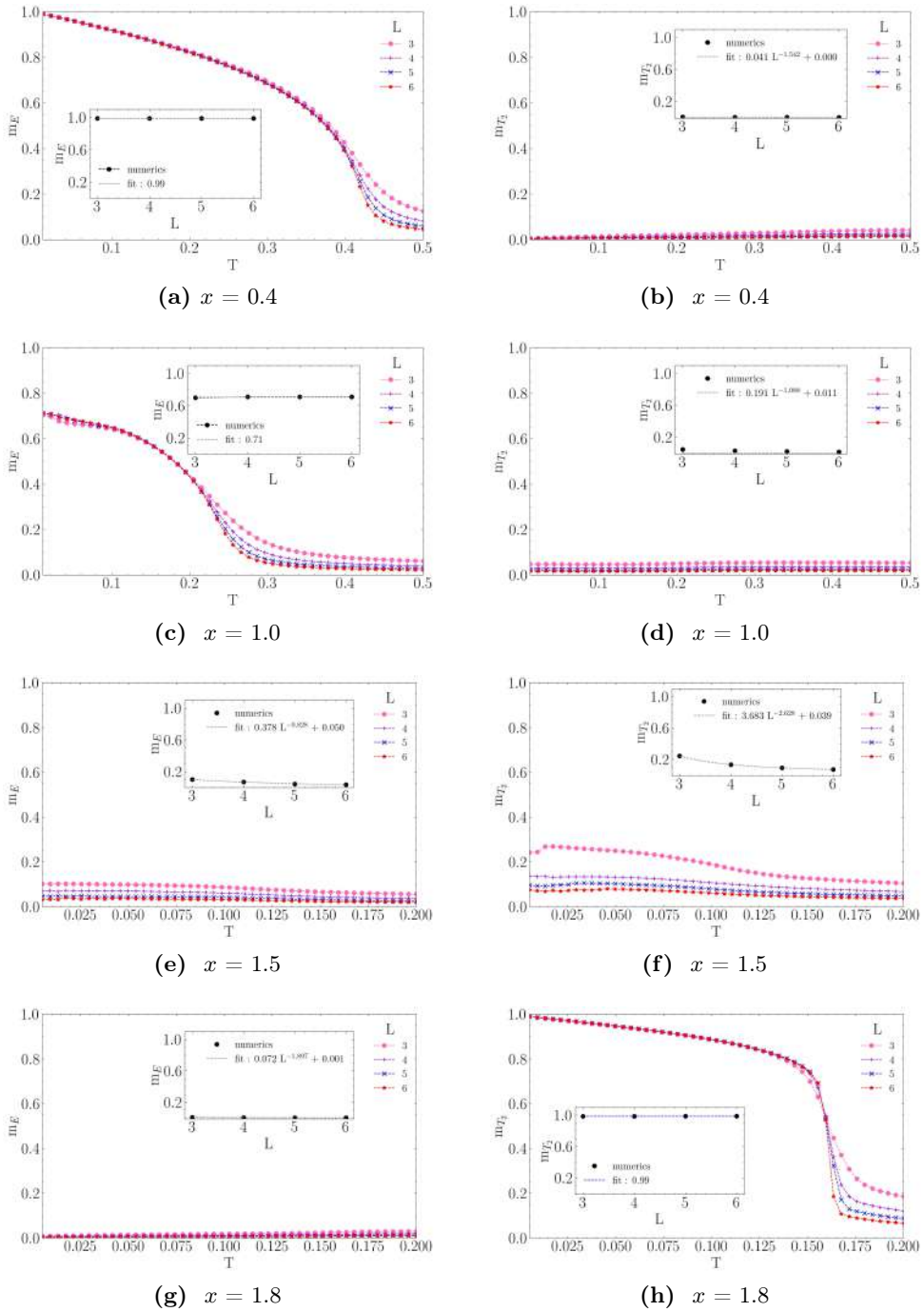

(a) $x = 0.4$ **(b)** $x = 0.4$

(c) $x = 1.0$ **(d)** $x = 1.0$

(e) $x = 1.5$ **(f)** $x = 1.5$

(g) $x = 1.8$ **(h)** $x = 1.8$

Figure 3.9: Temperature dependence of m_E (a,c,e,g) and m_{T_2} (b,d,f,h) order parameter of the CQD model for $x = \{0.4, 1, 1.5, 1.8\}$ and $L = \{3, 4, 5, 6, \}$. Inset: Finite-size scaling of the corresponding order parameter at very low temperature. The constant in the scaling function gives the value of the order parameter in the thermodynamic limit.

The total overlap is the lattice average

$$q = \frac{1}{N} \sum_i q_i, \tag{3.6}$$

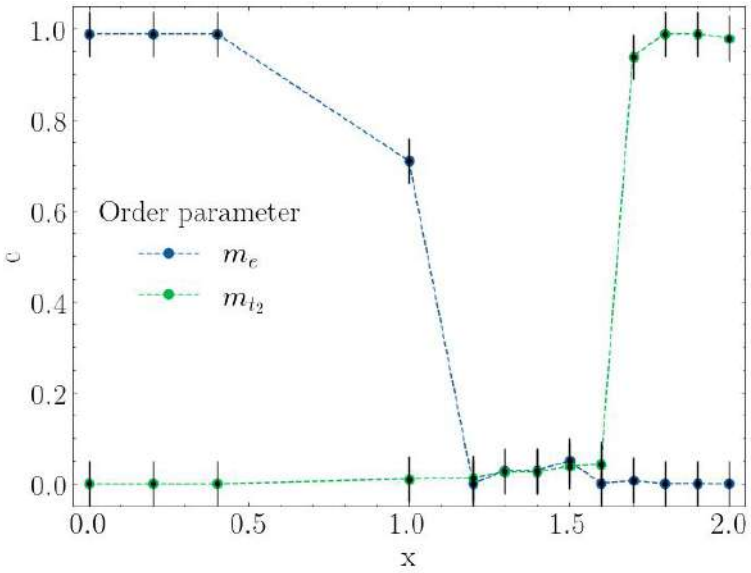

Figure 3.10: Value of the parameter c vs x obtained from the finite size scaling analysis (see Eq. 3.4), showing the evolution of the two order parameters, m_E and M_{T_2}, at very low temperature in the thermodynamic limit. There is a region without any long-range order between $x = 1.2$ and 1.6.

which gives the spin-glass susceptibility

$$X_q = V\overline{< q^2 >}, \tag{3.7}$$

with $V = 16L^3$ (number of spins). These quantities are able to measure the apparition of a spin glass phase, and also to provide a precise estimate of the transition temperature T_c. Indeed, the specific heat is not a good quantity anymore to measure T_c. Instead, we will prefer to use the fourth-order Binder cumulant [71]

$$U_b = \frac{3}{2} - \frac{1}{2}\frac{\overline{< q^4 >}}{\overline{< q^2 >}^2}. \tag{3.8}$$

As usual, we denote thermal averages by $\langle O \rangle$ and disorder averages by $\overline{O}$. The transition temperature is given by the crossing point of the Binder cumulants for multiple system sizes.

Our simulations confirm the establishment of a spin-glass phase in this intermediate regime. In Fig. 3.11, we plot the Binder cumulants for different system sizes which allows us to determine the transition temperature, even in this region without long-range order. But it is not yet enough to describe the full phase diagram of our CQD model, because we do not know if there is order by disorder among the Γ_5 states.

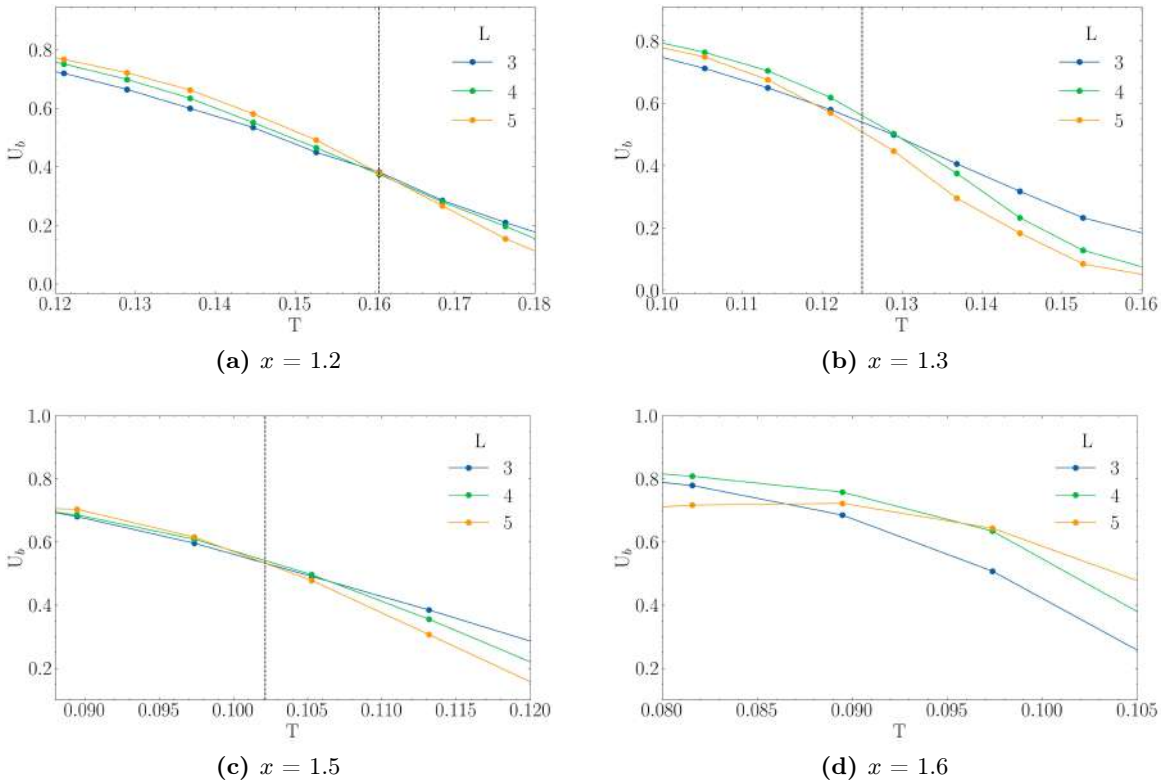

(a) $x = 1.2$ **(b)** $x = 1.3$

(c) $x = 1.5$ **(d)** $x = 1.6$

Figure 3.11: Binder cumulant U_b for (a)$x = \{1.2, 1.3, 1.5, 1.6\}$, as defined in Eq. (3.8). The crossing of the curves gives the value of the transition temperature and the associated error bars.

3.2.5 Model 1: Order by Disorder in the Γ_5 states

As explained in section 1.3.1, $Er_2Ti_2O_7$ is a famous instance of the order-by-disorder (ObD) mechanism. Its ground state has a U(1) degeneracy, lifted in favour of the Ψ_2 states in the pristine sample, while impurities are known to favour Ψ_3 states [49, 50, 51]. To distinguish between Ψ_2 and Ψ_3 orders is not straightforward though. The order parameter $\mathbf{m}_E = (m_{E_x}, m_{E_y})$ (see Table 1.1) only measures the presence of the U(1) manifold with E symmetry, and does not distinguish between states within this manifold.

This is why we measure the probability distribution $P(m_{E_x}, m_{E_y})$ [51, 101, 102, 3], as plotted in Fig 3.12 for different x values, and first focusing on low-temperature properties at $T = 0.05$ K. We naturally find Ψ_2 order for $Er_2Ti_2O_7$ at $x = 0$, with its six-fold degeneracy visible by the six arcs of higher intensity around the circle of (quasi-)saturated E order where $|\mathbf{m}_E|^2 = m_{E_x}^2 + m_{E_y}^2 = 1$. But as we increase the dilution to $x = 0.3$, these six arcs shift by a $\pi/6$ angle to the Ψ_3 states. This shift to Ψ_3 is consistent with previous works with different kind of quenched disorder [49, 50, 51], which strongly supports the idea that any form of quenched disorder reverses the ObD selection in $Er_2Ti_2O_7$.

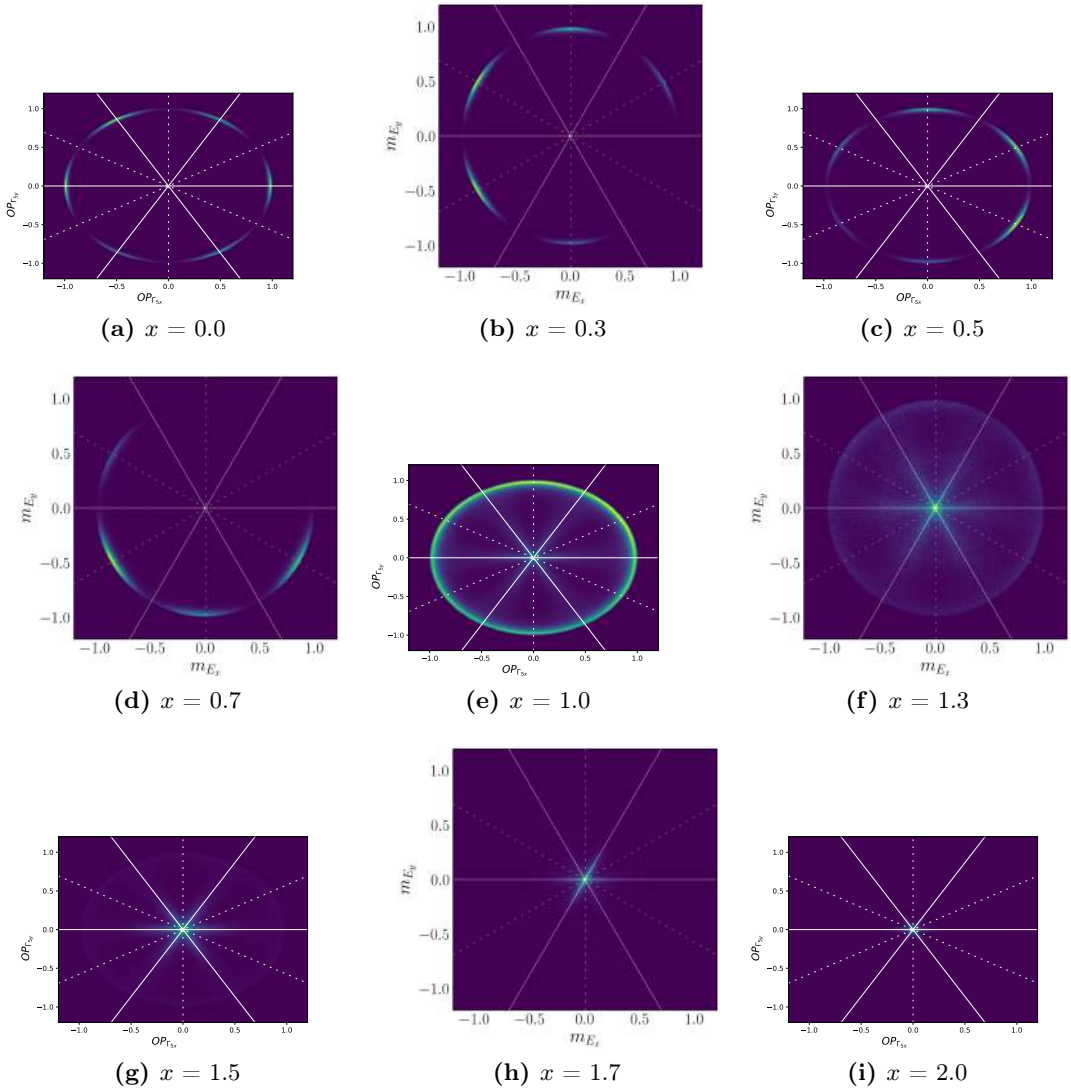

(a) $x = 0.0$ **(b)** $x = 0.3$ **(c)** $x = 0.5$

(d) $x = 0.7$ **(e)** $x = 1.0$ **(f)** $x = 1.3$

(g) $x = 1.5$ **(h)** $x = 1.7$ **(i)** $x = 2.0$

Figure 3.12: Probability distribution $P(m_{E_x}, m_{E_y})$ of the $\mathbf{m}_E$ order parameter at $T < T_c$ ($T = 0.05$ K) for different x values and system size $L = 10$. A uniform E order would give a circle $|\mathbf{m}_e|^2 = cst = m_{E_x}^2 + m_{E_y}^2$, while Ψ_2 and Ψ_3 orders are given by the full and dashed radial lines respectively, as defined in section 1.2.3.(II.a,b).

While Ψ_3 order persists for $x = 0.5$ and 0.7, we recover the uniform U(1) manifold at $x = 1$. This is fairly uncommon as ObD is usually expected to lift the U(1) ground-state degeneracy of frustrated systems that are not protected by Hamiltonian symmetry. However, here, thermal fluctuations are apparently not strong enough to compete with such a large quenched disorder. We can maybe rationalize this phenomenon by the fact that ObD is related to soft modes; soft modes that may require a certain length scale to take place. In some systems, ObD is known to appear only for big enough systems [3]. The presence of $\sim 1/4$ of $Er_2Sn_2O_7$ bonds that do not favour the U(1) manifold might prevent these soft modes to propagate

on length scales that are sufficient for thermal fluctuations (i.e. entropy) to select either Ψ_2 or Ψ_3 states. Interestingly, the radius of the circular distribution at $x = 1$ is almost $|\mathbf{m}_E| = 1$, which is noticeably larger than the value of ~ 0.7 found at low temperature in Fig. 3.9(c). Taken together, these data mean that almost all tetrahedra at $x = 1$ are in a spin configuration very close to one of the Γ_5 states with E symmetry; but it is not the same spin configuration across the lattice, which is why the overall spatial average gives $|\mathbf{m}_E| \sim 0.7$.

Finally, the circular intensity disappears for $x \geq 1.3$ since the $\mathbf{m}_E$ order parameter simply fluctuates around zero. There is, however, a diffuse halo inside the circle which means that a measurable fraction of tetrahedra still bear Γ_5 order over short-length scale. It is worth noticing though that the fluctuations around $m_E = 0$ are along the Ψ_2 radial lines. Keeping in mind the shape of the ground state manifold at the boundary between the E and T_2 phases in Fig. 1.11, we understand that in this parameter space, soft modes away from the Palmer-Chalker states favored by the $Er_2Sn_2O_7$ bonds tend precisely towards Ψ_2 states.

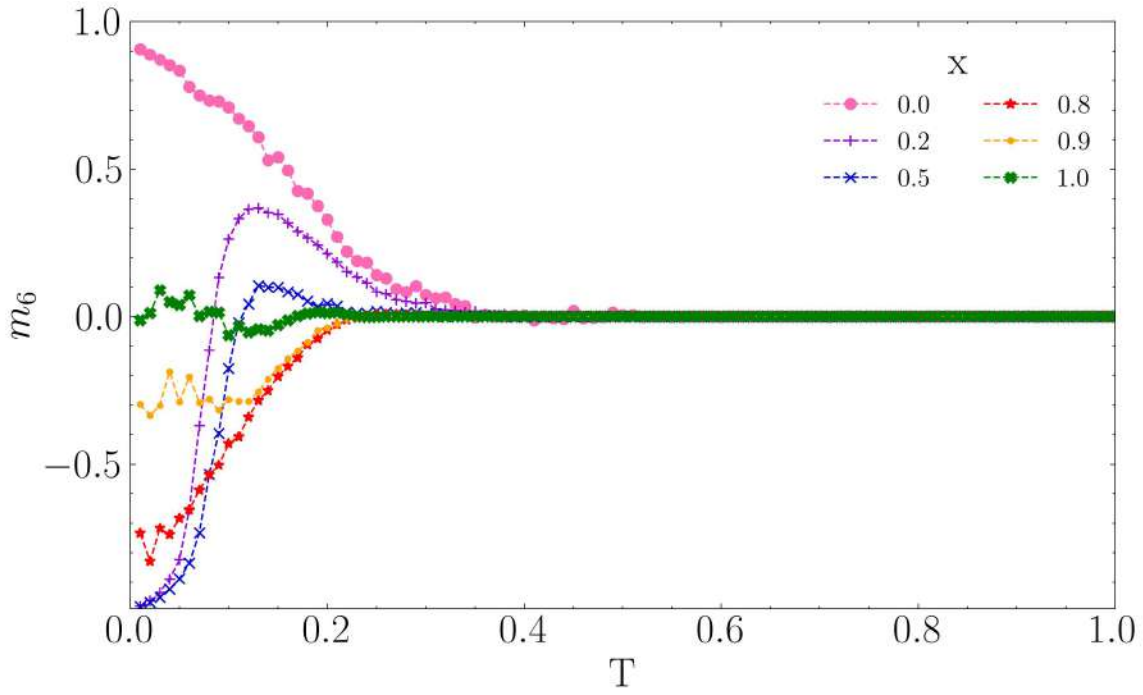

Figure 3.13: Clock-like order parameter m_6 as a function of T for L = 10 and several values of x where m_6 being positive (negative) for the Ψ_2/Ψ_3 states. We clearly see a change in temperature for a given x, until Ψ_2 disappears.

The probability distribution $P(m_{E_x}, m_{E_y})$ was a good way to get a snapshot of the Γ_5 physics at a given temperature and dilution x. But in order to finalise the phase diagram of the CQD model, we shall use the pseudo-order parameter[101]

$$m_6 = m_E \cos(6\Phi) \quad \text{where} \quad \Phi = \tan^{-1}(m_{E_y}/m_{E_x}). \tag{3.9}$$

Positive (resp. negative) values of m_6 indicate Ψ_2 (resp. Ψ_3) orders. Fig. 3.13 shows that

even if the low temperatures are always dominated by Ψ_3, Ψ_2 persists at finite temperature for small dilution x. m_6 cannot differentiate between the two states for $x \geq 1$, as expected from our analysis of Fig. 3.12.

3.2.6 Model 1: Spin-glass dynamics

Monte Carlo simulations have brought to light a spin-glass phase for $1.2 \leq x \leq 1.6$. However, the effect of glassiness is most well-known in the dynamics of the system. This is why we shall conclude our analysis of the CQD model using Landau-Lifshitz dynamics (see section 2.9) and computing the autocorrelation function $A(t)$ in Fig. 3.14(a).

$$A(t) = \sum_{a,b,c,d} \frac{\frac{4}{N}\sum_i < \overline{S_i(0).S_i(t)} > -\frac{4}{N}\sum_i < \overline{S_i(t)} > .\frac{4}{N}\sum_i < \overline{S_i(0)} >}{1 - (\frac{4}{N}\sum_i < \overline{S_i(0)} >)^2} \tag{3.10}$$

where $\langle O \rangle$ and $\overline{O}$ are respectively the thermal and disorder average, and (a, b, c, d) are the 4 sublattices of the pyrochlore lattice. Spin relaxation is very fast for the pristine samples ($x = 0$ and $x = 2$), as well as for $x = 0.5$. However, $A(t)$ reaches a plateau at long time for $x = 1$ and 1.5. Indeed spin glasses usually support a fast and a slow (glassy) spin dynamics [66]. The fast one is characteristic of the standard relaxation of spins at equilibrium. But once this fast relaxation has taken place, we are left with the frozen magnetic degrees of freedom that form the spin glass phase. the value of $A(t)$ on this plateau is known to be an approximate estimate of the Edwards-Anderson parameter q_{EA} for spin-glasses (see Eq. 1.20)[66].

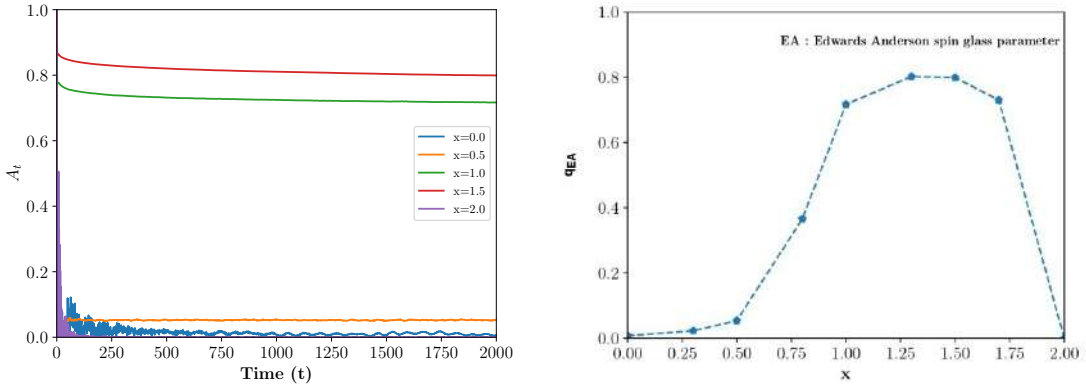

(a) **(b)**

Figure 3.14: (a) Autocorrelation function $A(t)$ of the CQD model at $T = 0.05$ K, as defined in Eq. 3.10), for several dilution x values. The decorrelation is fast for $x = 0, 0.5, 2$ while it reaches a plateau for $x = 1$ and 1.5. (b) q_{EA} vs x which is analogous to the Edwards-Anderson spin glass parameter.

To make this observation quantitative, we extract the value of $A(t)$ at long time (in practice, at $t_{long} = 2000$) and plot it as a function of x in Fig. 3.14(b). Of course, one needs to be

cautious when comparing results from Monte-Carlo simulations in the canonical ensemble and Landau-Lifshitz dynamics in the microcanonical ensemble. But with that caveat in mind, the results of Fig. 3.14(b) are remarkably consistent with the values of the antiferromagnetic order parameters in Fig. 3.10 at the same temperature $T = 0.05$ K. The spin-glass order parameter q_{EA} starts rising at $x \sim 0.5 - 0.6$, precisely when the antiferromagnetic E order becomes unsaturated (i.e. m_E becomes noticeably smaller than 1). Then it reaches a maximum around $x \sim 1.4$ and drops back to 0 for $x = 2$. The region of glassiness in the dynamics appears to be broader than in Monte Carlo simulations, but this is simply because some regions of the phase diagram have a noticeable co-existence of antiferromagnetic order (as measured by Monte Carlo simulations) and spin glass (as measured by spin dynamics).

3.2.7 Model 1: Phase diagram of the CQD model

After a detailed analysis in the previous sections, we report the phase diagram of the CQD model for $Er_2Ti_{2-x}Sn_xO_7$ in Fig 3.15. Here, the x-axis is the chemical dilution x and the y-axis is the critical temperature.

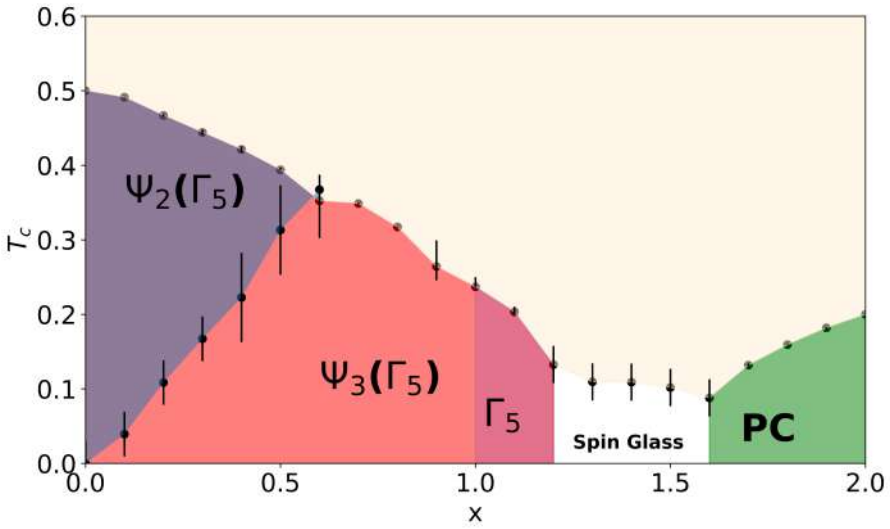

Figure 3.15: Phase diagram of the CQD model for $Er_2Ti_{2-x}Sn_xO_7$ obtained from classical Monte-Carlo simulations with Γ_5 (purple, pink and red), Palmer-Chalker (green) and spin-glass (white) phases. The Γ_5 phase is split into Ψ_2 and Ψ_3 orders because of order by disorder. In the region with noticeable disorder $x \in [1.0; 1.2]$, the full U(1) manifold of the Γ_5 phase is recovered, albeit with a fintie fraction fraction of frozen magnetic degrees of freedom.

One of the interesting outcomes of our CQD model is the emergence of spin glass behavior in the intermediate region between the two competing antiferromagnetic regions, as confirmed from Monte-Carlo simulations at equilibrium and Landau-Lifschitz out-of-equilibrium dynamics. Before further comparing this phase diagram to experiments, let us conclude our analysis with the third model with the uncorrelated quenched disorder (UQD).

3.2.8 Model 3: Uncorrelated quenched disorder (UQD)

As explained in section 3.1.3, model 3 is not unique. It depends on the value of α_0 since the bond perturbation Δ_i is a random variable distributed uniformly in the range $[-\alpha_0 J_{i,x}, \alpha_0 J_{i,x}]$. We performed simulations for three values of α_0: 0.1, 0.2, 0.3.

For $\alpha_0 = 0.3$, we recover a similar phase diagram as shown in Figure 3.15 for the CQD model. In particular, there is a spin-glass phase in the intermediate region. But since we can now tune the strength of quenched disorder, α_0, we shall focus our efforts on $\alpha_0 = 0.1$ and 0.2 and see how they deviate from the previous CQD model.

(i) $\alpha_0 = 0.2$

Fig. 3.16 shows that E order persists up to $x < 1.3$, giving rise to T_2 order for $x > 1.4$. This boundary is consistent with the one at $x_c = 1.323$ for the disorder-free NQD model. However, data at $x = 1.3$ and 1.4 show noticeable finite size effects; it is not clear if the E and T_2 orders persist in the thermodynamic limit in this region. that being said, if a spin-glass phase persists for $\alpha_0 = 0.2$, it will be limited to a rather narrow window of dilution for $x \sim 1.3 - 1.4$, smaller than for $\alpha_0 = 0.3$.

(ii) $\alpha_0 = 0.1$

As for α_0, Fig. 3.17 shows that E order persists up to $x \leq .3$, giving rise to T_2 order for $x \geq 1.4$. The m_{T_2} order parameter remains a bit noisy at low temperature for $x = 1.4$. Nevertheless, we now have clear antiferromagnetic order (either E or T_2) for all values of dilution x. It means that by using the disorder strength α_0, we could develop a microscopic model with quenched disorder but without any intermediate spin-glass phase. The resulting phase diagram for $\alpha_0 = 0.1$ is shown in Fig. 3.18. We did not measure the order-by-disorder competition between Ψ_2 and Ψ_3 here. But based on Ref. [49], since we have the same finite amount of bond disorder ($\alpha_0 = 0.1$) for all values of $x > 0$, we expect Ψ_3 order to dominate the Γ_5 region, except for the pristine sample at $x = 0$.

3.3 To benchmark simulations with experiments

Let us compare in Fig. 3.19 the phase diagrams of our three models (CQD, NQD and UQD) with the experimental one from Ref. [4]. The long-range ordered states are illustrated in Fig. 3.20 for convenience. First of all, we should point out that the transition temperature between simulations and experiments are off by a factor of approximately 2. This is a known artefact of using coupling parameters obtained by a quantum mean-field calculations in classical Monte Carlo simulations [3]. Our present theory is not claiming to reach this degree of precision. Our goal is rather to find a minimal model able to reproduce experiments semi-quantitatively, and especially how the physics of $Er_2Ti_{2-x}Sn_xO_7$ varies with dilution x.

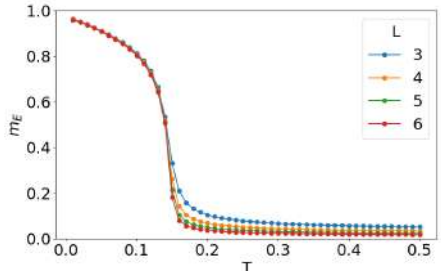

(a) $x = 1.2$

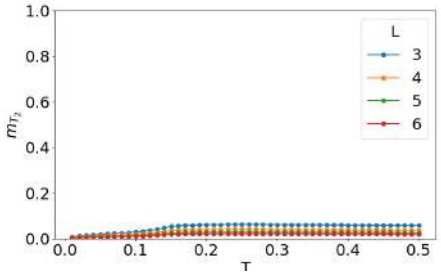

(b) $x = 1.2$

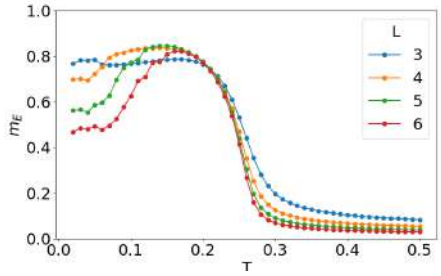

(c) $x = 1.3$

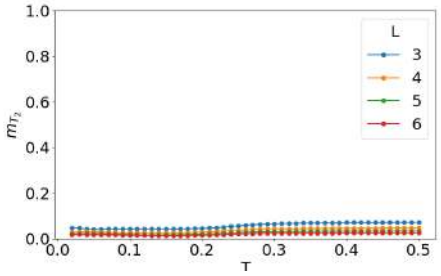

(d) $x = 1.3$

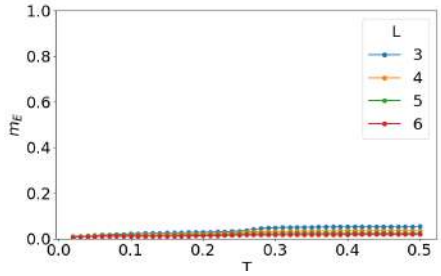

(e) $x = 1.4$

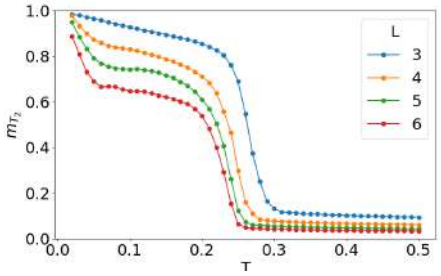

(f) $x = 1.4$

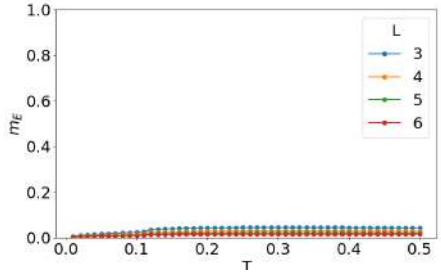

(g) $x = 1.5$

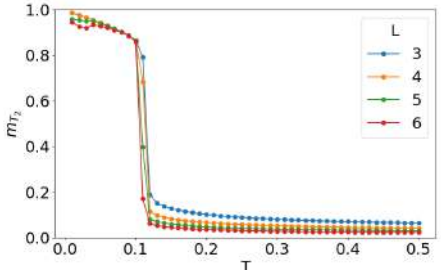

(h) $x = 1.5$

Figure 3.16: Temperature dependence of (a,c,e,g) m_E and (b,d,f,h) m_{T_2} order parameters for the UQD model (uncorrelated quenched disorder) with $\alpha_0 = 0.2$, for $x = \{1.2, 1.3, 1.4, 1.5\}$ for system size $L = \{3, 4, 5, 6\}$.

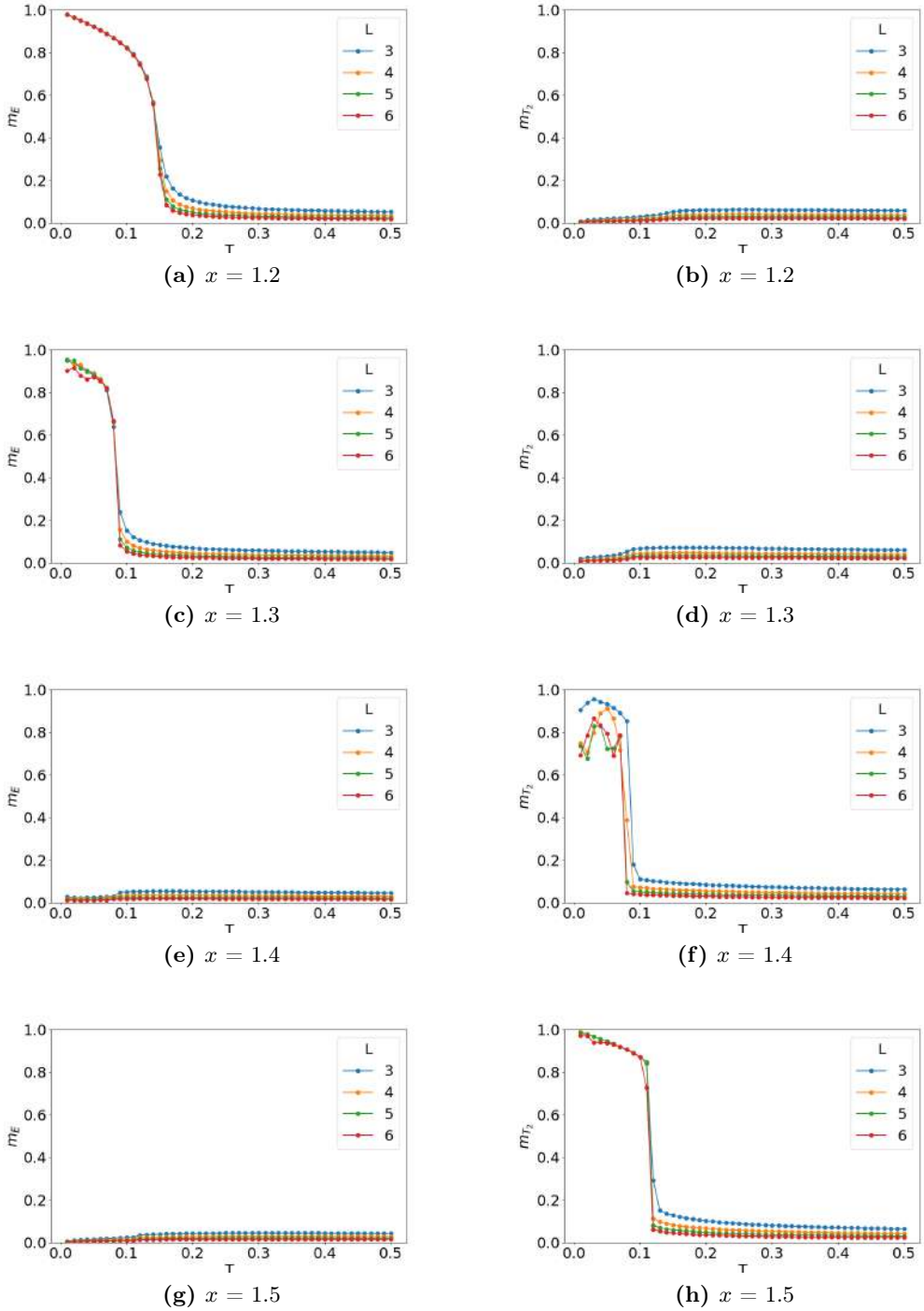

(a) $x = 1.2$ **(b)** $x = 1.2$

(c) $x = 1.3$ **(d)** $x = 1.3$

(e) $x = 1.4$ **(f)** $x = 1.4$

(g) $x = 1.5$ **(h)** $x = 1.5$

Figure 3.17: Temperature dependence of (a,c,e,g) m_E and (b,d,f,h) m_{T_2} order parameters for the UQD model (uncorrelated quenched disorder) with $\alpha_0 = 0.1$, for $x = \{1.2, 1.3, 1.4, 1.5\}$ for system size $L = \{3, 4, 5, 6\}$.

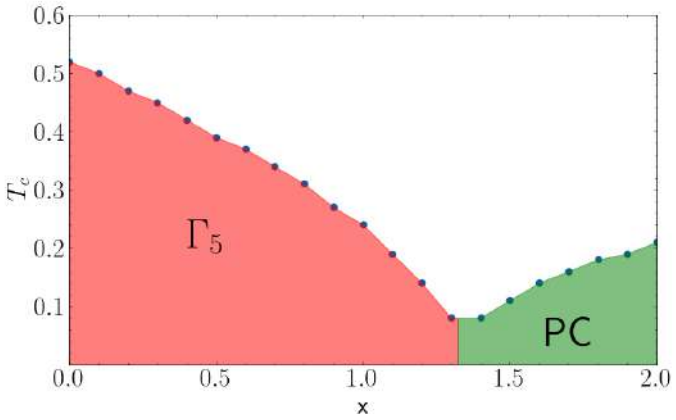

Figure 3.18: Phase diagram of the UQD model for $\alpha_0 = 0.1$

In that sense, our first main observations are the asymmetry of all four phase diagrams (in experiments and simulations) with a large Γ_5 region on the left; and a transition temperature that first decreases with x before increasing in the T_2 region. This can be explained by the proximity of $Er_2Sn_2O_7$ to the boundary (see Fig. 3.2). Indeed both CQD and UQD models with quenched disorder follow the same asymmetry as the NQD model without quenched disorder. Please note that the precise value of the boundary $x_c = 1.323$ obtained in Eq. (3.3) could easily be shifted to ~ 1.7, as observed in experiments, by slightly modifying the coupling parameters of $Er_2Sn_2O_7$, within the error bars measured in Ref. [10]. Indeed the proximity of $Er_2Sn_2O_7$ to the E/T_2 boundary means that x_c is particularly sensitive to its parametrisation. In any case, it means that the maximum of frustration (geometric + quenched disorder) is not observed when the non-magnetic dilution is maximum (i.e. 50% of Ti and 50% of Sn), but is instead determined by the underlying disorder-free phase diagram of Fig. 3.2 for the pristine systems. This is an important result as it supports the idea of this thesis; non-magnetic dilution can be used to explore regions of the phase diagram between known pristine compounds that are inaccessible otherwise.

Another result is that experiments do not seem to find a spin glass intervening between the Γ_5 and Palmer-Chalker states [4]. It would probably be good for future experiments to confirm this absence of out-of-equilibrium effects. But in that regard, the UQD model of Fig. 3.19(c) would be more consistent than the one with correlated quenched disorder (CQD) in Fig. 3.19(a). It suggests that even if the CQD model is qualitatively correct, the approximation to consider only the two neighboring non-magnetic ions for each bond might be too simplistic. Further non-magnetic neighbors might play a role, in which case the crystal field environment around each bond will sustain a variety of minute deformations. Since anisotropic superexchange between rare-earth ions are sensitive to such minute angle deformations, the Er-Er bonds would then take a broader range of values. The similari-

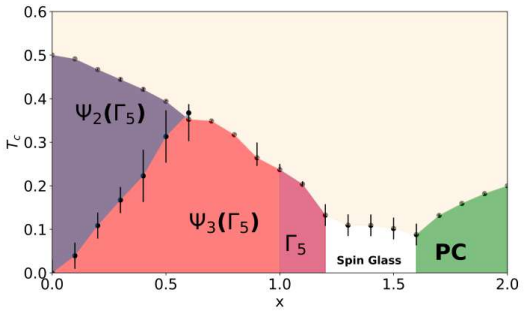

(a) Model 1 : Correlated Quenched Disorder

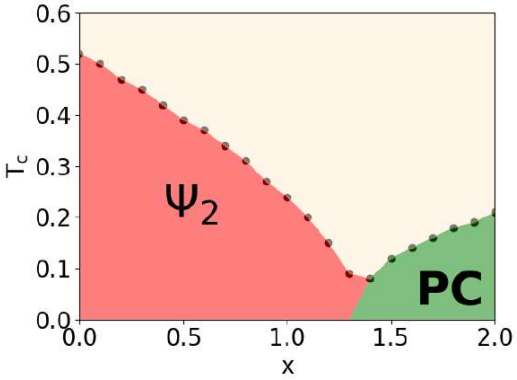

(b) Model 2 : No Quenched Disorder

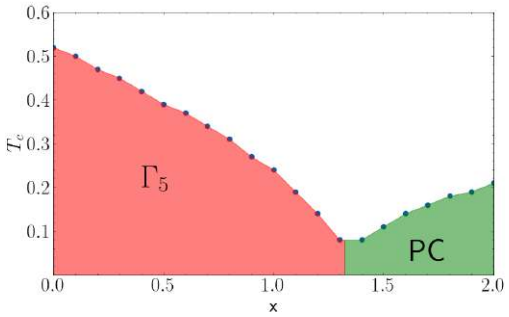

(c) Model 3 : Uncorrelated Quenched Disorder ($\alpha_0 = 0.1$)

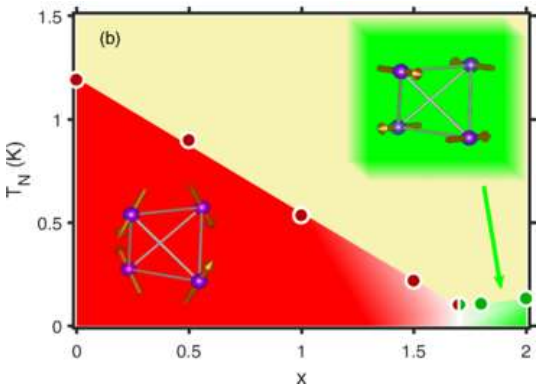

(d) Experimental phase diagram[4]

Figure 3.19: Phase diagrams for the three models studied in this thesis (a,b,c), compared to experiments on $Er_2Ti_{2-x}Sn_xO_7$ from Ref. [4] (d). The x-axis is always the dilution parameter x (or its equivalent as defined in section 3.1). All the ordered phases are antiferromagnetic, either with E (purple or red) or T_2 (green) symmetry. The white region in panel (a) is a spin glass.

ties between our simulations and experiments, and the apparent absence of spin glass in experiments, strongly suggests that these deformations should remain small though. In that case, the apparently simpler UQD model appears to be more accurate to reproduce the phase diagram of $Er_2Ti_{2-x}Sn_xO_7$. And the absence of spin glass in simulations for $\alpha_0 = 0.1$ confirms that the exchange perturbations is expected to remain relatively small.

In conclusion, our simulations can semi-quantitatively reproduce the experimental phase diagram $Er_2Ti_{2-x}Sn_xO_7$. They explain its asymmetry and strongly support the idea that a small, random, quenched disorder along a line in parameter space connecting the two pristine compounds $Er_2Ti_2O_7$ and $Er_2Sn_2O_7$, is a good way to understand the influence of non-magnetic dilution in rare-earth pyrochlore oxides. Now that our theory has been benchmarked against experiments, let us explore how easy it is to tune the properties of

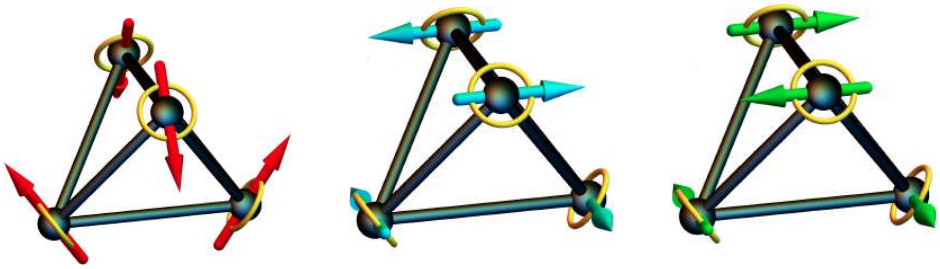

(a) (b) (c)

Figure 3.20: Spin configurations of the antiferromagnetic ordered phases found in the phase diagrams of Fig. 3.19: (a) non-coplanar Ψ_2, (b) coplanar Ψ_3 and (c) coplanar Palmer–Chalker (Ψ_4) states. Ψ_2 and Ψ_3 belong to the U(1) manifold of the Γ_5 states.

frustrated magnets via dilution.

3.4 Bridging the gap between rare-earth pyrochlores

The successful comparison between the different phase diagrams of Fig. 3.19 supports the idea that non-magnetic dilution (either in experiments or in the UQD model) offers a bridge between compounds in parameter space (the NQD model), at least for the low-temperature ordered phases (Γ_5 or Palmer-Chalker) and the evolution of the transition temperature T_c as a function of x. But what about intermediate temperatures above T_c ? Spin correlations above T_c are signature of both the onset of long-range order, and the proximity of other nearby phases [103, 3]. In that sense they offer a rich snapshot of the magnetic properties of a system, more subtle than simply the nature of magnetic order; here, order can be seen as a low-temperature selection within the phase space explored at intermediate temperature.

But since there is no broken symmetry by definition above T_c, there is no relevant order parameter to compute. The structure factor $S(\mathbf{q})$ is then the observable of choice to characterize magnetic correlations. Fortunately, the structure factors of $Er_2Ti_2O_7$ ($x = 0$) and $Er_2Sn_2O_7$ ($x = 2$) are noticeably different (see Fig. 3.21). The latter form a diamond pattern with maxima at (0,0,2) characteristic of the Palmer-Chalker onset, while the former is essentially made of broad intensity peaks indicating short-range antiferromagnetic correlations, with maxima at (2,2,0). This contrast provides a qualitative way to compare the evolution of $S(\mathbf{q})$ as a function of x between the three models: CQD, NQD and UQD. We will consider three different dilution values $x = \{0.5, 1.0, 1.5\}$. For The sake of completeness, we will plot three different temperatures at $T < T_c, T \approx T_c$ and $T > T_c$. Since we already know that low-temperature data will be the same (except in the spin-glass regime), we will focus our discussion to $T > T_c$.

Our main result is that the three models have essentially the same structure-factor evolution

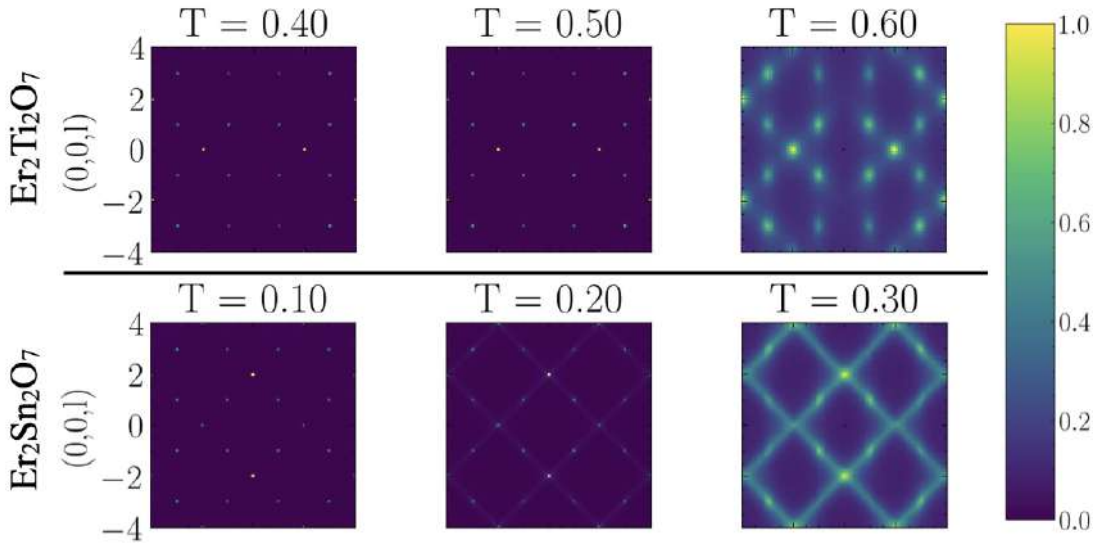

Figure 3.21: Structure factor $S(\mathbf{q})$ obtained from classical Monte Carlo simulation for parameters of $Er_2Ti_2O_7$ (top) and $Er_2Sn_2O_7$ (bottom) at three different temperatures : $T < T_c, T \approx T_c$ and $T > T_c$.

as a function of x (see Figs. 3.22, 3.23 and 3.24). At $x = 0.5$, there is some diffuse scattering appearing between the broad peaks characteristic of $Er_2Ti_2O_7$, but otherwise $S(\mathbf{q})$ remains quite similar to the one at $x = 0$. This is consistent with the idea developed in the previous sections that, independently of the type of quenched disorder considered here – correlated or not – a dilution of $x = 0.5$ is not enough to substantially change the properties of $Er_2Ti_2O_7$.

Comparing $x = 1$ to $x = 1.5$, we see the emergence of butterfly patterns superimposed with either the broad peaks of $Er_2Ti_2O_7$ for $x = 1$ in Fig. 3.23, or the (deformed) diamond shapes of $Er_2Sn_2O_7$ for $x = 1.5$ in Fig. 3.24. Hence, the region $1 \leq x \leq 1.5$ is where the system changes from $Er_2Ti_2O_7$ to $Er_2Sn_2O_7$ physics, in agreement with the ground-state boundary at $x_c = 1.323$. The interesting point is that we can interpret these butterfly patterns as a consequence of the proximity to this boundary. The boundary between E and T_2 phases is indeed adiabatically connected to the Heisenberg antiferromagnet (see Fig. 1.7), a classical spin liquid of extensive entropy, and with characteristic butterfly patterns in the structure factor [56]. It is the extensive entropy of this spin liquid that enables its properties (here its magnetic spin-spin correlations) to spread over vast regions of the phase diagram at finite temperature. But while it is understandable to see features of the spin liquid in the pristine NQD model *without* quenched disorder, it is remarkable to see these features persist in the two models *with* quenched disorder.

To conclude, we have shown in this section that the structure factor of our three models, with and without quenched disorder, evolves the same way as a function of x above T_c. In particular, non-trivial features such as the butterfly patterns, due to the proximity of

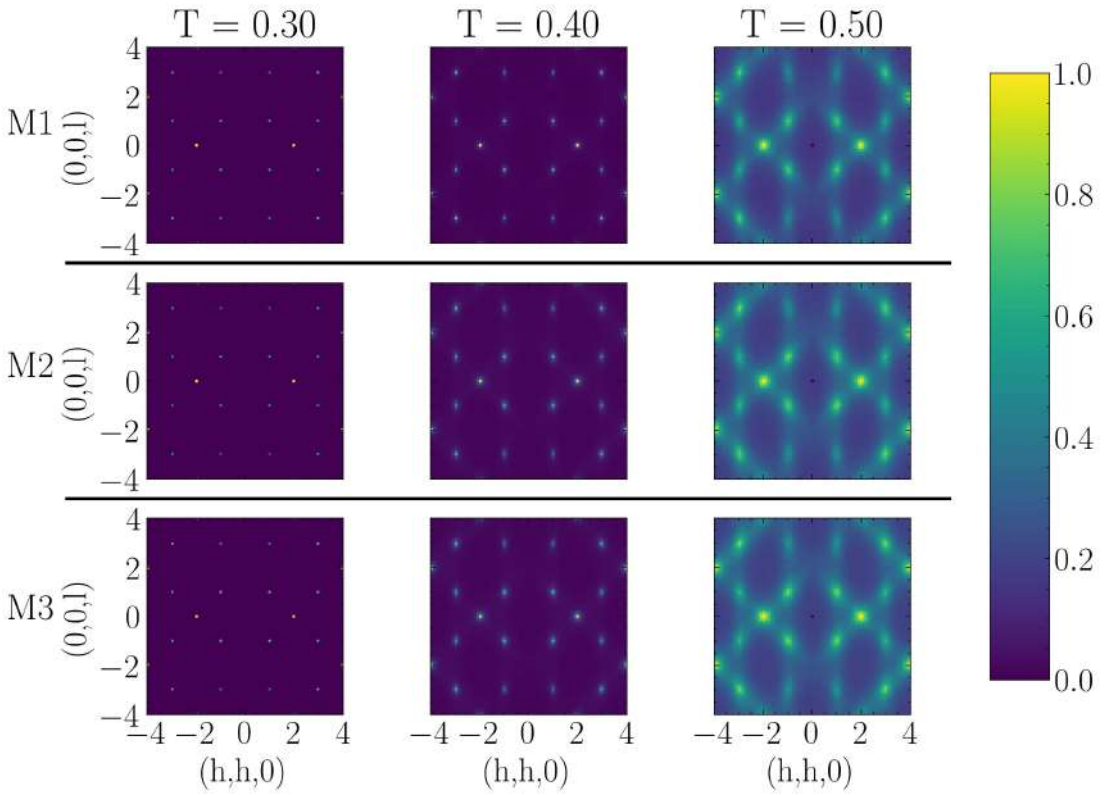

Figure 3.22: Structure factor $S(\mathbf{q})$ obtained from classical Monte Carlo simulation for $x = 0.5$ at three different temperatures : $T < T_c, T \approx T_c$ and $T > T_c$. The first, second and third row corresponds to the CQD, NQD and UQD models respectively. All models order into Γ_5. For each panel, the color scale goes from zero to the maximum of intensity.

the Heisenberg antiferromagnet, appear in all three models. Hence, with respect to (i) the low-temperature long-range order for $T < T_c$, (ii) the non-monotonic evolution of the transition temperature T_c and (iii) the spin-spin correlations at intermediate temperature for $T > T_c$, we have been able to use non-magnetic dilution x as a tuning parameter between $Er_2Ti_2O_7$ and $Er_2Sn_2O_7$.

3.5 In presence of a magnetic field h

In this final section about $Er_2Ti_{2-x}Sn_xO_7$, let us briefly consider the influence of magnetic field $h \leq 0.8$ T along the [001] direction. $Er_2Sn_2O_7$ is known to support reentrance behavior in a field, but not $Er_2Ti_2O_7$ [97][1]. Here we confirm this behavior for intermediate values of dilution x in the $h - T$ phase diagram of Fig. 3.25. At low field $h < 0.8$ T, the transition temperature decreases with magnetic field h for $x < 1$, while it increases for $x \geq 1.5$. Since

[1]Reentrance is the property of a system to return from an ordered phase to a previously encountered less-ordered phase as a controlling parameter (here the magnetic field h) is continuously varied.

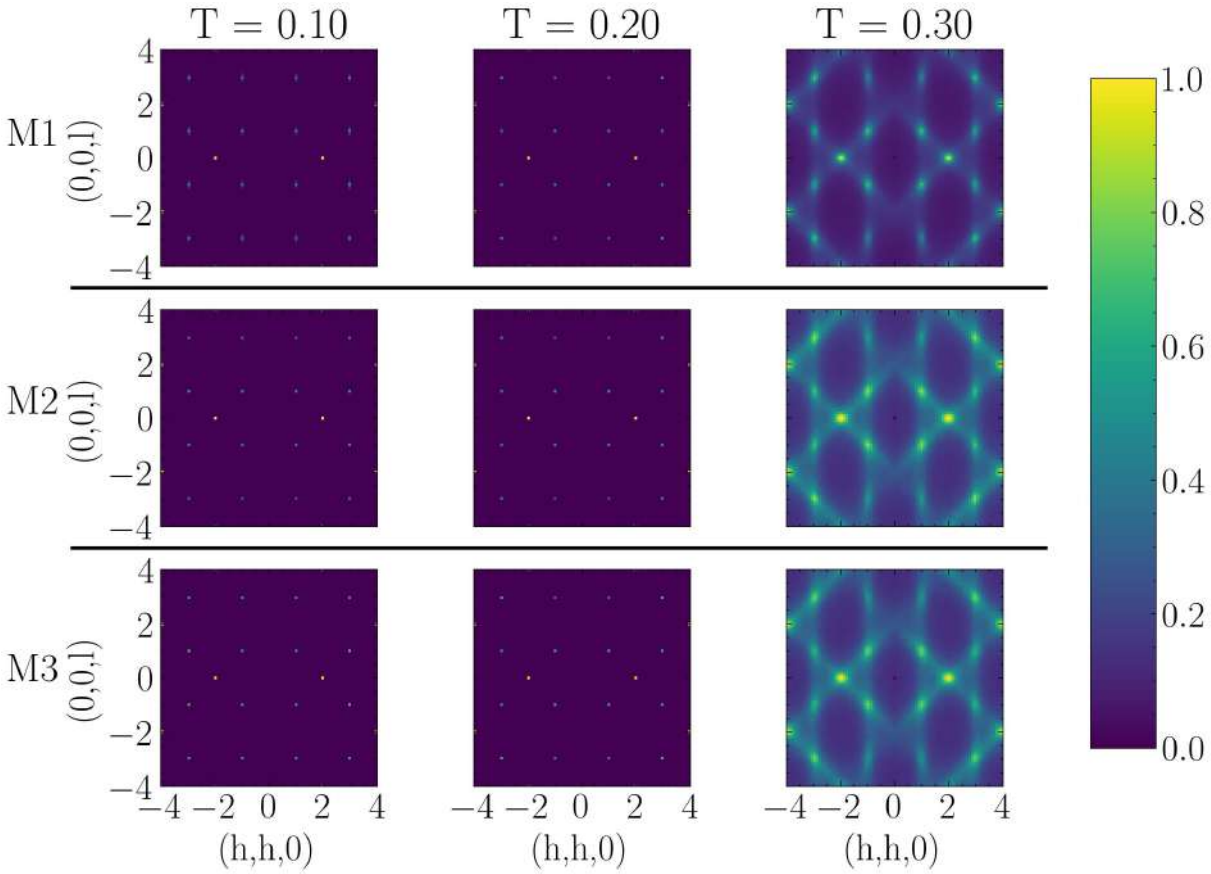

Figure 3.23: Structure factor $S(\mathbf{q})$ obtained from classical Monte Carlo simulation for $x = 1$ at three different temperatures : $T < T_c, T \approx T_c$ and $T > T_c$. The first, second and third row corresponds to the CQD, NQD and UQD models respectively. All models order into Γ_5. For each panel, the color scale goes from zero to the maximum of intensity.

we have Palmer-Chalker order at low temperature for $x \geq 1.5$, this antiferromagnetic state must vanish at high field. It means there must be a magnetic field h_0 above which the transition temperature starts to decrease, until it eventually reaches $T_c = 0$. Our CQD model thus reproduces the apparition of reentrance at finite dilution in $Er_2Ti_{2-x}Sn_xO_7$.

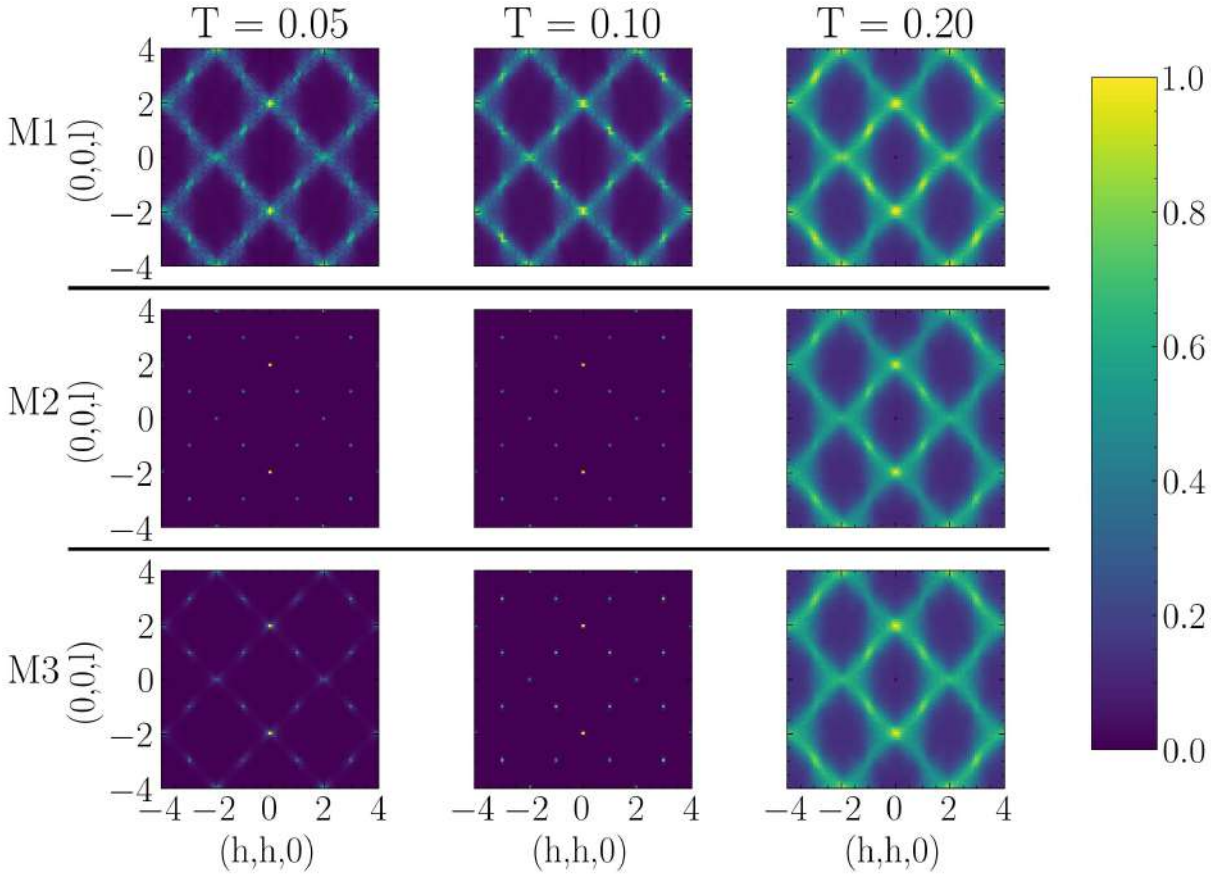

Figure 3.24: Structure factor $S(\mathbf{q})$ obtained from classical Monte Carlo simulation for $x = 1.5$ at three different temperatures: $T < T_c, T \approx T_c$ and $T > T_c$. The first, second and third row corresponds to the CQD, NQD and UQD models respectively; the former form a spin glass below T_c (no Bragg peaks), while the other two order into Palmer-Chalker. For each panel, the color scale goes from zero to the maximum of intensity.

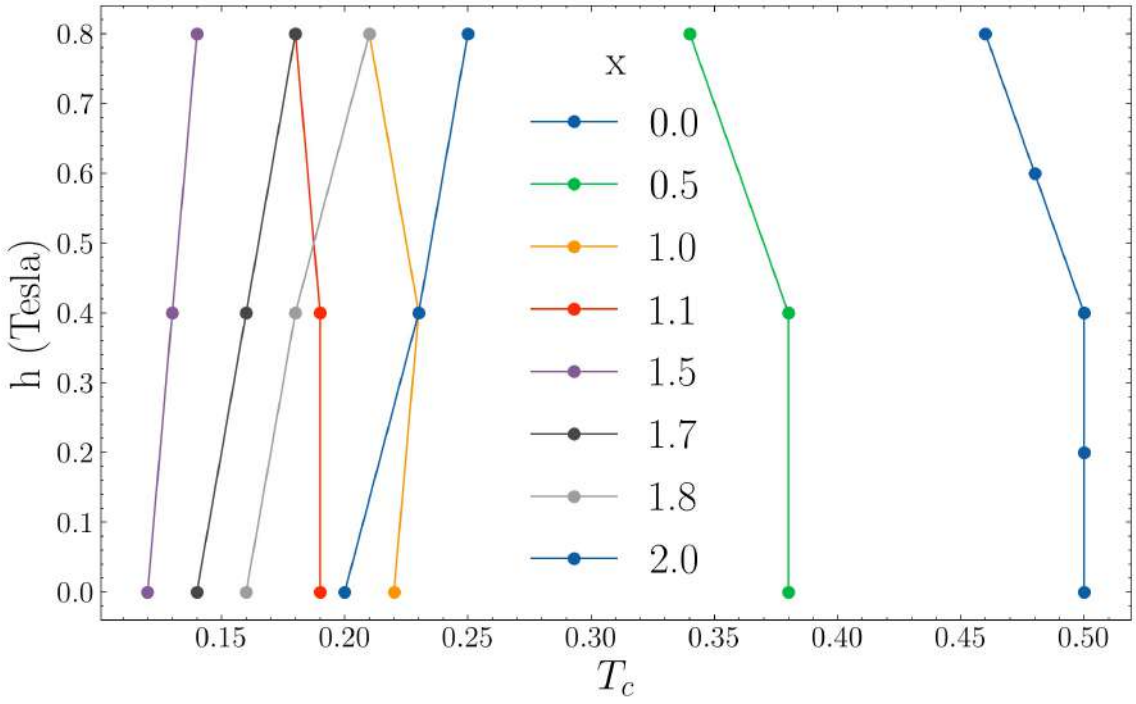

Figure 3.25: Phase diagram of the CQD model in the presence of a magnetic field h in the [001] direction. The transition temperatures are obtained from the peak in specific heat.

Chapter 4

Spin Liquid design

While the previous chapter was motivated by experiments on the competition between the multiple long-range orders in $Er_2Ti_{2-x}Sn_xO_7$ [4], here we want to further explore the opportunity offered by quenched disorder in spin liquids, namely between the Heisenberg pyrochlore antiferromagnet (HAF)[54] and a tensor spin liquid[57], which have been introduced in Chapter 1. While it was possible to quantify the competition between Γ_5 and Palmer-Chalker states in $Er_2Ti_{2-x}Sn_xO_7$ thanks to their order parameters, what happens for spin liquids ? Does the overlap of manifold between the two spin liquids produce long-range order ? Does the quenched disorder enforces a spin glass ? Or do we stabilise a new kind of spin liquid ? In this chapter we will first find the appropriate observables to study, and then analyse the evolution of the system as a function of dilution x.

4.1 Model

The two spin liquids will be labeled TSL for the tensor spin liquid and HAF for the Heisenberg antiferromagnet. The coupling parameters for the two spin liquids are :

$$J^{\mathrm{TSL}} :: (J_1 = 0.0K, J_2 = 0.0K, J_3 = -1.0K, J_4 = 0.0K) \tag{4.1}$$

$$J^{\mathrm{HAF}} :: (J_1 = 1.0K, J_2 = 1.0K, J_3 = 0.0K, J_4 = 0.0K) \tag{4.2}$$

Let us consider a simple form of quenched disorder here. There are $\frac{N}{2}$ tetrahedra for a pyrochlore lattice of N spins. We take $x\%$ of tetrahedra with J^{TSL} couplings and the remaining $(1-x)\%$ tetrahedra with J^{HAF} couplings, randomly distributed across the lattice. Monte Carlo simulations will be averaged over $n \sim 100$ number of samples to ensure the disorder averaging. But first, let us remind the reader of the properties of the two pristine spin liquids [54, 57].

4.2 The tensor and Heisenberg-antiferromagnet spin liquids

In Figure 4.1 we plot the specific heat for the two spin liquids. As expected there is no phase transition down to $T = 0.001$ K. The spin liquids are actually so magnetically "disordered"

that there are no Schottky-like peak that would mark a substantial loss of entropy. The two

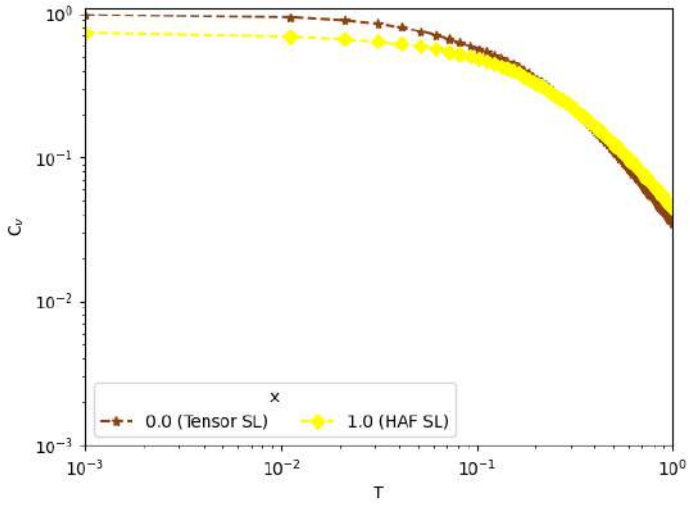

Figure 4.1: Specific heat for the tensor spin liquid and Heisenberg antiferromagnet on a log-log scale.

specific heats do nevertheless differ as $T \to 0^+$. Classical Heisenberg spins usually possess two quadratic degrees of freedom as $T \to 0^+$ due to harmonic oscillations in their local (x, y) plane around their position of equilibrium. Equipartition tells us that each quadratic mode contributes to $k_B T/2$ in the energy, and thus $k_B/2$ in the specific heat. With N spins, we are left with $2\,N\,(k_B/2) = N\,k_B$, which means a specific heat per spin of 1 (here $k_B = 1$). For a system of N classical Heisenberg spins, we cannot have more than $2N$ modes of excitations. However, in spin liquids, excitations out of the ground state can be softer than quadratic, and replaced by quartic modes carrying an energy $k_B T/4$. This is for example what happens around hexagonal plaquettes of spins in the HAF spin liquid on kagome, whose collective excitations (called weather-vane) are quartic in energy [20]. Extending this concept to the pyrochlore lattice where there are as many hexagons as spins, the zero-temperature specific heat becomes

$$C_v^{\mathrm{HAF}} \to \frac{1}{N}\left((2N-N)\frac{k_B}{2} + N\frac{k_B}{4}\right) = \frac{3}{4}k_b \quad [T \to 0^+] \tag{4.3}$$

But these weather-vane excitations are a priori absent from the TSL. As a consequence, the specific heat of the HAF and TSL do not saturate to the same value as $T \to 0^+$ (see Fig. 4.1).

Since they are spin liquids, all order parameters $m_I = 0$. Nonetheless, the reduced susceptibility $\chi_I T$ for each irrep I shows which irrep degrees of freedom fluctuates in the ground state (see Fig. 4.2). According to Ref. [3] and chapter 1, the ground-state manifold of these spin liquids are formed by the combination of the following irreps:

- HAF :: $A_2 \oplus E \oplus T_{1,B} \oplus T_2$
- TSL :: $E \oplus T_{1,A'} \oplus T_2$

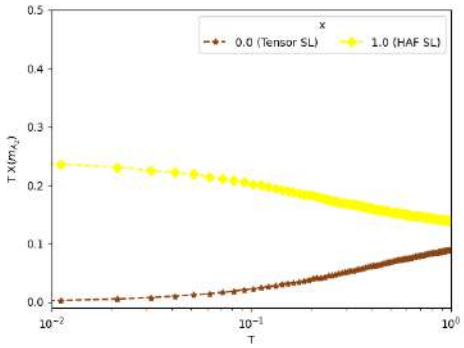

(a) A_2

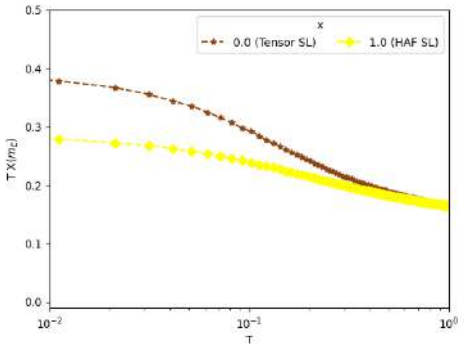

(b) E

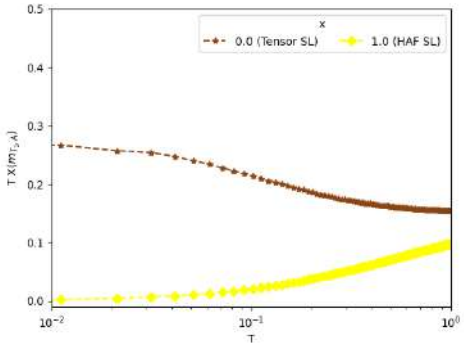

(c) $T_{1,A}$

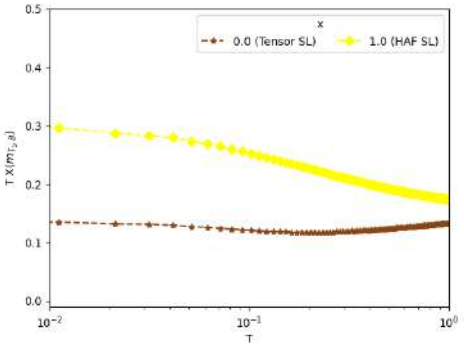

(d) $T_{1,B}$

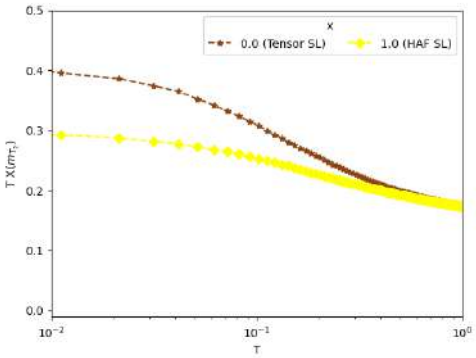

(e) T_2

Figure 4.2: Reduced susceptibilities $\chi_I T$ for each irrep I and for both TSL and HAF. Temperature is in log scale. Degrees of freedom of a given irrep are allowed to fluctuate at low temperature if this irrep belongs to the ground state.

For a given spin liquid, the degrees of freedom of these irreps are allowed to fluctuate in the ground state, which is why the corresponding $\chi_I T$ increases at low temperatures in Fig. 4.2.

For the other irreps, since they correspond to excited states, their fluctuations are suppressed at low temperature and the corresponding $\chi_I T$ vanishes. Note that since $T_{1,A'}$ is a linear combination of $T_{1,A}$ and $T_{1,B}$, $\chi_{T_{1,B}} T$ remains finite for both spin liquids. Hence the main difference between TSL and HAF takes place for A_2 and $T_{1,A}$ fluctuations (see Fig. 4.2(a,c)). In addition, only the E and T_2 irreps belong to the ground-state of both spin liquids.

With this in mind, let us now study what happens when we add quenched disorder to connect the TSL ($x = 0$) to the HAF ($x = 1$) (see definition in section 4.1).

4.3 Results

4.3.1 Specific heat

In Fig. 4.3, we plot the specific heat for $x \in [0; 1]$. We still do not observe any phase transition down to $T = 0.001$ K, as for the pristine systems. However, the value of the specific heat at zero temperature gradually decreases as x increases (see right panel). This evolution seems

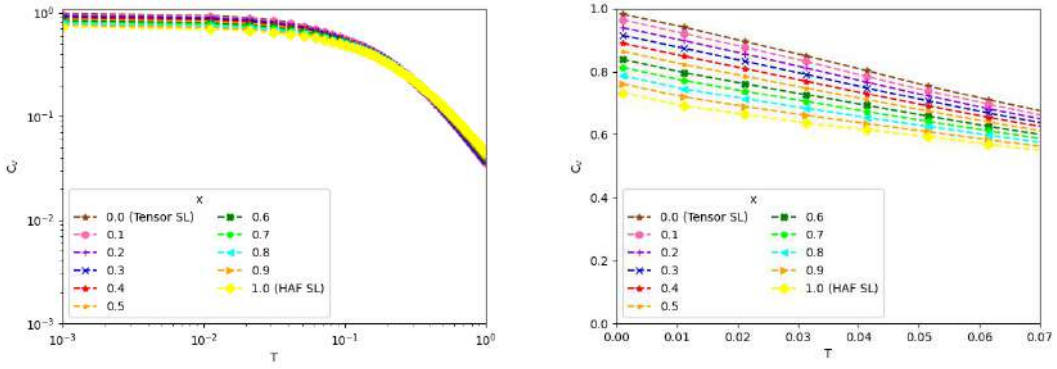

Figure 4.3: *Left:* Specific-heat temperature dependence for $x \in [0; 1]$ on a log-log scale, obtained from Monte Carlo simulations of the model with quenched disorder, as defined in section 4.1. *Right:* Zoom at low temperature of the same data on a linear scale.

to be linear in x at the naked eye. To confirm this observation, we plot on fig. 4.4

$$f(x, T) \equiv \frac{C_v(x, T)}{1 + \alpha x} \tag{4.4}$$

as $T \to 0^+$. We fix $\alpha = -1/4$ to respect the constraint that $C_v(x, T \to 0^+)$ goes from 1 at $x = 0$ to 3/4 at $x = 1$. This scaling function is quasi-independent of the quenched disorder x, which means that $f(x, T) \approx f(T) \to 1$ $[T \to 0^+]$, and the specific heat scales linearly with x close to zero temperature. The overall outcome of this scaling law is that, up to an excellent approximation, each tetrahedron with J^{HAF} coupling contributes equally to the appearance of quartic modes. Hence, as far as low-temperature excitations are concerned, the mixture of HAF and TSL tetrahedra is simply linear and the additional frustration due to quenched disorder is negligible.

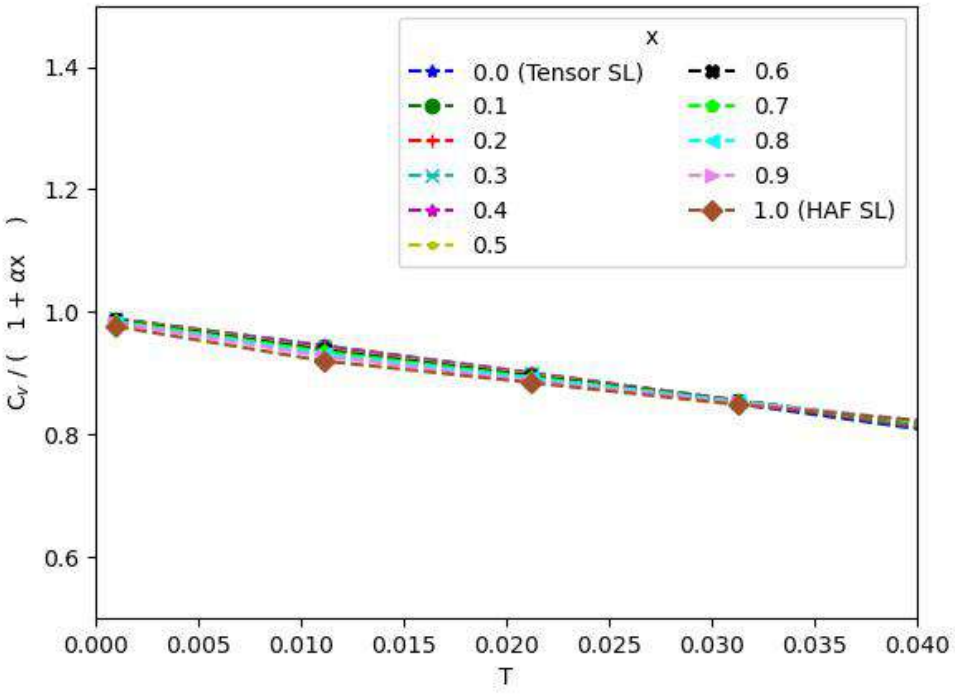

Figure 4.4: Scaling function of the specific heat as $T \to 0^+$ (see Eq. 4.4) for $\alpha = -0.25$, showing that the specific heat grows linearly with x.

4.3.2 Order parameters and susceptibilities

As noticed previously, the only irreps belonging to both spin-liquid ground states are E and T_2. One could imagine that frustration due the mixture of both types of tetrahedra (TSL and HAF) would prevent fluctuations outside of these two irreps (E and T_2). As explained in Fig. 1.11, this would give rise to Ψ_2 order. However, the absence of peaks in the specific heat does not support this scenario, as confirmed by a direct measure of the order parameters which are all zero (up to finite-size effects) (Fig. 4.5).

In absence of long-range order, the reduced magnetic susceptibility χT can be written as

$$\chi T \equiv \frac{1}{N} \sum_{i,j=1}^{N} \langle \mathbf{S}_i \cdot \mathbf{S}_j \rangle. \tag{4.5}$$

In the appropriate units, spin liquids show a Curie-law crossover [104] between the standard paramagnetic Curie law $\chi = 1/T$ and the low-temperature behavior $\chi = K/T$, where K is the normalised integration of magnetic correlations in the spin-liquid ground state. While the standard magnetic susceptibility corresponds to the $T_{1,A}$ irrep, the reduced susceptibility $\chi_I T$ corresponds to the integration of degrees of freedom for a specific irrep I [57]. The

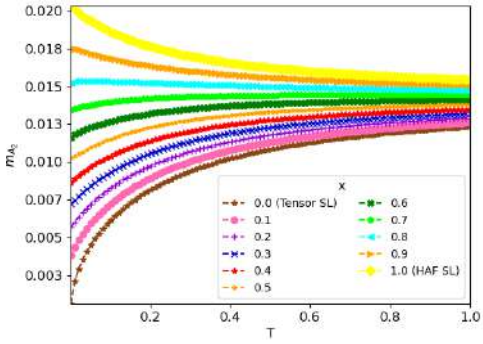

(a) m_{A_2}

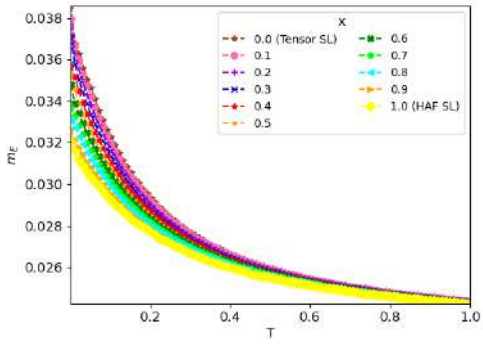

(b) m_{E}

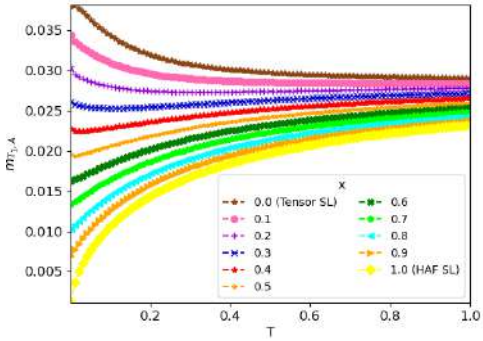

(c) $\mathrm{m}_{T_1,A}$

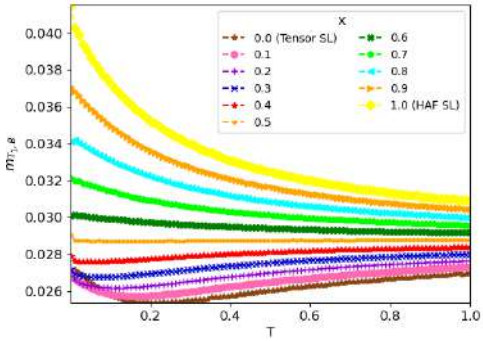

(d) $\mathrm{m}_{T_1,B}$

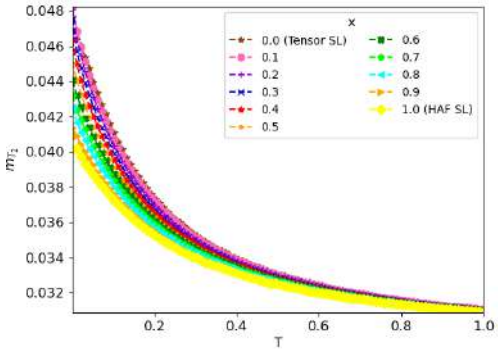

(e) m_{T_2}

Figure 4.5: All order parameters, (a) m_{A_2}, (b) m_E, (c) $m_{T_{1,A}}$, (d) $m_{T_{1,B}}$, (e) m_{T_2}, are zero up to finite-size effects, for all values of x. In particular they are always bounded by the ones of the spin liquids at $x = 0$ or $x = 1$.

quantities $K_I \equiv \chi_I T|_{T\to 0^+}$ are thus a characteristic property of a given spin liquid. Our simulations in Fig. 4.6 show that the value of this plateau $K_I(x)$ evolves monotonically as a function of x for all irreps I. It means each system with a given dilution x forms its own

distinctive spin liquid at low temperature The evolution of K_I depends on the irrep I, and

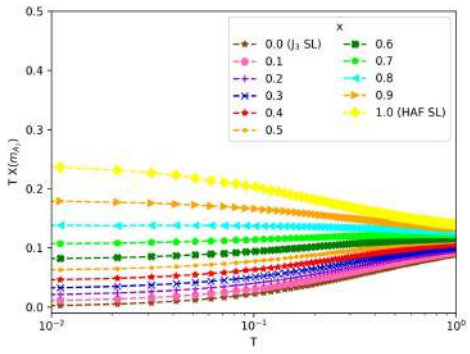

(a) $T\chi_{A_2}$

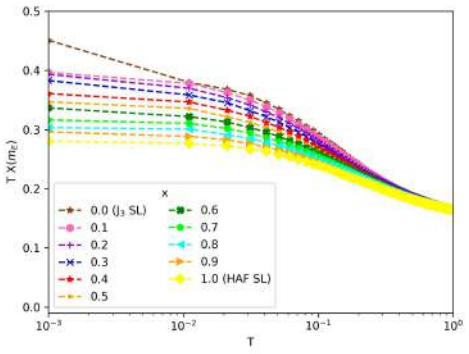

(b) $T\chi_E$

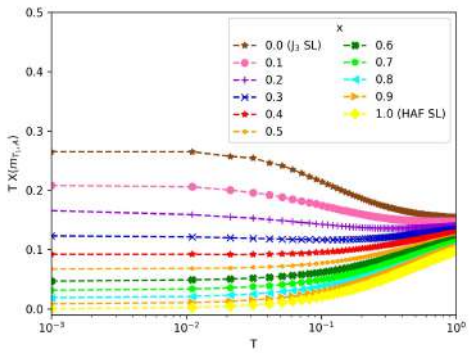

(c) $T\chi_{T_1,A}$

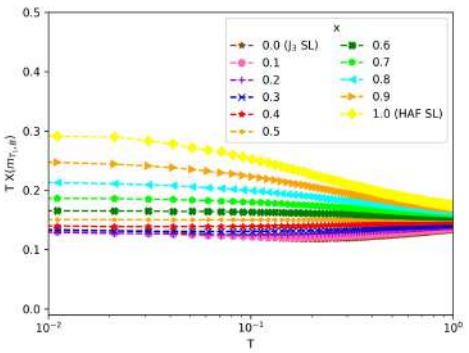

(d) $T\chi_{T_1,B}$

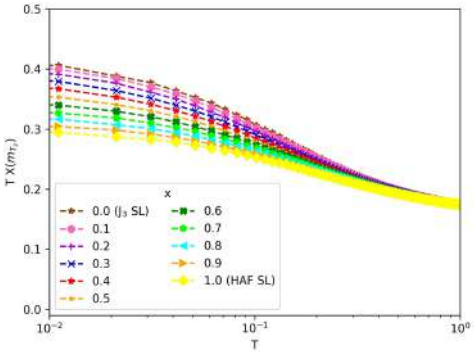

(e) $T\chi_{T_2}$

Figure 4.6: Reduced susceptibilities $\chi_I T$ for each irrep $I = \{\mathrm{A}_2$ (a), E (b), $\mathrm{T}_{1,A}$ (c), $\mathrm{T}_{1,B}$ (d), T_2 (e)$\}$, as a function of the temperature T in log scale, and for different dilutions x. Simulations for $T \ll 0.01$ could be difficult to thermalise, which explains the spurious data point at $T = 0.001$ in panel (b).

as opposed to the specific-heat scaling of Eq. 4.4, it is visibly not linear in x for most irreps: see e.g. how the spacing between the plateaux K_{A_2} (resp. $K_{T_{1A}}$) gets wider (resp. smaller)

as x increases. We rationalise it as follows. In the HAF ($x = 1$), there are no ferromagnetic fluctuations corresponding to the T_{1A} irrep, which is why $K_{T_{1A}} = 0$. As x starts to decrease, a small density of TSL tetrahedra appear in the system, but they are diluted and mostly disconnected from each other. It means ferromagnetic correlations are possible within each tetrahedron, but they can only persist over small length scales between connected cluster of TSL tetrahedra. As x keeps decreasing, two joint effects take place: (i) short-range ferromagnetic correlations linearly increase with the number of TSL tetrahedra, and (ii) long-range ferromagnetic correlations become possible over larger clusters of connected TSL tetrahedra. According to Eq. 4.5, both effects contribute positively to the value of $K_{T_{1A}}$ which thus decreases faster than linearly in x (see Fig. 4.6(c)). The same argument can be applied to the A_2 irrep which is absent from the TSL ground state; and to the T_{1B} irrep which is quasi-absent from the TSL ground state. As a summary, the value of K_I increases faster than linearly as one approaches the spin liquid where the irrep I is part of the ground state. When the irrep is present in both spin liquids (e.g. E and T_2), then the evolution of K_I is closer to linear (see Fig. 4.6(b,e)).

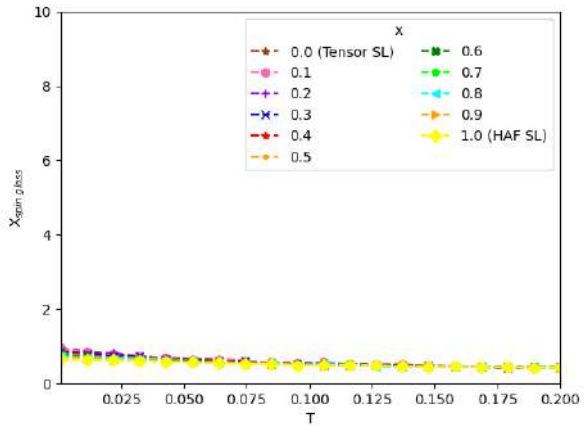

Figure 4.7: Temperature dependence of spin glass susceptibility for different x values.

To conclude, we should make sure that the system does not enter a spin glass. The absence of bump in the specific heat already suggested the absence of any substantial release of entropy expected if the system was freezing. This is confirmed by the spin-glass susceptibility $\chi_{spinglass}$ in Fig. 4.7 where we don't see any rapid increase at low temperature for any dilution x.

As a running summary, we have shown that our model with quenched disorder does neither order nor freeze for any value of dilution x. Instead, it remains in a spin liquid regime for all x, whose properties evolve continuously from TSL to HAF.

4.4 Structure Factor

To conclude this chapter, we will compare the evolution of both the equal-time $S(\mathbf{q})$ and inelastic $S(\mathbf{q}, \mathbf{w})$ structure factors as a function of x. We use the Landau-Lifshitz dynamics for the latter, as explained in section 2.9, averaged over 1000 initial spin configurations obtained from Monte Carlo simulations at very low temperature in the spin liquid regime.

The structure factor is indeed the most quantitative observable, experimentally available, to describe the nature of a spin liquid. Emergent Coulomb gauge fields such as the HAF spin liquid at $x = 1$ appear as pinch-point singularities [56, 105] that evolve into half-moon patterns when increasing the energy w [5, 6, 7] (see Fig. 4.13). But more complex magnetic textures have different signatures, such as the tensor spin liquid at $x = 0$, famous for its pinch lines [57] visible in Fig. 4.8. Pinch lines are extensions of pinch points for higher-rank spin liquids [106].

Turning on the dilution, we see that pinch lines have already smeared out for a small amount of disorder $x = 0.2$ (see Fig. 4.9), and have completely vanished at $x = 0.4$ (see Fig. 4.10). On the other hand, even with a majority of TSL tetrahedra in the system, the contour of the HAF pinch points already starts to form at $x = 0.4$. Increasing the dilution then quickly brings the magnetic correlations closer to the ones of the HAF. Half-moon patterns appear at high energy for $x = 0.6$ (see Fig. 4.11), and the structure factors at $x = 0.8$ and $x = 1$ are essentially the same (see Figs. 4.12 and 4.13), except for the finite thickness of the pinch points. This thickness is most likely due to the length scale imposed by the presence of TSL tetrahedra in the system that break the HAF Coulomb gauge field beyond the mean distance between TSL tetrahedra.

Dilution x thus opens a path between these two spin liquids with an intermediate phase that is qualitatively different from the TSL and HAF. This intermediate phase is, however, not in the middle of the phase diagram ($x = 0.5$) but rather shifted towards $x \sim 0.2 - 0.4$. As opposed to the asymmetry observed in the phase diagrams of chapter 3, there is no reason a priori for the HAF to dominate the TSL here. In the pristine models, the HAF and TSL models are connected by the $J_1 = J_2$ line of Fig. 1.7. It might be possible to search for a different path between the two models, but the important fact is that both spin liquids only rigorously exist in the asymptotic limits $J_1 = J_2 = 0$ for the TSL and $J_3 = 0$ for the HAF. For classical spins, any perturbations would lift the spin-liquid degeneracy. Hence, we must look for the reason elsewhere.

This is where it is useful to remember that, on one hand, the ground-state manifolds of the HAF is a linear combination of $A_2 \oplus E \oplus T_{1,B} \oplus T_2$ states, as explained in section 4.2. It means that deviations from the HAF structure factor mostly come from tetrahedra where $m_{T_{1,A}} \neq 0$. It can happen in TSL tetrahedra, but it only represents a fraction of the 3-dimensional $T_{1,A'}$ subspace within the 8-dimensional TSL manifold composed of $E \oplus$

$T_{1,A'} \oplus T_2$.

On the other hand, deviations from the TSL structure factor mostly come from tetrahedra where $m_{T_{1,B'}} \neq 0$ and $m_{A_2} \neq 0$, which represents a fraction of the 3-dimensional $T_{1,B}$ and the 1-dimensional A_2 subspaces within the 9-dimensional HAF manifold. There is an additional dimension of degrees of freedom that breaks TSL correlations with respect to HAF ones.

It means that at $x = 1/2$, when there is an equal number of TSL and HAF tetrahedra in the system, TSL correlations are more frequently broken than HAF ones when doing a spatial average over the entire system. Hence the structure factor at $x = 0.5$ would look more similar to the HAF one than the TSL one. As a result, the intermediate phase where the system is different from both spin liquids is at lower dilution, for $x \sim 0.2 - 0.4$. As a general rule of thumb, the spin liquid with highest residual entropy tends to dominate the phase diagram in presence of quenched disorder.

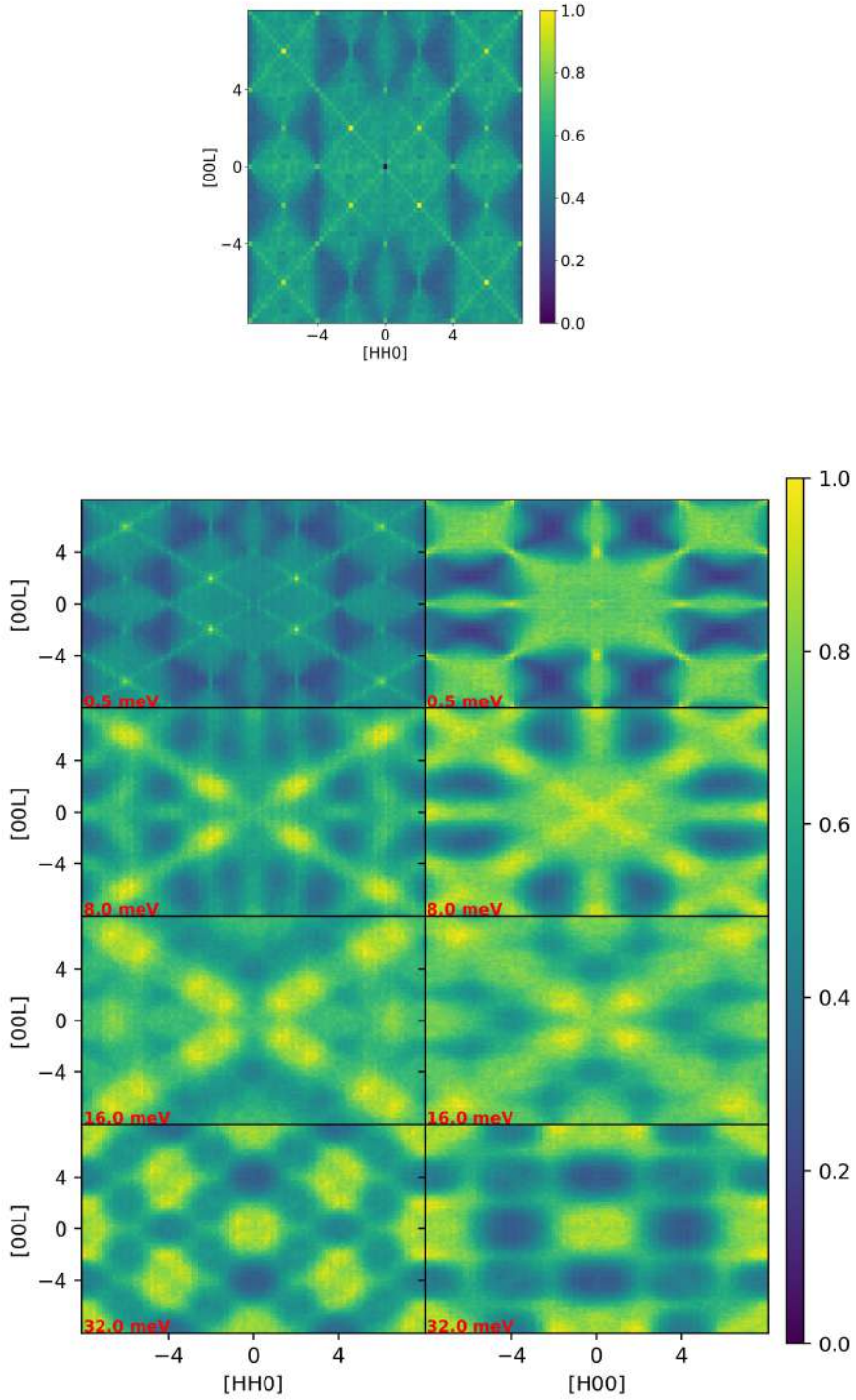

Figure 4.8: Equal-time structure factor in the [HHL] plane (top) and energy cuts of the inelastic structure factor (bottom) for $x = 0$ (TSL, no quenched disorder). The left and right column in the bottom panels correspond to [HHL] and [H0L] planes respectively. The energies are marked in the lower left corner of each subplot. Pinch lines can be seen at energy E = 0.5 meV

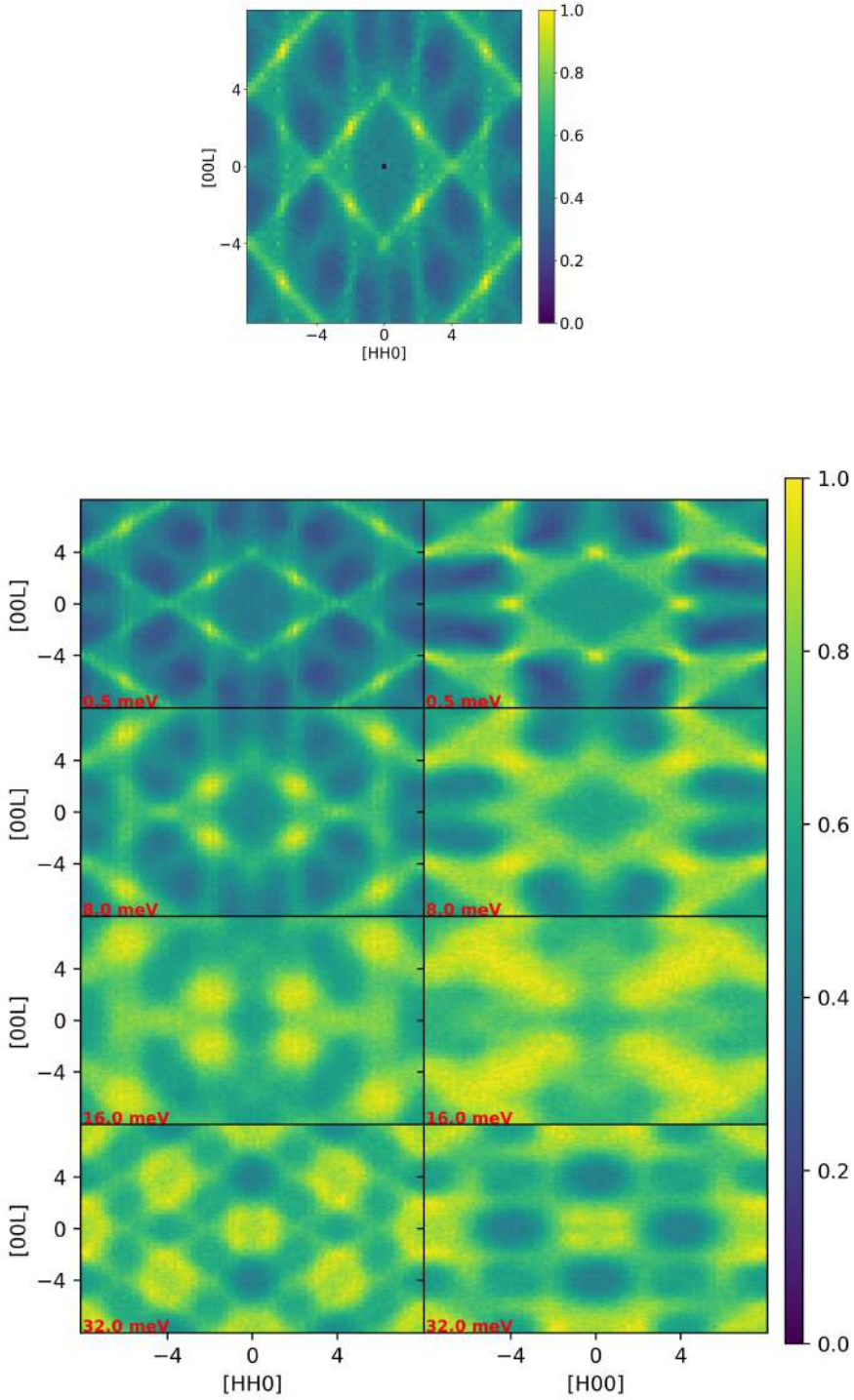

Figure 4.9: Equal-time structure factor in the [HHL] plane (top) and energy cuts of the inelastic structure factor (bottom) for $x = 0.2$. The left and right column in the bottom panels correspond to [HHL] and [H0L] planes respectively. The energies are marked in the lower left corner of each subplot. Pinch lines have smeared out.

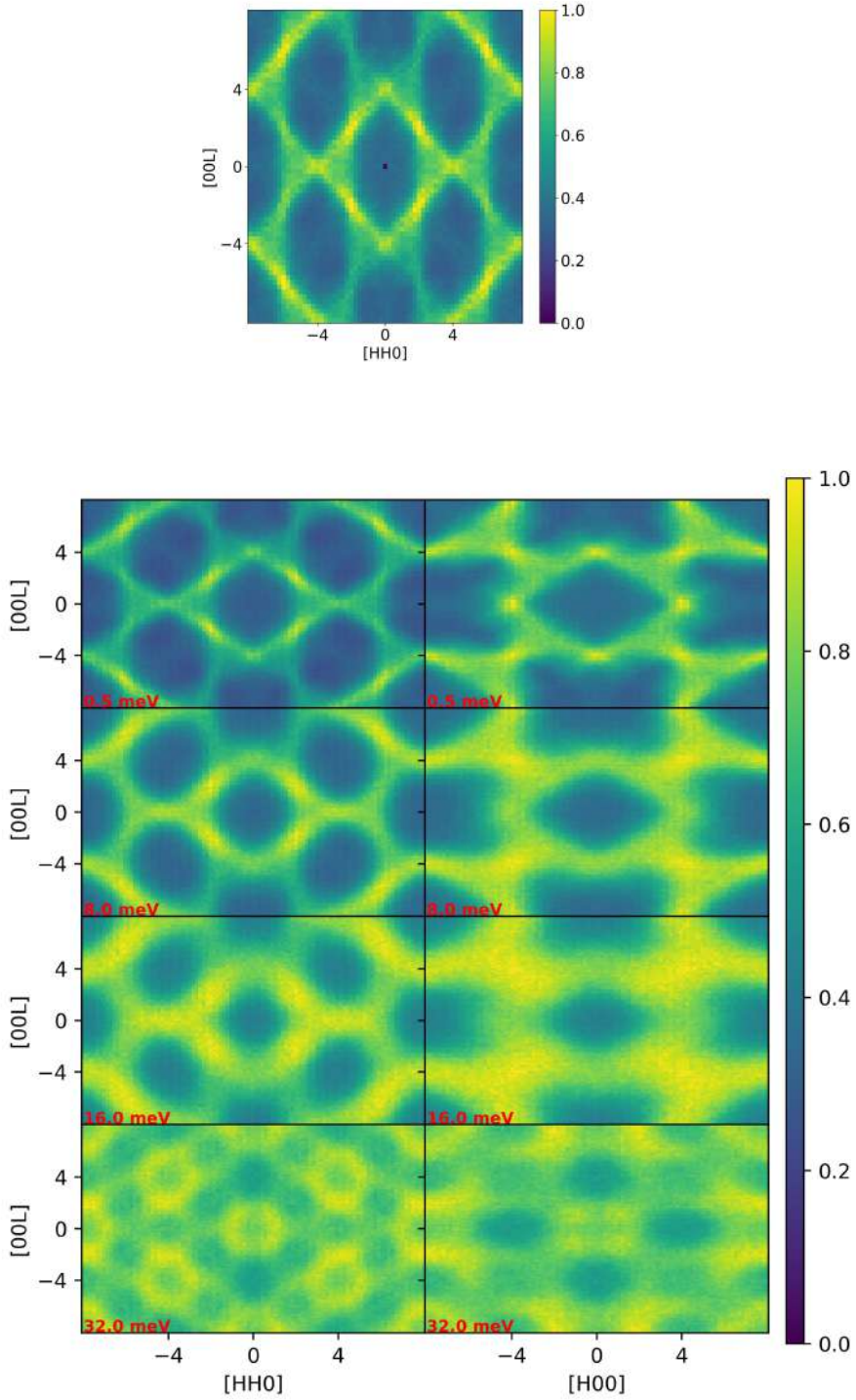

Figure 4.10: Equal-time structure factor in the [HHL] plane (top) and energy cuts of the inelastic structure factor (bottom) for $x = 0.4$. The left and right column in the bottom panels correspond to [HHL] and [H0L] planes respectively. The energies are marked in the lower left corner of each subplot. We are starting to see similarities with HAF spin liquid.

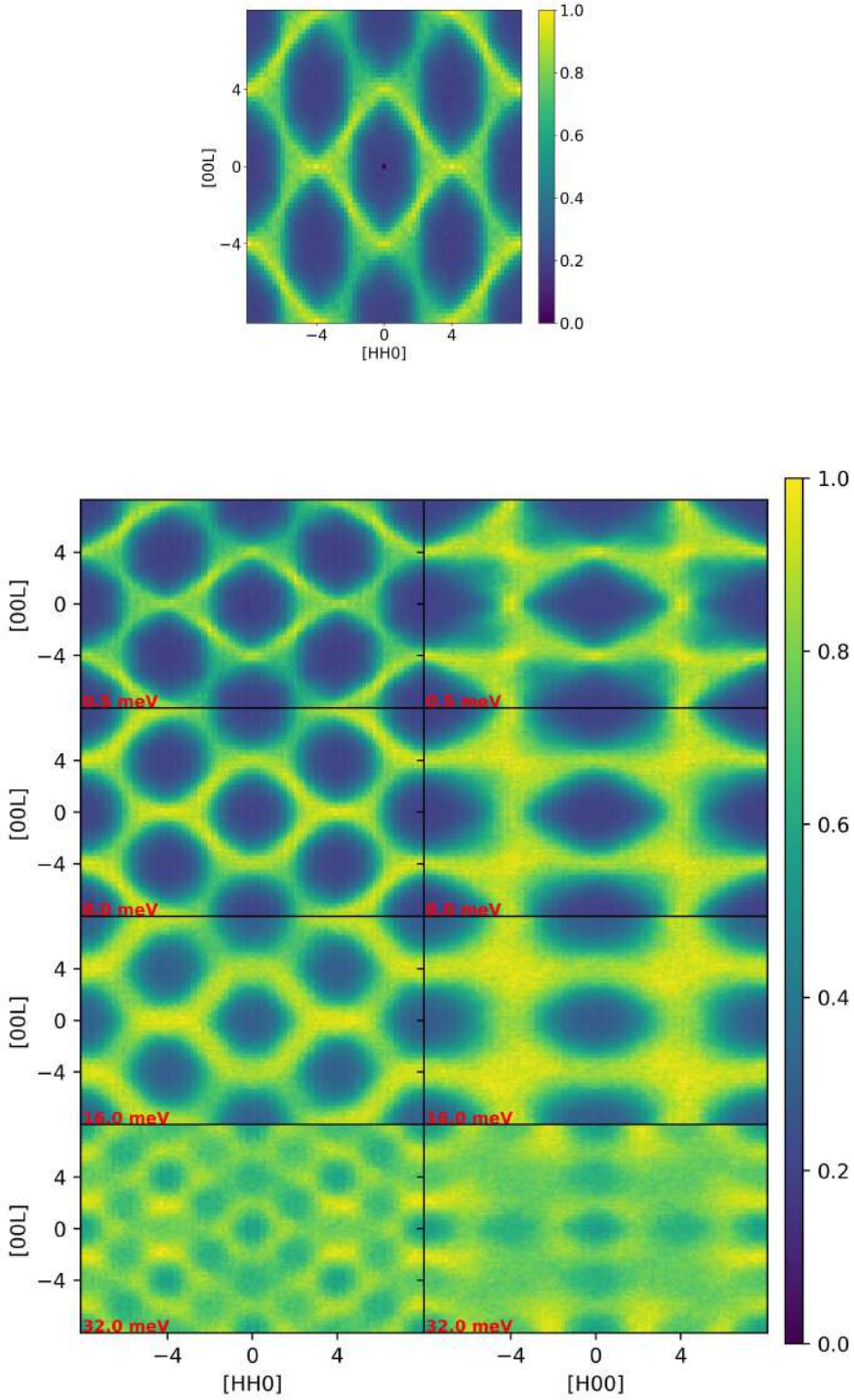

Figure 4.11: Equal-time structure factor in the [HHL] plane (top) and energy cuts of the inelastic structure factor (bottom) for $x = 0.6$. The left and right column in the bottom panels correspond to [HHL] and [H0L] planes respectively. The energies are marked in the lower left corner of each subplot. The structure factor possesses patterns reminiscent to the one of the HAF spin liquid, with broad pinch points at low energy that evolve into half-moon patterns at higher energy [5, 6, 7, 8].

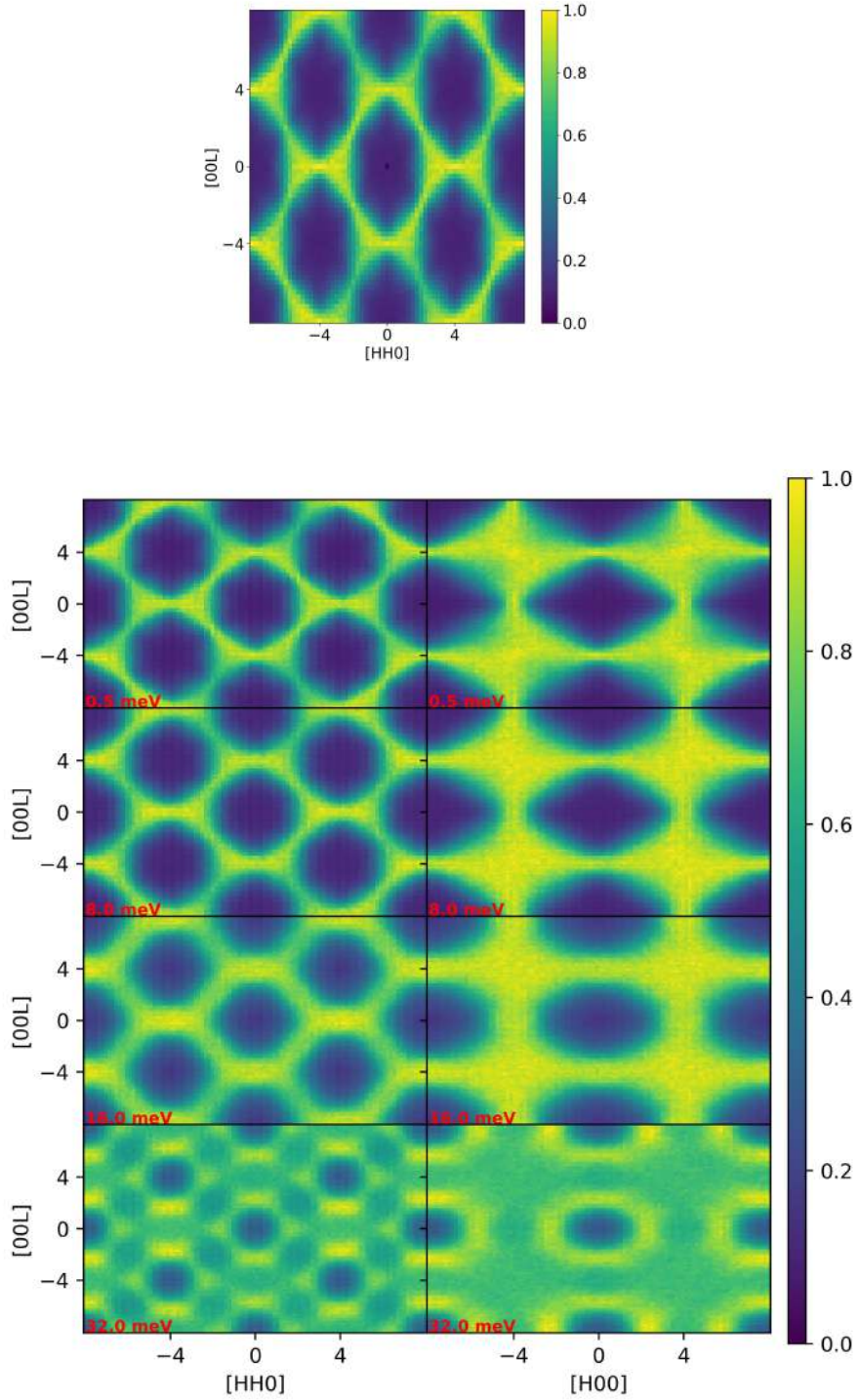

Figure 4.12: Equal-time structure factor in the [HHL] plane (top) and energy cuts of the inelastic structure factor (bottom) for $x = 0.8$. The left and right column in the bottom panels correspond to [HHL] and [H0L] planes respectively. The energies are marked in the lower left corner of each subplot. This structure factor is very similar to the one of the HAF spin liquid. The main difference is the finite thickness of the pinch points, most likely due to the length scale imposed by the presence of TSL tetrahedra in the system that break the HAF gauge field.

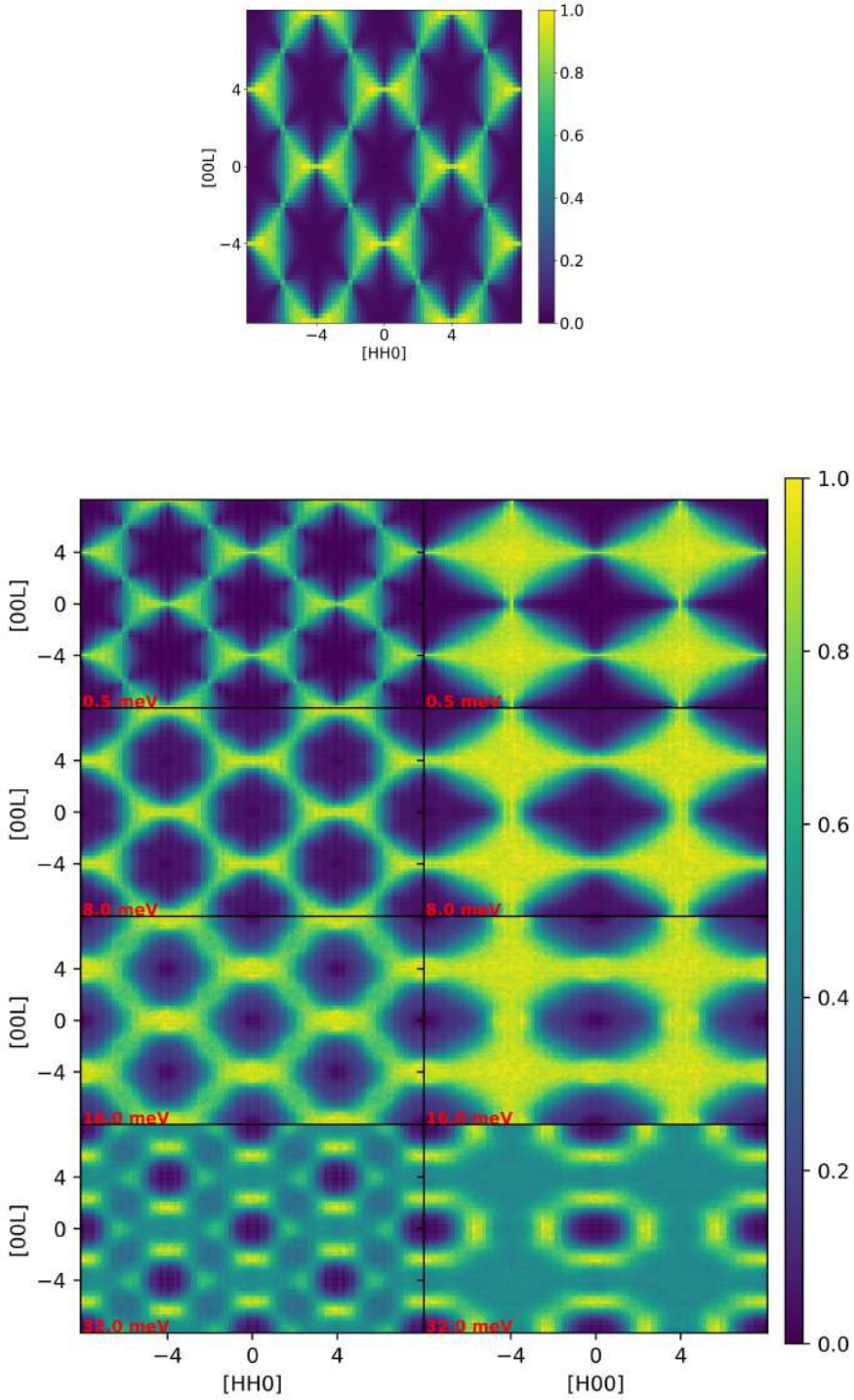

Figure 4.13: Equal-time structure factor in the [HHL] plane (top) and energy cuts of the inelastic structure factor (bottom) for $x = 1$ (HAF, no quenched disorder). The left and right column in the bottom panels correspond to [HHL] and [H0L] planes respectively. The energies are marked in the lower left corner of each subplot.

Chapter 5

Conclusion

In this work, we have studied diverse frustrated systems on pyrochlore lattices. In highly frustrated magnetism, it is usually believed that pristine crystals are necessary, and impurities are unwanted perturbations. Our motivation here was to take the opposing view, and use impurities as a tool to design the properties of frustrated magnets. Exhaustive studies have been done for the two pyrochlore oxides:: $Er_2Ti_2O_7$ and $Er_2Sn_2O_7$. Motivated by experiments on the rare-earth pyrochlore oxide $Er_2Ti_{2-x}Sn_xO_7$[4], the idea was to tune the hamiltonian of our system via non-magnetic dilution x; in other words, to use impurities as a knob to explore unknown parts of the phase diagram. This approach brings us at the frontier between geometric frustration and spin glasses.

We reported in chapter 3 the phase diagram of $Er_2Ti_{2-x}Sn_xO_7$ for $0 \leq x \leq 2$, using classical Monte Carlo simulations for three different models. Our calculations reproduce the shape of the experimental phase diagram [4], with a competition between Γ_5 and Palmer-Chalker antiferromagnetic orders. Depending on the type of quenched disorder, an intermediate spin-glass phase takes place where magnetic order disappears. As in experiments, a pronounced asymmetry in favor of Γ_5 is observed, due to the exchange parameters of $Er_2Sn_2O_7$ being closer to the E/T_2 phase boundary than $Er_2Ti_2O_7$ ones. In addition, above the transition temperature T_c, the structure factors of the two models with quenched disorder closely follow the evolution expected for a pristine model connecting $Er_2Ti_2O_7$ to $Er_2Sn_2O_7$ in parameter space. Finally, in presence of a magnetic field h, we recovered in simulations with quenched disorder the apparition of reentrance expected when approaching $Er_2Sn_2O_7$. All of these results put together strongly support the idea that non-magnetic dilution can be used to explore inaccessible regions in parameter space, by connecting the dots between pristine samples.

In chapter 4, we extended this idea to spins liquids, by continuously diluting the tensor spin liquid ($x = 0$) into the Heisenberg antiferromagnet ($x = 1$). We find neither long-range order nor glassiness in simulations. But the challenge is that in absence of long-range order, we cannot rely on order parameters to measure the presence or absence of a given phase. This is why we had to find alternate solutions in the zero-temperature limit of the specific heat C_v and reduced susceptibility $\chi_I T$ of irrep I. The former offers a measure of the number of

quartic modes in the system, which we find to evolve linearly with dilution x. The latter represents the integration of magnetic correlations for a given irrep, whose evolution with x is not necessarily linear anymore, but remains monotonic. Taken together, these results indicate that we have build a model with a spin-liquid ground state for all values of dilution, and whose properties evolve continuously with x. This is further confirmed by the structure factors, but with a noticeable asymmetry in favour of the spin liquid with highest residual entropy.

As a conclusion, we believe our work in this thesis paves the way for a systematic use of quenched disorder, and in particular non-magnetic dilution, as a knob to tune the properties of frustrated magnets. The range of possibilities is gigantic with rare-earth pyrochlore and spinels alone. It offers a direct way to tune a spin liquid into order or vice-versa, and a platform to search for exotic properties in magnets. On a more fundamental level, with spin liquids as low-energy realizations of emergent gauge fields, it provides a framework to combine artificial gauge fields that might be difficult, nay impossible, to study at high energy.

Appendix A

A.1 g-tensor calculations

In the local coordinate frame, the magnetic moment is given as :

$$m_i^{\alpha} = \sum_{\beta=1}^{3} g_{\mathsf{local}}^{\alpha\beta} \mathsf{S}_i^{\beta} \tag{A.1}$$

which is connected to the spin-1/2 operator S_i^{α} via a g-tensor matrix given as :

$$\mathbf{g}_{\mathsf{local}} = \begin{pmatrix} g_{xy} & 0 & 0 \\ 0 & g_{xy} & 0 \\ 0 & 0 & g_z \end{pmatrix} \tag{A.2}$$

here, α , β are the local coordinates of the spin. Values of g_{xy} and g_z(Table A.1) are derived from experiments on $Er_2Ti_2O_7$, and $Er_2Sn_2O_7$.

	$Yb_2Ti_2O_7$	$Er_2Ti_2O_7$	$Er_2Sn_2O_7$
g_{xy}	4.18	5.97	7.52
g_z	1.77	2.45	0.05

Table A.1: Estimates of the components of the g-tensor in the local frame $\mathbf{g}_{\mathsf{local}}$ [Eq. (A.2)], taken from experiments.

The g-tensor in global coordinates can be formulated by rotating $\mathbf{g}_{\mathsf{local}}$:

$$\mathbf{g}_0 = \begin{pmatrix} g_1 & g_2 & g_2 \\ g_2 & g_1 & g_2 \\ g_2 & g_2 & g_1 \end{pmatrix} \quad \mathbf{g}_1 = \begin{pmatrix} g_1 & -g_2 & -g_2 \\ -g_2 & g_1 & g_2 \\ -g_2 & g_2 & g_1 \end{pmatrix} \tag{A.3}$$

$$\mathbf{g}_2 = \begin{pmatrix} g_1 & -g_2 & g_2 \\ -g_2 & g_1 & -g_2 \\ g_2 & -g_2 & g_1 \end{pmatrix} \qquad \mathbf{g}_3 = \begin{pmatrix} g_1 & g_2 & -g_2 \\ g_2 & g_1 & -g_2 \\ -g_2 & -g_2 & g_1 \end{pmatrix} \tag{A.4}$$

where

$$g_1 = \frac{2}{3}g_{xy} + \frac{1}{3}g_z \quad g_2 = -\frac{1}{3}g_{xy} + \frac{1}{3}g_z. \tag{A.5}$$

A.2 Finite size scaling (Model 1: Correlated quenched disorder)

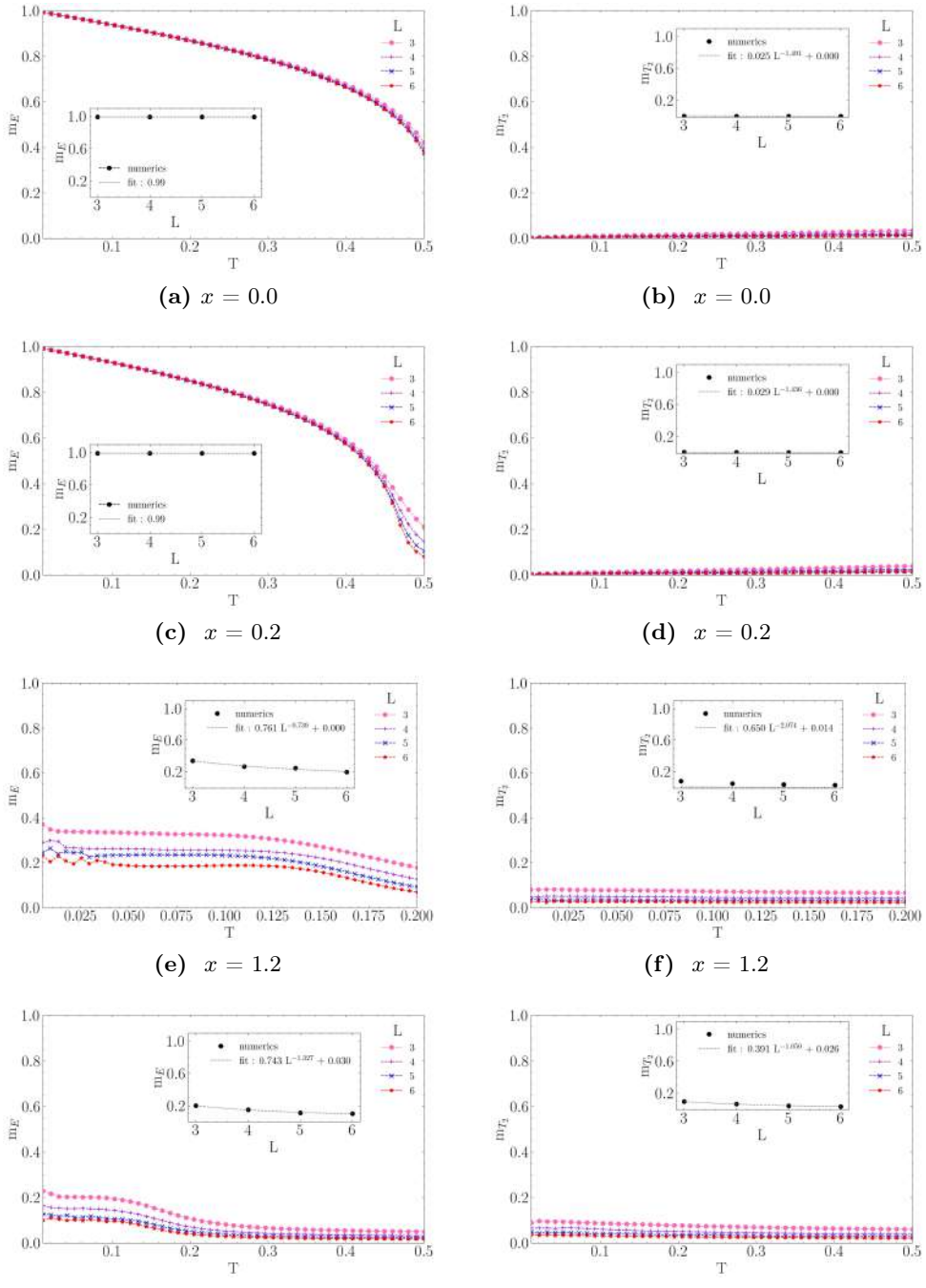

(a) $x = 0.0$ **(b)** $x = 0.0$

(c) $x = 0.2$ **(d)** $x = 0.2$

(e) $x = 1.2$ **(f)** $x = 1.2$

(g) $x = 1.3$ **(h)** $x = 1.3$

Figure A.1: Temperature dependence of m_E (a,c,e,g) and m_{T_2} (b,d,f,h) order parameter for different x values with the finite size scaling on the inset. The constant in the scaling function gives the value of the order parameter in the thermodynamic limit. m_{T_2} vanishes for these x values.

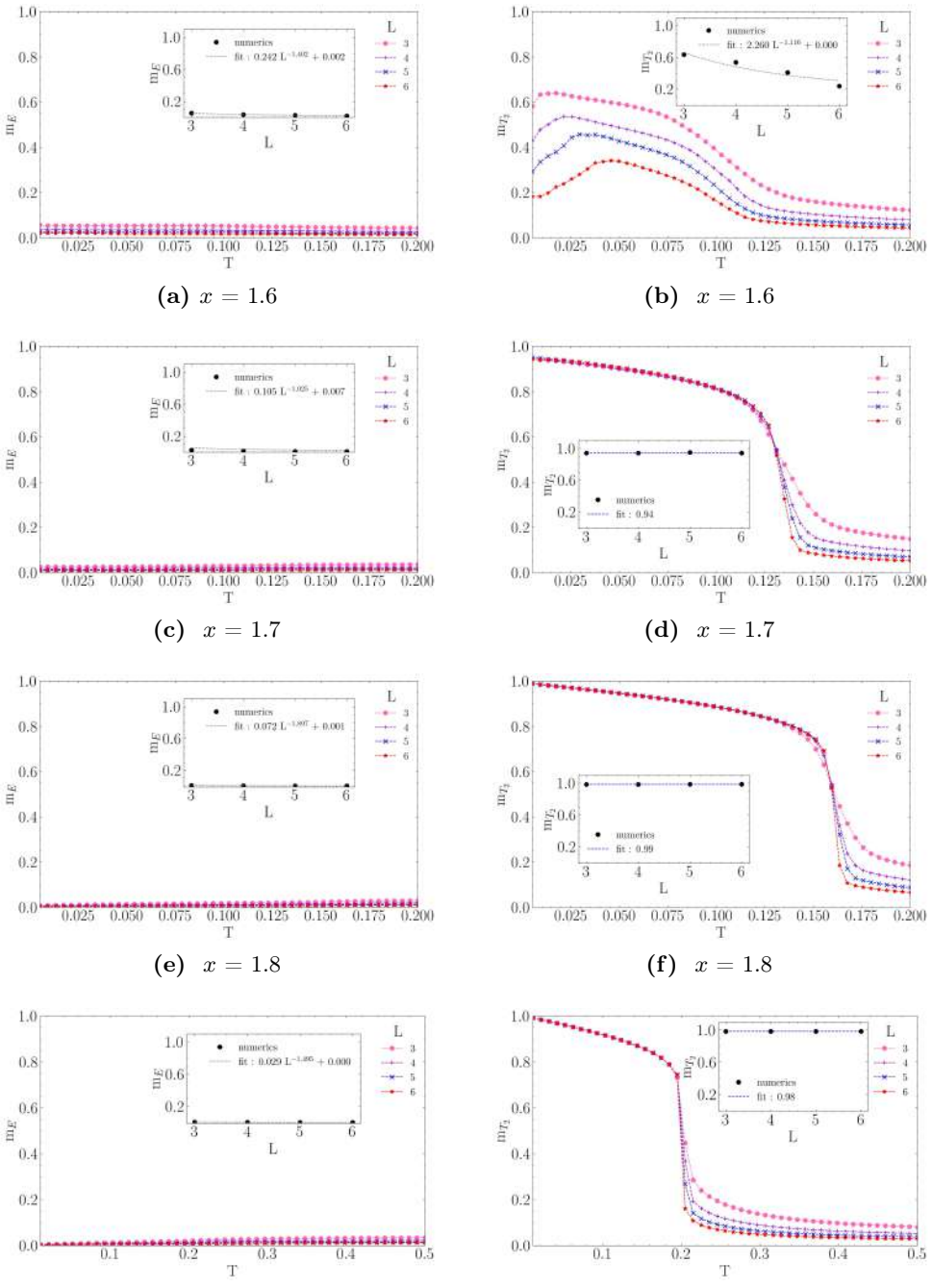

(a) $x = 1.6$ **(b)** $x = 1.6$

(c) $x = 1.7$ **(d)** $x = 1.7$

(e) $x = 1.8$ **(f)** $x = 1.8$

(g) $x = 2.0$ **(h)** $x = 2.0$

Figure A.2: Temperature dependence of m_E (a,c,e,g) and m_{T_2} (b,d,f,h) order parameter for different x values with the finite size scaling on the inset. The constant in the scaling function gives the value of the order parameter in the thermodynamic limit. m_{T_2} vanishes for these x values.

References

[1] Claudine Lacroix, Philippe Mendels, and Frédéric Mila. Introduction to frustrated magnetism : materials, experiments, theory. 2011.

[2] Jason S. Gardner, Michel J. P. Gingras, and John E. Greedan. Magnetic pyrochlore oxides. *Rev. Mod. Phys.*, 82:53–107, Jan 2010.

[3] Han Yan, Owen Benton, Ludovic Jaubert, and Nic Shannon. Theory of multiple-phase competition in pyrochlore magnets with anisotropic exchange with application to $yb_2ti_2o_7, er_2ti_2o_7$, and $er_2sn_2o_7$. *Phys. Rev. B*, 95:094422, Mar 2017.

[4] M. Shirai, R. S. Freitas, J. Lago, S. T. Bramwell, C. Ritter, and I. Živković. Doping-induced quantum crossover in $er_2ti_{2-x}sn_xo_7$. *Phys. Rev. B*, 96:180411, Nov 2017.

[5] J. Robert, B. Canals, V. Simonet, and R. Ballou. Propagation and ghosts in the classical kagome antiferromagnet. *Phys. Rev. Lett.*, 101:117207, Sep 2008.

[6] Tomonari Mizoguchi, Ludovic D. C. Jaubert, Roderich Moessner, and Masafumi Udagawa. Magnetic clustering, half-moons, and shadow pinch points as signals of a proximate coulomb phase in frustrated heisenberg magnets. *Phys. Rev. B*, 98:144446, Oct 2018.

[7] Han Yan, Rico Pohle, and Nic Shannon. Half moons are pinch points with dispersion. *Phys. Rev. B*, 98:140402, Oct 2018.

[8] Shu Zhang, Hitesh J. Changlani, Kemp W. Plumb, Oleg Tchernyshyov, and Roderich Moessner. Dynamical structure factor of the three-dimensional quantum spin liquid candidate $nacani_2f_7$. *Phys. Rev. Lett.*, 122:167203, Apr 2019.

[9] Lucile Savary, Kate A. Ross, Bruce D. Gaulin, Jacob P. C. Ruff, and Leon Balents. Order by quantum disorder in $er_2ti_2\mathbf{o}_7$. *Phys. Rev. Lett.*, 109:167201, Oct 2012.

[10] Solene Guitteny, Sylvain Petit, Elsa Lhotel, Julien Robert, Pierre Bonville, Anne Forget, and Isabelle Mirebeau. Palmer-chalker correlations in the *xy* pyrochlore antiferromagnet $er_2sn_2o_7$. *Phys. Rev. B*, 88:134408, Oct 2013.

[11] M. Plischke and B. Bergerson. *Equilibrium Statistical Physics*. World Scientific, Singapore, 3rd edition, 2006.

[12] K. Binder and A. P. Young. Spin glasses: Experimental facts, theoretical concepts, and open questions. *Rev. Mod. Phys.*, 58:801–976, Oct 1986.

[13] J. Knolle and R. Moessner. A field guide to spin liquids. *Annual Review of Condensed Matter Physics*, 10(1):451–472, 2019.

[14] Stefano Gianni, María Inés Freiberger, Per Jemth, Diego U. Ferreiro, Peter G. Wolynes, and Monika Fuxreiter. Fuzziness and frustration in the energy landscape of protein folding, function, and assembly. *Accounts of Chemical Research*, 54(5):1251–1259, 03 2021.

[15] Tao Jiang, Elizabeth L. Magnotti, and Vincent P. Conticello. Geometrical frustration as a potential design principle for peptide-based assemblies. *Interface Focus*, 7(6):20160141, October 2017.

[16] P. W. Anderson. The resonating valence bond state in la2cuo4 and superconductivity. *Science*, 235(4793):1196–1198, 1987.

[17] A P Ramirez. Strongly geometrically frustrated magnets. *Annual Review of Materials Science*, 24(1):453–480, 1994.

[18] G. H. Wannier. Antiferromagnetism. the triangular ising net. *Phys. Rev.*, 79:357–364, Jul 1950.

[19] Itiro Syôzi. Statistics of Kagomé Lattice. *Progress of Theoretical Physics*, 6(3):306–308, 06 1951.

[20] J. T. Chalker, P. C. W. Holdsworth, and E. F. Shender. Hidden order in a frustrated system: Properties of the heisenberg kagomé antiferromagnet. *Phys. Rev. Lett.*, 68:855–858, Feb 1992.

[21] Villain, J., Bidaux, R., Carton, J.-P., and Conte, R. Order as an effect of disorder. *J. Phys. France*, 41(11):1263–1272, 1980.

[22] Jeffrey G. Rau and Michel J.P. Gingras. Frustrated quantum rare-earth pyrochlores. *Annual Review of Condensed Matter Physics*, 10(1):357–386, 2019.

[23] EF Shender. Anti-ferromagnetic garnets with fluctuation-like interacting sub-lattices. *ZHURNAL EKSPERIMENTALNOI I TEORETICHESKOI FIZIKI*, 83(1):326–337, 1982.

[24] Subir Sachdev. Kagome´- and triangular-lattice heisenberg antiferromagnets: Ordering from quantum fluctuations and quantum-disordered ground states with unconfined bosonic spinons. *Phys. Rev. B*, 45:12377–12396, Jun 1992.

[25] Christopher L. Henley. Ordering due to disorder in a frustrated vector antiferromagnet. *Phys. Rev. Lett.*, 62:2056–2059, Apr 1989.

[26] M. E. Zhitomirsky, M. V. Gvozdikova, P. C. W. Holdsworth, and R. Moessner. Quantum order by disorder and accidental soft mode in $er_2ti_2\mathbf{o}_7$. *Phys. Rev. Lett.*, 109:077204, Aug 2012.

[27] Paul A. McClarty, Pawel Stasiak, and Michel J. P. Gingras. Order-by-disorder in the *xy* pyrochlore antiferromagnet. *Phys. Rev. B*, 89:024425, Jan 2014.

[28] J.E. Greedan, M. Sato, Xu Yan, and F.S. Razavi. Spin-glass-like behavior in y2mo2o7, a concentrated, crystalline system with negligible apparent disorder. *Solid State Communications*, 59(12):895–897, 1986.

[29] Hiroshi Takatsu, Hiroaki Kadowaki, Taku J Sato, Jeffrey W Lynn, Yoshikazu Tabata, Teruo Yamazaki, and Kazuyuki Matsuhira. Quantum spin fluctuations in the spin-liquid state of tb2ti2o7. *Journal of Physics: Condensed Matter*, 24(5):052201, dec 2011.

[30] M. J. Harris, S. T. Bramwell, D. F. McMorrow, T. Zeiske, and K. W. Godfrey. Geometrical frustration in the ferromagnetic pyrochlore $ho_2ti_2O_7$. *Phys. Rev. Lett.*, 79:2554–2557, Sep 1997.

[31] C. Castelnovo, R. Moessner, and S. L. Sondhi. Magnetic monopoles in spin ice. *Nature*, 451(7174):42–45, 2008.

[32] Sylvain Petit, Julien Robert, Solène Guitteny, Pierre Bonville, Claudia Decorse, Jacques Ollivier, Hannu Mutka, Michel J. P. Gingras, and Isabelle Mirebeau. Order by disorder or energetic selection of the ground state in the *xy* pyrochlore antiferromagnet $er_2ti_2o_7$: An inelastic neutron scattering study. *Phys. Rev. B*, 90:060410, Aug 2014.

[33] K. A. Ross, Y. Qiu, J. R. D. Copley, H. A. Dabkowska, and B. D. Gaulin. Order by disorder spin wave gap in the *xy* pyrochlore magnet $er_2ti_2o_7$. *Phys. Rev. Lett.*, 112:057201, Feb 2014.

[34] Y. Yasui, T. Kageyama, T. Moyoshi, M. Soda, M. Sato, and K. Kakurai. Studies on the anomalous hall effect of nd2mo2o7—test of the chirality mechanism. *Journal of Magnetism and Magnetic Materials*, 310(2, Part 2):e544–e546, 2007. Proceedings of the 17th International Conference on Magnetism.

[35] Hironori Sakai, Hiroyuki Ohno, Kazuyoshi Yoshimura, Harukazu Kato, Shinsaku Kambe, Russell E Walstedt, Tatsuma D Matsuda, Yoshinori Haga, Shugo Ikeda, and Yoshichika Ōnuki. Superconductivity in pyrochlore oxide cd2re2o7. *Physica C: Superconductivity*, 378-381:43–46, oct 2002.

[36] Mariam Kavai, Joel Friedman, Kyle Sherman, Mingda Gong, Ioannis Giannakis, Samad Hajinazar, Haoyu Hu, Sarah E. Grefe, Justin Leshen, Qiu Yang, Satoru Nakatsuji, Aleksey N. Kolmogorov, Qimiao Si, Michael Lawler, and Pegor Aynajian. Inhomogeneous kondo-lattice in geometrically frustrated pr2ir2o7. *Nature Communications*, 12(1):1377, 2021.

[37] Kate A. Ross, Lucile Savary, Bruce D. Gaulin, and Leon Balents. Quantum excitations in quantum spin ice. *Phys. Rev. X*, 1:021002, Oct 2011.

[38] S. H. Curnoe. Quantum spin configurations in $tb_2ti_2o_7$. *Phys. Rev. B*, 75:212404, Jun 2007.

[39] P A McClarty, S H Curnoe, and M J P Gingras. Energetic selection of ordered states in a model of the er2ti2o7 frustrated pyrochlore XY antiferromagnet. *Journal of Physics: Conference Series*, 145:012032, jan 2009.

[40] Solène Guitteny, Julien Robert, Pierre Bonville, Jacques Ollivier, Claudia Decorse, Paul Steffens, Martin Boehm, Hannu Mutka, Isabelle Mirebeau, and Sylvain Petit. Anisotropic propagating excitations and quadrupolar effects in $tb_2ti_2\mathbf{o}_7$. *Phys. Rev. Lett.*, 111:087201, Aug 2013.

[41] Lieh-Jeng Chang, Shigeki Onoda, Yixi Su, Ying-Jer Kao, Ku-Ding Tsuei, Yukio Yasui, Kazuhisa Kakurai, and Martin Richard Lees. Higgs transition from a magnetic coulomb liquid to a ferromagnet in yb2ti2o7. *Nature Communications*, 3(1):992, 2012.

[42] A. Yaouanc, P. Dalmas de Réotier, P. Bonville, J. A. Hodges, V. Glazkov, L. Keller, V. Sikolenko, M. Bartkowiak, A. Amato, C. Baines, P. J. C. King, P. C. M. Gubbens, and A. Forget. Dynamical splayed ferromagnetic ground state in the quantum spin ice $yb_2sn_2\mathbf{o}_7$. *Phys. Rev. Lett.*, 110:127207, Mar 2013.

[43] J. D. M. Champion, M. J. Harris, P. C. W. Holdsworth, A. S. Wills, G. Balakrishnan, S. T. Bramwell, E. Čižmár, T. Fennell, J. S. Gardner, J. Lago, D. F. McMorrow, M. Orendáč, A. Orendáčová, D. McK. Paul, R. I. Smith, M. T. F. Telling, and A. Wildes. $er_2ti_2o_7$: evidence of quantum order by disorder in a frustrated antiferromagnet. *Phys. Rev. B*, 68:020401, Jul 2003.

[44] A Poole, A S Wills, and E Lelièvre-Berna. Magnetic ordering in the xy pyrochlore antiferromagnet er2ti2o7: a spherical neutron polarimetry study. *Journal of Physics: Condensed Matter*, 19(45):452201, oct 2007.

[45] S. E. Palmer and J. T. Chalker. Order induced by dipolar interactions in a geometrically frustrated antiferromagnet. *Phys. Rev. B*, 62:488–492, Jul 2000.

[46] S. Petit, E. Lhotel, F. Damay, P. Boutrouille, A. Forget, and D. Colson. Long-range order in the dipolar *xy* antiferromagnet $er_2sn_2o_7$. *Phys. Rev. Lett.*, 119:187202, Oct 2017.

[47] H.W.J. Blöte, R.F. Wielinga, and W.J. Huiskamp. Heat-capacity measurements on rare-earth double oxides r2m2o7. *Physica*, 43(4):549–568, 1969.

[48] R. Siddharthan, B. S. Shastry, A. P. Ramirez, A. Hayashi, R. J. Cava, and S. Rosenkranz. Ising pyrochlore magnets: Low-temperature properties, "ice rules," and beyond. *Phys. Rev. Lett.*, 83:1854–1857, Aug 1999.

[49] V. S. Maryasin and M. E. Zhitomirsky. Order from structural disorder in the *xy* pyrochlore antiferromagnet $er_2ti_2o_7$. *Phys. Rev. B*, 90:094412, Sep 2014.

[50] A. Andreanov and P. A. McClarty. Order induced by dilution in pyrochlore xy antiferromagnets. *Phys. Rev. B*, 91:064401, Feb 2015.

[51] Eric C. Andrade, José A. Hoyos, Stephan Rachel, and Matthias Vojta. Cluster-glass phase in pyrochlore *xy* antiferromagnets with quenched disorder. *Phys. Rev. Lett.*, 120:097204, Mar 2018.

[52] J Lago, T Lancaster, S J Blundell, S T Bramwell, F L Pratt, M Shirai, and C Baines. Magnetic ordering and dynamics in the xy pyrochlore antiferromagnet: a muon-spin relaxation study of er2ti2o7 and er2sn2o7. *Journal of Physics: Condensed Matter*, 17(6):979, jan 2005.

[53] P M Sarte, H J Silverstein, B T K Van Wyk, J S Gardner, Y Qiu, H D Zhou, and C R Wiebe. Absence of long-range magnetic ordering in the pyrochlore compound er2sn2o7. *Journal of Physics: Condensed Matter*, 23(38):382201, sep 2011.

[54] R. Moessner and J. T. Chalker. Properties of a classical spin liquid: The heisenberg pyrochlore antiferromagnet. *Phys. Rev. Lett.*, 80:2929–2932, Mar 1998.

[55] R. Moessner and J. T. Chalker. Low-temperature properties of classical geometrically frustrated antiferromagnets. *Phys. Rev. B*, 58:12049–12062, Nov 1998.

[56] B Canals and D A Garanin. Spin-liquid phase in the pyrochlore anti-ferromagnet. *Canadian Journal of Physics*, 79(11-12):1323–1331, 2001.

[57] Owen Benton, L. D. C. Jaubert, Han Yan, and Nic Shannon. A spin-liquid with pinch-line singularities on the pyrochlore lattice. *Nature Communications*, 7(1):11572, 2016.

[58] G. Toulouse. Theory of the frustration effect in spin glasses: I. In *World Scientific Lecture Notes in Physics*, pages 99–103. WORLD SCIENTIFIC, November 1986.

[59] J A Mydosh. *Spin Glasses*. CRC Press, April 2014.

[60] Hidetoshi Nishimori. *Statistical Physics of Spin Glasses and Information Processing: an Introduction*. Oxford University Press, Oxford; New York, 2001.

[61] S F Edwards and P W Anderson. Theory of spin glasses. *J. phys.*, 5(5):965–974, May 1975.

[62] David Sherrington and Scott Kirkpatrick. Solvable model of a spin-glass. *Phys. Rev. Lett.*, 35:1792–1796, Dec 1975.

[63] J. M. Kosterlitz, D. J. Thouless, and Raymund C. Jones. Spherical model of a spin-glass. *Phys. Rev. Lett.*, 36:1217–1220, May 1976.

[64] Cécile Monthus and Jean-Philippe Bouchaud. Models of traps and glass phenomenology. *Journal of Physics A: Mathematical and General*, 29(14):3847, July 1996.

[65] Karl Heinz Hoffmann. *The Statistical Physics of Energy Landscapes: From Spin Glasses to Optimization*, pages 57–76. Springer Berlin Heidelberg, Berlin, Heidelberg, 2002.

[66] Jean-Philippe Bouchaud, Leticia F. Cugliandolo, Jorge Kurchan, and Marc Mezard. Out of equilibrium dynamics in spin-glasses and other glassy systems, 1997.

[67] G Parisi. The order parameter for spin glasses: a function on the interval 0-1. *Journal of Physics A: Mathematical and General*, 13(3):1101–1112, March 1980.

[68] Leticia F. Cugliandolo and Gustavo Lozano. Real-time nonequilibrium dynamics of quantum glassy systems. *Phys. Rev. B*, 59:915–942, Jan 1999.

[69] K. A. Ross, Th. Proffen, H. A. Dabkowska, J. A. Quilliam, L. R. Yaraskavitch, J. B. Kycia, and B. D. Gaulin. Lightly stuffed pyrochlore structure of single-crystalline $yb_2ti_2o_7$ grown by the optical floating zone technique. *Phys. Rev. B*, 86:174424, Nov 2012.

[70] H. Takatsu, S. Onoda, S. Kittaka, A. Kasahara, Y. Kono, T. Sakakibara, Y. Kato, B. Fåk, J. Ollivier, J. W. Lynn, T. Taniguchi, M. Wakita, and H. Kadowaki. Quadrupole order in the frustrated pyrochlore $tb_{2+x}ti_{2-x}o_{7+y}$. *Phys. Rev. Lett.*, 116:217201, May 2016.

[71] David P. Landau and Kurt Binder. *A Guide to Monte Carlo Simulations in Statistical Physics*. Cambridge University Press, 3 edition, 2009.

[72] Bernd A Berg. *Markov Chain Monte Carlo Simulations and Their Statistical Analysis*. WORLD SCIENTIFIC, October 2004.

[73] N. Metropolis, Arianna W. Rosenbluth, Marshall N. Rosenbluth, A. H. Teller, and Edward Teller. Equation of state calculations by fast computing machines. *Journal of Chemical Physics*, 21:1087–1092, 1953.

[74] Alexander A Markov. Extension of the law of large numbers to quantities, depending on each other (1906). reprint. 2006.

[75] P. W. Bridgman. Note on the principle of detailed balancing. *Phys. Rev.*, 31:101–102, Jan 1928.

[76] LUDWIG BOLTZMANN. Further studies on the thermal equilibrium of gas molecules. In *History of Modern Physical Sciences*, pages 262–349. PUBLISHED BY IMPERIAL COLLEGE PRESS AND DISTRIBUTED BY WORLD SCIENTIFIC PUBLISHING CO., July 2003.

[77] Y Miyatake, M Yamamoto, J J Kim, M Toyonaga, and O Nagai. On the implementation of the 'heat bath' algorithms for monte carlo simulations of classical heisenberg spin systems. *Journal of Physics C: Solid State Physics*, 19(14):2539–2546, May 1986.

[78] Michael Creutz. Overrelaxation and monte carlo simulation. *Phys. Rev. D*, 36:515–519, Jul 1987.

[79] Frank R. Brown and Thomas J. Woch. Overrelaxed heat-bath and metropolis algorithms for accelerating pure gauge monte carlo calculations. *Phys. Rev. Lett.*, 58:2394–2396, Jun 1987.

[80] Shai Wiseman and Eytan Domany. Lack of self-averaging in critical disordered systems. *Phys. Rev. E*, 52:3469–3484, Oct 1995.

[81] E Marinari and G Parisi. Simulated tempering: A new monte carlo scheme. *Europhysics Letters (EPL)*, 19(6):451–458, jul 1992.

[82] Koji Hukushima and Koji Nemoto. Exchange monte carlo method and application to spin glass simulations. *Journal of the Physical Society of Japan*, 65(6):1604–1608, 1996.

[83] Robert H. Swendsen and Jian-Sheng Wang. Replica monte carlo simulation of spin-glasses. *Phys. Rev. Lett.*, 57:2607–2609, Nov 1986.

[84] K. Binder. Critical properties from monte carlo coarse graining and renormalization. *Phys. Rev. Lett.*, 47:693–696, Aug 1981.

[85] K. Binder. Finite size scaling analysis of ising model block distribution functions. *Zeitschrift für Physik B Condensed Matter*, 43(2):119–140, 1981.

[86] Lisandro Dalcin and Yao-Lung L. Fang. mpi4py: Status update after 12 years of development. *Computing in Science Engineering*, 23(4):47–54, 2021.

[87] Lisandro D. Dalcin, Rodrigo R. Paz, Pablo A. Kler, and Alejandro Cosimo. Parallel distributed computing using python. *Advances in Water Resources*, 34(9):1124–1139, 2011. New Computational Methods and Software Tools.

[88] Lisandro Dalcín, Rodrigo Paz, Mario Storti, and Jorge D'Elía. Mpi for python: Performance improvements and mpi-2 extensions. *Journal of Parallel and Distributed Computing*, 68(5):655–662, 2008.

[89] Lisandro Dalcín, Rodrigo Paz, and Mario Storti. Mpi for python. *Journal of Parallel and Distributed Computing*, 65(9):1108–1115, 2005.

[90] L. D. Landau and E. M. Lifshitz. *The Classical Theory of Fields*. Butterworth-Heinemann, 4 edition, January 1980.

[91] C. Runge. Ueber die numerische auflösung von differentialgleichungen. *Mathematische Annalen*, 46(2):167–178, 1895.

[92] Mathieu Taillefumier, Julien Robert, Christopher L. Henley, Roderich Moessner, and Benjamin Canals. Semiclassical spin dynamics of the antiferromagnetic heisenberg model on the kagome lattice. *Phys. Rev. B*, 90:064419, Aug 2014.

[93] J D M Champion and P C W Holdsworth. Soft modes in the easy plane pyrochlore antiferromagnet. *Journal of Physics: Condensed Matter*, 16(11):S665–S671, March 2004.

[94] P. Dalmas de Réotier, A. Yaouanc, Y. Chapuis, S. H. Curnoe, B. Grenier, E. Ressouche, C. Marin, J. Lago, C. Baines, and S. R. Giblin. Magnetic order, magnetic correlations, and spin dynamics in the pyrochlore antiferromagnet $er_2ti_2o_7$. *Phys. Rev. B*, 86:104424, Sep 2012.

[95] J. Oitmaa, R. R. P. Singh, B. Javanparast, A. G. R. Day, B. V. Bagheri, and M. J. P. Gingras. Phase transition and thermal order-by-disorder in the pyrochlore antiferromagnet $er_2ti_2o_7$: A high-temperature series expansion study. *Phys. Rev. B*, 88:220404, Dec 2013.

[96] Anson W. C. Wong, Zhihao Hao, and Michel J. P. Gingras. Ground state phase diagram of generic *xy* pyrochlore magnets with quantum fluctuations. *Phys. Rev. B*, 88:144402, Oct 2013.

[97] D. R. Yahne, D. Pereira, L. D. C. Jaubert, L. D. Sanjeewa, M. Powell, J. W. Kolis, Guangyong Xu, M. Enjalran, M. J. P. Gingras, and K. A. Ross. Understanding reentrance in frustrated magnets: The case of the $er_2sn_2o_7$ pyrochlore. *Phys. Rev. Lett.*, 127:277206, Dec 2021.

[98] H. G. Ballesteros, A. Cruz, L. A. Fernández, V. Martín-Mayor, J. Pech, J. J. Ruiz-Lorenzo, A. Tarancón, P. Téllez, C. L. Ullod, and C. Ungil. Critical behavior of the three-dimensional ising spin glass. *Phys. Rev. B*, 62:14237–14245, Dec 2000.

[99] H. G. Ballesteros, L. A. Fernández, V. Martín-Mayor, A. Muñoz Sudupe, G. Parisi, and J. J. Ruiz-Lorenzo. Critical exponents of the three-dimensional diluted ising model. *Phys. Rev. B*, 58:2740–2747, Aug 1998.

[100] E. Marinari, C. Naitza, F. Zuliani, G. Parisi, M. Picco, and F. Ritort. General method to determine replica symmetry breaking transitions. *Phys. Rev. Lett.*, 81:1698–1701, Aug 1998.

[101] M. E. Zhitomirsky, P. C. W. Holdsworth, and R. Moessner. Nature of finite-temperature transition in anisotropic pyrochlore $er_2ti_2o_7$. *Phys. Rev. B*, 89:140403, Apr 2014.

[102] Jie Lou, Anders W. Sandvik, and Leon Balents. Emergence of u(1) symmetry in the 3d *xy* model with Z_q anisotropy. *Phys. Rev. Lett.*, 99:207203, Nov 2007.

[103] L. D. C. Jaubert, Owen Benton, Jeffrey G. Rau, J. Oitmaa, R. R. P. Singh, Nic Shannon, and Michel J. P. Gingras. Are multiphase competition and order by disorder the keys to understanding $yb_2ti_2o_7$? *Phys. Rev. Lett.*, 115:267208, Dec 2015.

[104] L. D. C. Jaubert, M. J. Harris, T. Fennell, R. G. Melko, S. T. Bramwell, and P. C. W. Holdsworth. Topological-sector fluctuations and curie-law crossover in spin ice. *Phys. Rev. X*, 3:011014, Feb 2013.

[105] C. L. Henley. The "coulomb phase" in frustrated systems. *Annu. Rev. Condens. Matter Phys.*, 1(1):179–210, 2010.

[106] Owen Benton and Roderich Moessner. Topological route to new and unusual coulomb spin liquids. *Phys. Rev. Lett.*, 127:107202, Sep 2021.